US Department of Transportation Federal Highway Administration
Research, Development, and Technology Turner-Fairbank Highway
Research Center 6300 Georgetown Pike McLean, VA 22101-2296

Microdamage Healing in Asphalt and Asphalt Concrete, Volume 2: Laboratory and Field Testing to Assess and Evaluate Microdamage and Micordamage Healing.

FHWA-RD-98-142

June 2001

FOREWORD

Public Law 102-240, the Intermodal Surface Transportation Efficiency Act (ISTEA) of 1991, directed the Federal Highway Administration in Section 6016 to enter into a 5-year contract research program with the Western Research Institute (WRI) of the University of Wyoming. The title of this research program is Fundamental Properties of Asphalts and Modified Asphalts, Contract No. DTFH61-92-C-00170. As part of this contract, Task K–Microdamage Healing in Asphalt and Asphalt Concrete was performed by the Texas Transportation Institute of Texas A&M University and North Carolina State University.

This report details the results of the Task K subcontract; the main body of the WRI report will be published subsequently. The results of Task K have advanced our understanding, both theoretically and in terms of measurement, of fatigue damage, especially fatigue cracking, in asphalt pavements. It explicitly and quantitatively considers the impact of healing, the regaining of pavement strength and integrity upon standing without traffic (resting), on fatigue life. This research is expected to form the basis of specification testing for fatigue susceptibility and the improvement of fatigue life of asphalt pavements.

T. Paul Teng, P.E.
Director, Office of Infrastructure
Research and Development

NOTICE

Technical Report Documentation Page

1. Report No. FHWA-RD-98-142	2. Government Accession No.	3. Recipient's Catalog No.

4. Title and Subtitle `Microdamage Healing in Asphalt and Asphalt Concrete, Volume II, Laboratory and Field Testing to Assess and Evaluate Microdamage and Microdamage Healing`	5. Report Date `June 2001` 6. Performing Organization Code
7. Author(s) D. Williams, D.N. Little, R.L. Lytton, Y. R. Kim, and Y. Kim	8. Performing Organization Report No. Research Report 7229
9. Performing Organization Name and Address Texas Transportation Institute The Texas A&M University System College Station, Texas 77843-3135	10. Work Unit No. (TRAIS) 11. Contract or Grant No. DTFH61-92-C-00170
12. Sponsoring Agency Name and Address Western Research Institute (WRI) P.O. Box 3395 University Station Laramie, Wyoming 82071	13. Type of Report and Period Covered Final: May 1998 14. Sponsoring Agency Code

15. Supplementary Notes

Research performed in cooperation with the Federal Highway Administration
Research Project Title: Fundamental Properties of Asphalts and Modified Asphalts
Task K – Microdamage Healing in Asphalt and Asphalt Concrete

16. Abstract

Volume 2 documents laboratory and field testing that provides the evidence that microdamage healing is real and measurable and that it has a significant impact on pavement performance. Part of the laboratory experiments to evaluate the impact of rest periods were performed at North Carolina State University (NCSU). The experiment included two very different asphalt binders: AAD and AAM. The experiment clearly demonstrated that the rest periods introduced after fatigue damage allowed significant recovery in the flexural and dynamic modulus. The recovery was attributed to the healing of microcracks within the sample.

A separate series of laboratory testing was performed at Texas A&M University's Texas Transportation Institute (TTI). These tests consisted of controlled-strain haversine loading direct tensile tests and controlled-strain trapezoidal loading direct tensile tests. The change and rate of change in Dissipated Pseudo-Strain Energy (DPSE) were recorded throughout the test and after rest periods introduced during the fatigue tests. The recovered DPSE after the rest period normalized by the DPSE before the rest period defined a Healing Index (HI) term used to quantify healing. Although healing was found to be dependent on the temperature of the mixture during the rest period and the length of the rest period, it was also found to be highly dependent on the type of asphalt cement. Asphalt AAM was found to provide much better healing properties than asphalt AAD, which is in agreement with the work of NCSU where significantly different testing protocols were used.

Volume 2 completes the evidence of microdamage healing with convincing field evidence. Wave speed and attenuation measurements were made on in situ pavements. The stress wave test and analysis successfully detected fatigue damage growth and microdamage healing of asphalt pavements (at the FHWA's Turner-Fairbank Highway Research Center – Accelerated Loading Facility) with different asphalt layer thicknesses and viscosities and demonstrated the importance of microdamage healing during rest periods of pavement performance. The ability of stress wave testing to measure microdamage and healing in the field was further evaluated at the Minnesota Road Project (Mn/ROAD) on seven pavement test sections at the site. The fact that healing does occur in pavements in the field during rest periods suggests that the performance and service life of the pavement will be increased if rest periods are introduced, or if binders are used that heal more quickly and completely.

`asphalt concrete, microcracks, microdamage healing, binders`	18. Distribution Statement No restrictions. This document is available to the public through NTIS: National Technical Information Service 5285 Port Royal Road Springfield, Virginia 22161

19. Security Classif.(of this report) Unclassified	20. Security Classif.(of this page) Unclassified	21. No. of Pages 180	22. Price

Form DOT F 1700.7 (8-72) **Reproduction of completed page authorized**

SI* (MODERN METRIC) CONVERSION FACTORS

APPROXIMATE CONVERSIONS TO SI UNITS

Symbol	When You Know	Multiply By	To Find	Symbol
		LENGTH		
in	inches	25.4	millimeters	mm
ft	feet	0.305	meters	m
yd	yards	0.914	meters	m
mi	miles	1.61	kilometers	km
		AREA		
in^2	square inches	645.2	square millimeters	mm^2
ft^2	square feet	0.093	square meters	m^2
yd^2	square yards	0.836	square meters	m^2
ac	acres	0.405	hectares	ha
mi^2	square miles	2.59	square kilometers	km^2
		VOLUME		
fl oz	fluid ounces	29.57	milliliters	mL
gal	gallons	3.785	liters	L
ft^3	cubic feet	0.028	cubic meters	m^3
yd^3	cubic yards	0.765	cubic meters	m^3
NOTE: Volumes greater than 1000 l shall be shown in m^3.				
		MASS		
oz	ounces	28.35	grams	g
lb	pounds	0.454	kilograms	kg
T	short tons (2000 lb)	0.907	megagrams (or "metric ton")	Mg (or "t")
		TEMPERATURE (exact)		
°F	Fahrenheit temperature	5(F-32)/9 or (F-32)/1.8	Celcius temperature	°C
		ILLUMINATION		
fc	foot-candles	10.76	lux	lx
fl	foot-Lamberts	3.426	candela/m^2	cd/m^2
		FORCE and PRESSURE or STRESS		
lbf	poundforce	4.45	newtons	N
lbf/in^2	poundforce per square inch	6.89	kilopascals	kPa

APPROXIMATE CONVERSIONS FROM SI UNITS

Symbol	When You Know	Multiply By	To Find	Symbol
		LENGTH		
mm	millimeters	0.039	inches	in
m	meters	3.28	feet	ft
m	meters	1.09	yards	yd
km	kilometers	0.621	miles	mi
		AREA		
mm^2	square millimeters	0.0016	square inches	in^2
m^2	square meters	10.764	square feet	ft^2
m^2	square meters	1.195	square yards	yd^2
ha	hectares	2.47	acres	ac
km^2	square kilometers	0.386	square miles	mi^2
		VOLUME		
mL	milliliters	0.034	fluid ounces	fl oz
L	liters	0.264	gallons	gal
m^3	cubic meters	35.71	cubic feet	ft^3
m^3	cubic meters	1.307	cubic yards	yd^3
		MASS		
g	grams	0.035	ounces	oz
kg	kilograms	2.202	pounds	lb
Mg (or "t")	megagrams (or "metric ton")	1.103	short tons (2000 lb)	T
		TEMPERATURE (exact)		
°C	Celcius temperature	1.8C + 32	Fahrenheit temperature	°F
		ILLUMINATION		
lx	lux	0.0929	foot-candles	fc
cd/m^2	candela/m^2	0.2919	foot-Lamberts	fl
		FORCE and PRESSURE or STRESS		
N	newtons	0.225	poundforce	lbf
kPa	kilopascals	0.145	poundforce per square inch	lbf/in^2

* SI is the symbol for the International System of Units. Appropriate rounding should be made to comply with Section 4 of ASTM E380.

(Revised September 1993)

TABLE OF CONTENTS

Section Page

TABLE OF CONTENTS
(continued)

LIST OF TABLES

LIST OF FIGURES

LIST OF FIGURES
(continued)

LIST OF FIGURES
(continued)

LIST OF FIGURES
(continued)

VOLUME 2: LABORATORY AND FIELD TESTING TO ASSESS AND EVALUATE MICRODAMAGE AND MICRODAMAGE HEALING

PROJECT SUMMARY

Background and Objectives

This final report documents the findings of a four and one-half year study of ***"Microdamage Healing in Asphalt and Asphalt Concrete."*** The study is identified as Task K in a larger overall study under the direction of Western Research Institute entitled ***"Fundamental Properties of Asphalts and Modified Asphalts."*** The study was sponsored by the Federal Highway Administration (FHWA) under contract number DTFH61-92-C-00170. Work in Task K was a joint effort between the Texas Transportation Institute (TTI) of Texas A&M University and the Department of Civil Engineering at North Carolina State University (NCSU).

The final report is divided, for reasons of readability and ease of documentation, into four volumes: (1) Microdamage Healing - Project Summary Report, (2) Evidence of Microdamage Healing, (3) Micromechanics Fatigue and Healing Model, and (4) Viscoelastic Continuum Damage Fatigue Model.

There were five primary study objectives:

1. Demonstrate that microdamage healing occurs and that it can be measured in the laboratory and in the field.
2. Confirm that the same fracture properties that control propagation of visible cracks control the propagation of microcracks, and determine the effects of microdamage healing on these fracture properties and basic fracture parameters.
3. Identify the asphalt constituents that influence microdamage and microdamage healing.
4. Establish appropriate correlations between microdamage and microdamage healing in the laboratory and in the field.
5. Predict the effect of microdamage healing on pavement performance and develop the appropriate constitutive damage models that account for the effects of microdamage healing on the performance of asphalt concrete pavement layers.

By satisfying the objectives of this research, the FHWA will be able to:

1. Establish the validity and significance of microdamage healing in flexible pavement design and analysis.
2. Identify how microdamage healing can be utilized in pavement design and analysis.
3. Maximize pavement performance life by selecting asphalt binders that match the level of microdamage healing to the level of traffic.

Volume 1: Microdamage Healing - Project Summary Report

Volume 1 is a summary report that chronicles the research highlights of the entire study. Volume 1 describes the success of the project in addressing the project objectives as summarized in the following paragraphs.

The initial research objective was to demonstrate that healing occurs and can be measured both in the laboratory and in the field. Healing was verified on laboratory test samples that demonstrated that dissipated pseudo-strain energy (DPSE) with each cycle of loading, which steadily decreased during cyclic, controlled-strain loading, was recovered after rest periods. The level and rate of the recovered DPSE varied in a logical manner corresponding to changes in the duration of the rest period and the temperature during the rest period. A parameter called the Healing Index (HI) was developed to quantify the magnitude of healing. Furthermore, a Micromechanics Fatigue and Healing Model (MFHM) was developed in this study on the basis of the basic laws of fracture and microcrack growth. This model predicts the size distribution of microcracks and the growth of the microcracks as the fatigue process continues. The model, which is based on a relationship between stiffness loss during the fatigue process (due to microcrack damage) and the rate of change in DPSE, reveals a reduced average length of microcracks in the sample following rest periods. The MFHM model can be used to accurately calculate (by reverse calculation techniques) pertinent material properties and the rate of change in DPSE during the fatigue and healing process at temperatures below 25°C. However, the back-calculated pertinent material properties and the rate of change in DPSE cannot be accurately predicted using the MFHM at temperatures above about 25°C. This is because below 25°C, the change in damage during cyclic loading is almost all due to microcrack growth and healing. However, at the higher temperatures, plastic deformation occurs to a considerable extent, and plastic damage is not accounted for by the MFHM.

Convincing evidence of healing based on field data further verifies the occurrence of and ability to measure microdamage and healing. The stiffness of damaged roadways was found to recover or increase after rest periods where the stiffness was measured using in situ surface wave techniques. Experiments that verify healing were performed on U.S. 70 in North Carolina, the MnROAD project in Minnesota, and the Accelerated Loading Facility in McLean, Virginia.

The second research objective, using the MFHM, which is based on fracture mechanics principles, was to confirm that the same fracture properties that control the propagation of visible cracks also control the propagation of microcracks and determine the effects of microdamage healing on the basic fracture properties and the fatigue life.

The third objective was to identify the asphalt constituents that influence microdamage and microdamage healing. Five asphalts ranging widely in aromatic, amphoteric, and wax contents were considered, and asphalts with low amphoteric and high aromatic contents were found to be better healers. However, the most important relationship between binder properties and healing was based on surface energy, which was shown to be fundamentally related to fracture and healing in a landmark study by Richard Schapery. More specifically, two components of surface energy (the polar and the non-polar component) were found to explain experimental data on the rate of early healing and the development of long-term healing.

The fourth objective was to establish appropriate correlations between microdamage and microdamage healing in the laboratory and in the field. This was accomplished, as evidence verifies that a very significant level of recovery or healing occurs in the field following rest periods, and this level of recovery is in agreement with the magnitude of healing measured in the laboratory.

Finally, the project sought to predict the effect of microdamage healing on pavement performance and to develop an appropriate damage model. Two complementary approaches to the accomplishment of this objective were developed in this research. One was the development of the viscoelastic continuum damage mechanics model (CDM) and the second was the micromechanics fatigue and healing model (MFHM). The CDM can be used to assess fatigue life from either controlled-strain or controlled-stress fatigue experiments and the direct effects of rest periods (healing) on damage. Whereas the CDM offers an assessment of generic damage, the MFHM offers considerable insight into how material properties of the mixture affect fracture rate, healing rate, and the net rate of crack growth or fatigue, which is a balance between fracture rate and healing rate.

Volume 2: Evidence of Microdamage Healing

Volume 2 documents laboratory and field testing that provides the evidence that microdamage healing is real and measurable and that it has a significant impact on pavement performance.

Part of the laboratory experiments to evaluate the impact of rest periods were performed at North Carolina State University (NCSU). In these experiments, fatigue damage was induced through flexural beam experiments. Damage was recorded as the flexural stiffness of the beam became smaller during the flexural fatigue experiment and as the dynamic modulus of elasticity (as measured from impact resonance) became smaller. The experiment included two very different asphalt binders: AAD and AAM. The experiment clearly demonstrated that the rest periods introduced after fatigue damage allowed significant recovery in the flexural and dynamic modulus. The recovery was attributed to the healing of microcracks within the sample. The time of the rest period and the temperature of the sample during the rest period were found to significantly affect the degree of healing. The healing potentials of AAD and AAM asphalt cements were evaluated using four different indicators. Each indicator showed AAM to be a significantly better healer than AAD.

A separate series of laboratory testing was performed at Texas A&M University's Texas Transportation Institute (TTI). These tests consisted of controlled-strain haversine loading direct tensile tests and controlled-strain trapezoidal loading direct tensile tests. The change and rate of change in DPSE were recorded throughout the test and after rest periods introduced during the fatigue tests. The recovered DPSE after the rest period normalized by the DPSE before the rest period defined a Healing Index (HI) term used to quantify healing. Although healing was found to be dependent on the temperature of the mixture during the rest period and the length of the rest period, it was also found to be highly dependent on the type of asphalt cement. Asphalt AAM was found to provide much better healing properties than asphalt AAD, which is in agreement with the work of NCSU where significantly different testing protocols were used.

A discussion is presented in Volume 2 that explains the importance of transforming the dissipated energy into pseudo-dissipated energy in order to accurately evaluate the relative ability of the various mixtures to heal. The transformation to pseudo-strain energy can be tedious and painfully slow. However, a linear transformation protocol is presented that is acceptably accurate and efficient. This protocol was used in this research to calculate pseudo-dissipated energies for the mixtures compared.

The TTI laboratory work demonstrated that several factors may influence the measure of microdamage healing apart from crack healing: molecular structuring or steric hardening, temperature confoundment, and stress relaxation during loading and rest periods. Each factor is discussed with respect to its role in influencing microdamage and microdamage healing. The conclusions are that: 1) molecular structuring is not of significance or importance for the rest periods and test protocols used in this study; 2) temperature increase upon loading or dissipation during rest periods was minimal in these experiments and had an insignificant impact on measured properties due to the nature of the test protocol, number of loading cycles used, and length of rest periods; and 3) stress relaxation is accounted for in the determination of the pseudo-strain energy data as they relate to microdamage healing.

The influence of several factors as they affect microdamage healing (the healing index) are discussed. These include the effects of low density polyethylene (LDPE) as an asphalt additive, the effects of age-hardening (including the effects of hydrated lime as an inhibitor of hardening), the effect of five different binders (exhibiting very different compositional properties), and the effect of different mixture types (dense graded mixtures versus stone mastic type mixtures).

The most notable finding presented in this volume is the difference in healing indices among the five virgin binders evaluated. A strong relationship between surface energy of the binder and the magnitude of healing and the rate of realization of maximum healing is presented. This relationship agrees with the fundamental (fracture mechanics-based) explanation of fatigue presented in Volume 3. In this fundamental relationship, the fatigue process is presented as a balance between the fracture during loading and healing or recovery during periods of rest.

Volume 2 completes the evidence of microdamage healing with convincing field evidence. Wave speed and attenuation measurements were made on in situ pavements. The stress wave test and analysis successfully detected fatigue damage growth and microdamage healing of asphalt pavements (at the FHWA's Turner-Fairbank Highway Research Center - Accelerated Loading

Facility) with different asphalt layer thicknesses and viscosities and demonstrated the importance of microdamage healing during rest periods on pavement performance. The ability of stress wave testing to measure microdamage and healing in the field was further evaluated at the Minnesota Road Project (Mn/ROAD) on seven pavement test sections at the site. The results further confirmed that the stress wave analysis can be used to monitor microdamage growth and healing in the field. The conclusion of the field study was that, although healing of asphalt concrete pavements in the field is more difficult to measure than in the controlled setting of a laboratory, it can be accurately detected using stress wave analysis. The fact that healing does occur in pavements in the field during rest periods suggests that the performance and service life of the pavement will be increased if rest periods are introduced, or if binders are used that heal more quickly and completely.

Volume 3: Micromechanics Fatigue and Healing Model

Volumes 3 and 4 present two different ways of describing the fatigue cracking in mixes. In both volumes, the sample being tested is damaged. The two approaches differ in their ways of characterizing cracking. In Volume 3, it is assumed that all of the damage is due to cracking and obeys the fracture and healing laws that have been established for viscoelastic materials. In this approach the material properties that are relevant to these fracture and healing laws may be measured independently of the sample that is tested in fatigue. The resulting model of fatigue cracking and healing is the Micromechanics Fracture and Healing Model (MFHM). In Volume 4, the sample is assumed to suffer a generic "damage" with which no material properties are associated. Instead, model coefficients are found by analysis of the sample DPSE data. The resulting model is the continuum damage model (CDM). Volume 3 contains a description of the tests that were run and interpreted using the MFHM at 4°C, 25°C and 40°C. At the lower temperatures (4°C and 25°C), the MFHM model was used to calculate the cohesive fracture and healing surface energies, which were measured independently using a Wilhemy Plate apparatus. The calculated and measured values matched well within reasonable experimental error. However, at 40°C, the calculated surface energies did not match the measured values, indicating that a mechanism other than fracture and healing was operating at the higher temperature. The most likely damage mechanism to operate at the higher temperature is plastic flow. This suggests that a continuum damage model (CDM) at the higher temperatures will probably be of a different form with different sets of model coefficients than what was found to fit the fracture and healing damage mechanism at the lower temperatures as discussed in Volume 4. The most likely dividing line between the fracture and healing mechanism and the plastic flow mechanism is the stress free temperature of the asphalt concrete mixture.

Three events occur simultaneously in asphalt mixtures under strain-controlled fatigue loading. These are relaxation, fracture, and healing. Relaxation of stress is a direct result of asphalt molecular structure. Fracture can be regarded as the growth of microcracks or macrocracks during loading, and healing is the recovery of the asphalt structure during rest periods. Healing is at least partly due to the recovery of bonding strength at the closure of fracture faces. The relaxation and healing mechanisms extend the performance life of asphalt mixtures while fatigue damage degrades their quality.

The theories of fracture mechanics are well established for time-independent materials, such as metals. However, analysis methods to characterize the behavior of time-dependent viscoelastic materials are rare. A number of approximate interrelationships between linear elastic and viscoelastic properties have been developed; however, they are only applicable to quasi-static problems. Finding a closed-form solution to quantify the response of viscoelastic materials under general loading conditions is one of the objectives of a portion of the study described in this volume. A second objective of this portion of the research was to show that the same fracture properties that control the propagation of visible cracks control the propagation of microcracks.

It is a third objective to show that the microfracture and healing properties that can be calculated from the measured results of tensile fatigue tests match the cohesive fracture and healing properties of the asphalt binder that can be measured independently. It is this third objective which demonstrates closure: The microfracture and healing theory proposed in this report actually does predict the measured results.

An extended background review of the literature, which supports much of the development of the models presented in this volume, is presented in the Ph.D. dissertation of Chen (1997). This volume presents a finite element model, which is used to calculate the fracture properties of asphalt mixtures and to calculate damage behavior (average crack length and density of crack distribution) during fatigue testing. The fracture properties and damage assessment is based on dissipated pseudo-strain energy, which is recorded throughout the test. Based on the microfracture and healing model, a fundamental relation of viscoelastic fracture was derived and is presented in this volume. This fundamental law is used to describe the rate or speed of fracture and the rate or speed of microfracture healing based on fundamental properties of the mixture and its components. The law defines the fatigue process as being a balance between the rate of fracture and the rate of healing. The fundamental relationship identifies component and global mixture properties that affect fracture and healing. Tests to measure these material properties show potential for development into specification tests. Among these are the surface energy tests for binders and aggregates and mixture tensile and compressive compliance tests. The reasonableness of the approach is demonstrated by the fact that the fundamental relationship of viscoelastic fracture mechanics was used to calculate fracture and healing surface energies from actual fatigue test dissipated pseudo-strain energy data, and fundamental mixture fracture properties were calculated from these data. The calculated mixture surface energies were within a reasonable range of those measured separately for the binder and mixture as discussed in Volume 3.

The analytical methods presented in this volume demonstrate a reduction in average microcrack length following rest periods and that the same fundamental fracture parameters that influence macrocrack growth (fractures larger than about 7.5 mm) also control microcrack growth.

Volume 4: Viscoelastic Continuum Damage Fatigue Model of Asphalt Concrete With Microdamage Healing

A mechanistic approach to fatigue characterization of asphalt-aggregate mixtures is presented in this volume. This approach is founded on a uniaxial viscoelastic constitutive model that accounts for damage evolution under cyclic loading conditions. The elastic-viscoelastic correspondence principle is applied in order to evaluate damage growth and healing in cyclic loading separately from time-dependent characteristics of the material. The damage growth during loading cycles and healing during rest periods are modeled using work potential theory, a continuum damage theory based on thermodynamics of irreversible processes. Internal state variable formulation was used in developing the analytical representation model. Tensile uniaxial fatigue tests were performed in the controlled-strain mode with different strain amplitudes to determine model parameters. The resulting constitutive model successfully predicts the damage growth of asphalt concrete under monotonic loading at varying strain rates and damage growth and recovery due to complex loading histories, in both controlled-strain and controlled-stress modes, composed of randomly applied multi-level loading with different loading rates and varying durations of rest.

Fatigue lives of two different mixtures were predicted with reasonable accuracy using the constitutive model for the constant stress-strain amplitude cyclic loading histories with and without rest periods. A standard uniaxial fatigue test protocol is proposed by simplifying the experimental approach used in developing the constitutive model.

VOLUME SUMMARY

Laboratory Testing

This volume documents the laboratory testing protocols and presents the experimental designs followed. This volume documents mixture testing protocols used to assess fatigue damage and mixture properties related to fatigue. These tests include controlled-strain haversine loading direct tensile tests, controlled-strain trapezoidal loading direct tensile tests, and flexural beam fatigue tests where damage and healing were evaluated based on change in pseudo-stiffness and based on vibrational analysis. This volume also addresses the protocols used to establish surface energies for the binders evaluated and for the aggregates used in the testing matrix.

This volume presents the results of the mixture tests with emphasis on the healing index as a measure of microdamage healing. A discussion is presented that explains the importance of transforming the dissipated energy into pseudo-dissipated energy in order to accurately evaluate the relative ability of the various mixtures to heal. The transformation to pseudo-strain energy can be tedious and painfully slow. However, a linear transformation protocol is presented that is acceptably accurate and efficient. This protocol was used in this research to calculate pseudo-dissipated energies for the mixtures compared.

Several factors may influence the measure of microdamage healing apart from crack healing: molecular structuring or steric hardening, temperature confoundment, and stress relaxation during loading and rest periods. Each factor is discussed with respect to its role in influencing microdamage and microdamage healing. The conclusions are that: 1) molecular structuring is not of important significance for the rest periods and test protocols used in this study; 2) temperature increase upon loading or dissipation during rest periods is not of important significance due to the test protocol, number of loading cycles used, and length or rest periods; and 3) stress relaxation must be accounted for in the presentation of data as they relate to microdamage healing.

The influence of several factors as they affect microdamage healing (the healing index) are discussed. These include the effects of polymers as an asphalt additive, the effects of hydrated lime on aged mixture as an asphalt additive, the effect of five different binders (exhibiting very different compositional properties), and the effect of different mixture types (dense graded mixtures versus stone mastic type mixtures).

The most notable finding presented in this chapter is the difference in healing indices among the five virgin binders evaluated. A strong relationship between surface energy of the binder and the magnitude of healing and the rate of realization of maximum healing is presented. This relationship agrees with the fundamental (fracture mechanics-based) explanation of fatigue presented in Volume 3. In this fundamental relationship, the fatigue process is presented as a balance between the fracture during loading and healing or recovery during periods of rest.

Field Testing

Field testing using stress wave analysis was performed on pavement sections at the accelerated loading Facility (ALP) at the FHWA's Turner-Fairbanks Lab in McLean, Virginia, and at the Minnesota Road Pavement Project (Mn/Road). Field testing verified the ability of stress wave analysis to detect and document microcrack damage and microdamage healing.

CHAPTER 1: EVALUATION OF MICRODAMAGE HEALING BASED ON LABORATORY DIRECT TENSILE TESTING AND CONSIDERING THE EFFECTS OF BITUMEN COMPOSITION AND SURFACE ENERGY

Research Approach

Microdamage healing was considered to be a function of a number of mixture variables, which are discussed in the following section entitled "General Experiment Design." The influence of these variables on healing rate was evaluated as discussed in the General Experiment. However, it was concluded that a more meaningful direction was to concentrate on the effect of properties that are not only logically or empirically related to microdamage growth and healing but also on those that can be related in a definitive way based on established fracture theory. This led to the study of healing rate or rate of recovery of asphalt mixtures as influenced by chemical composition, and specifically the surface energy of the asphalt binders via the Wilhelmy Plate method. The experiment design developed to assess the effect of bitumen composition and surface energy is referred to as the "Primary Experiment."

The healing rate as calculated and quantified from stress-strain data was acquired from fatigue tests performed on the Cox and Sons 7000 SHRP shear machine. This healing quantity is also called the *healing index*, and compares the energy dissipated in a fatigue test cycle prior to a rest period (the 'damaged' cycle) to the identically applied cycle ensuing a rest period (the 'healed' cycle) and is represented by the following equation:

$$HI = \frac{\Phi_H - \Phi_D}{\Phi_D} \tag{1}$$

where ϕ_D is the pseudo-strain energy from the cycle prior to the rest period (damaged) and
ϕ_H is the pseudo-strain energy following the rest period (healed).

It bears note that the healing indices are based on pseudo energy, using the quantities of stress and pseudo-strain. This transformation was applied linearly to the test data to remove the obfuscating effects of creep and relaxation from the calculated energy dissipation in the fatigue test data. The pseudo-energy transformation is covered extensively in many works on viscoelastic behavior and is a standard evaluation method for these materials.

Primary Experiment Design

Healing rates were determined in the primary experiment for a group of mixtures featuring five different binders combined with Watsonville Granite (SHRP-RB) aggregate in a standard mix design; this is detailed in the laboratory testing program. Asphalt binders were chosen according to chemical compositional differences to fit factorial matrices (Table 1) with the help of Dr. Jan

Branthaver (1997) at Western Research Institute (WRI). This matrix serves as a guide for both direct evaluation of healing rates with respect to chemical composition and to assess the effect of surface energy. Direct evaluation of the compositional effects was performed using a statistical contrast/comparison test of the mixture data. As evinced in Table 1, the selected SHRP binders vary in wax, amphoteric, and aromatic quantities.

Table 1. Asphalt Composition Matrices Provided by Dr. Jan Branthaver of Western Research Institute (1997).

		Wax Content	
		High	**Low**
Amphoteric Content	High	AAB-1	AAD-1
	Low	AAM-1	AAG-1

		Wax Content	
		High	**Low**
Aromatic Content	High	AAF-1	AAG-1
	Low	AAM-1	AAD-1

The primary factorial experiment, Table 2, is actually a subset of the general experiment, Tables 3 and 4. Succinctly stated, the primary experiment is intended to provide a direct comparative analysis of surface energy characteristics of five binders to their respective chemical composition via a contrast-comparison statistical analysis. Additionally, the experiment is designed to evaluate the effect of bitumen surface energies on the healing ability of asphalt additives that are identical accept for the binder used.

Table 2. Partial Factorial of Experimental Design for Virgin SHRP-Classified Asphalt Binders (Primary Experiment).

Aggregate	**Mix Type**	**Binder**				
		AAB-1	**AAD-1**	**AAF-1**	**AAG-1**	**AAM-1**
Watsonville Granite - SHRP (RB)	Dense-Graded (DG)	9*	9	9	9	9

* Number of samples fabricated and tested.

Table 3. Partial Factorial of Experimental Design for Virgin SHRP-Classified Asphalt Binders (General Experiment).

Aggregate	**Mix Type**	**Binder**				
		AAB-1	**AAD-1**	**AAF-1**	**AAG-1**	**AAM-1**
Watsonville Granite - SHRP (RB)	Dense-Graded (DG)	9*	9	9	9	9
	Stone Matric (SMA)		9			9
Brownsville Texas Limestone	Dense-Graded (DG)		3			3

*Number of replicate samples tested.

Table 4. Partial Factorial Experimental Design for Binders Containing Additives (General Experiment).

Aggregate and Mix Type	**Binder**							
	AAM + LDPE	**AAD + LDPE**	**AAM + SBS**	**AAD + SBS**	**AC1 Aged**	**AC2 Aged**	**AC1+ Lime Aged**	**AC2+ Lime Aged**
Dense-Graded Aggregate RB	3*	3	3	3	3	3	3	3

* Number of replicate samples tested

General Experiment Design

A generalized experiment design (Tables 2 and 3) was developed to assess the effects of:

1. Binder composition as previously discussed.
2. Aggregate mineralogy (granite versus limestone).
3. Mixture type (dense-graded versus stone mastic).
4. Effect of additives.
5. Effect of aging.

Each virgin binder (Table 3) required nine samples, and tests were performed with 2-minute rest periods inserted every 100, 200 and 300 cycles (three replicate samples for each test). Modified binders (Table 4) were evaluated in dense-graded mixes with granite (RB) aggregate, and 2-minute rest periods were induced every 200 cycles.

Data from the generalized experiments were analyzed to assess all five effects. However, the strong emphasis of the analysis was placed on the primary experiment, which evaluated the influence of binder composition and binder surface energy on microdamage healing.

The general experiment addresses the five effects previously listed as these were determined to logically influence type and mode of fracture growth and, perhaps, healing. For example, bitumen and aggregate bond or compatibility must influence their fracture and healing properties. The effect of polymer additives should have some influence on the binder rheology and hence on fracture rate and healing rate. These polymer effects include changing elastic-viscous characteristics and energy dissipation properties through microcrack pining due to enclusions. Aging embrittles the binder and the mix and should make the mix substantially more susceptible to fracture and less likely to heal. Hydrated lime is known to reduce the effects of oxidative hardening and hence was introduced in the general experiment to assess possible mitigation of fracture effects and enhancement of healing effect on aged mixtures. Finally, mixture type should affect the fracture and healing behavior as mixes with high mastic volumes (bitumen and smaller than 75 micron aggregate) may promote cohesive fracture whereas traditional, lower asphalt content, dense-graded mixtures may be more susceptible to adhesive rather than cohesive fracture. Cohesive fractures (within the mastic) are logically more amenable to healing.

Although the effects evaluated in the general experiment are important to understand, a theoretical link was established between surface energy and fracture and healing rate. Therefore, a greater emphasis was placed on the primary experiment, which evaluates the link between surface energy and the five binders (Table 1) and healing level and rate. This relationship will be established in the following sections.

Surface Energy of the Bitumen

Asphalt concrete is a composite blend of bitumen and aggregate of a range of sizes. Unlike other composites, comparatively little has been done to thermodynamically characterize the asphalt-aggregate bond in terms of adhesion and cohesion. The thermodynamic change in the surface free energy is the theoretical work required to break an interface, or form one. This energy required to sever and reform an interfacial bond certainly is related to the characteristics of crack growth and crack healing. More energy required to sever a bond in the surrounding media means more work that will have to be done to propagate the crack (other factors being equal). If less energy is required to re-establish that bond, then more healing is facilitated.

Crack propagation and healing within the composite asphalt mixture occur as one of two types, **adhesive** or **cohesive**. The Adhesive mode implies interaction between two materials, and in an asphalt mixer this is the asphalt-aggregate interface. The Cohesive mode involves only the mastic (bitumen and ultra-fine aggregate). Cracks propagate through the means of least resistance, so it is implied that the lower energy route (adhesive or cohesive) will dictate its respective mode of fracture. Crack healing occurs only in the presence of fracture, so its rate should be dependent on the type of fracture most prevalent in a given mix as well as the surface energy germane to each mode of healing. Given that the fatigue progression of an asphalt-aggregate composite is a succession of and balance between fracture and healing, the cohesive properties of the bitumen and the adhesive properties of the asphalt-aggregate bond exert an important influence on the life of these mixtures under repetitive loading.

The cohesive and adhesive bonding interactions of asphalt-aggregate systems are chiefly influenced by two effects: the Lifshitz-van der Waals interactions of electron shells of neighboring molecules, and acid-base interactions between constituent molecules (Good and Van Oss, 1992). Acid-base effects generally dominate for asphalt-aggregate composites. They are particularly important to the development of strong adhesive bonds that are resistant to water (Labib, 1992). The acid-base interaction component consists of two components of its own, a Lewis acid parameter and a Lewis base parameter. The total surface energies of the asphalt are determined from the Lifshitz-van der Waals component and the acid and base components.

Surface Energy Testing

Binder characterization by surface energy characteristics was performed using the Wilhelmy Plate method executed at Texas A&M University. The experimental setup is diagramed in Figure 1 and centers on the use of a highly sensitive balance, the Cahn C2000, married to a computer-controlled motor and a data acquisition module.

The binder to be tested was first prepared by heating a small tin (about 100 grams worth) of asphalt to 80°C and mixing the sample thoroughly for about 30 minutes. This step is meant to render as homogeneous a sample as possible when the asphalt is parceled onto the glass plates. Then, cleaned glass plates are dip-coated with the asphalt and set in a desiccator to dry to a stable condition where the asphalt is immobilized. The coated glass plates remain in the desiccator overnight, generally no more than 16 hours.

The specific plate to be tested is attached to the Cahn balance apparatus as diagramed in Figure 1. The plate hangs from the end of the balance just above an open container of a chemically documented fluid. From this point, the experiment has three measured states, detailed in Figure 2:

1. The plate hangs in the air;

2. The plate is lowered slowly into the fluid until the contact angle between the coated plate and the fluid reaches an equilibrium state, and is then measured. This is called

the **wetting** cycle; and

3. The plate is raised slowly out of the fluid until the contact angle between the coated plate and the fluid reaches an equilibrium state, and is then measured. This is called the **dewetting** cycle.

Throughout the experiment, the force (“F” in Figure 2) is sampled by the data acquisition module, and the applied plate velocity (“V_p” in Figure 2) is tightly controlled. The fluids used in these tests were water, glycerol, and ethylene glycol. Both the advancing and receding angles from the wetting and de-wetting processes are necessary to ensure accuracy with this method due to the chemical heterogeneity of asphalt. Numerous trials are also necessary, as the method is very sensitive to the applied velocity and replicate samples are required to ensure that successful replicate verification has been achieved. Applying a velocity that is too great or too small can nullify the attempt to get an equilibrium contact angle. A sample data plot from a trial run of a Dutch bitumen appears in Figure 3. The beginning of the experimental run is marked on the data plot with an ‘X’.

The Wilhelmy Plate results are summarized in Table 5.

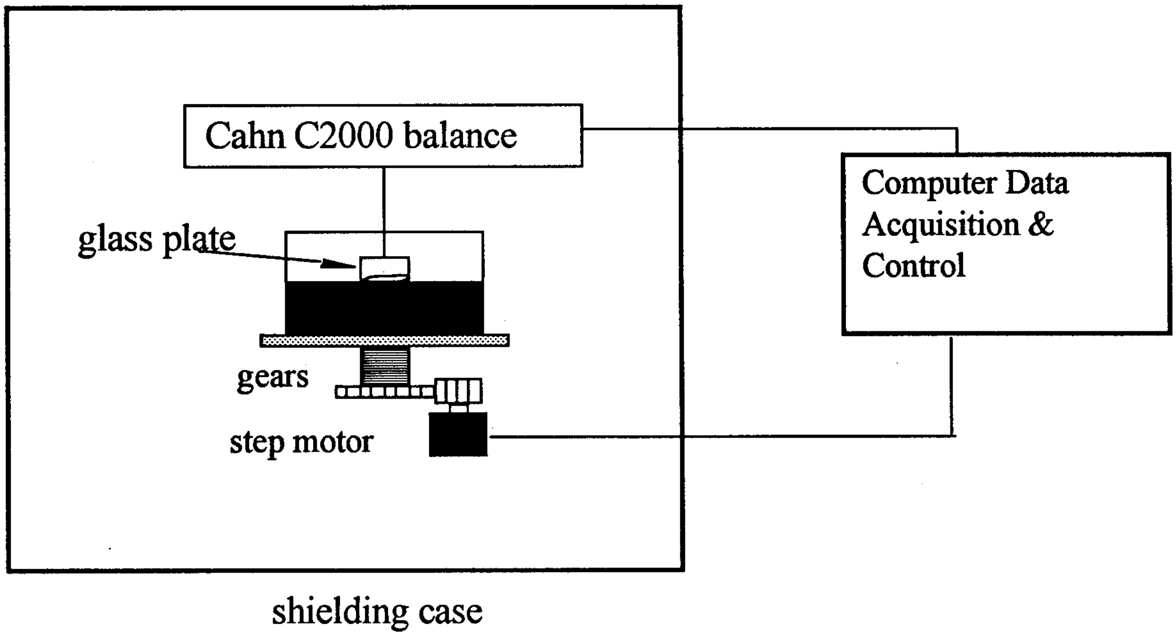

Figure 1. Schematic of the Wilhelmy Plate Experiment Centered About the Cahn C2000 Balance.

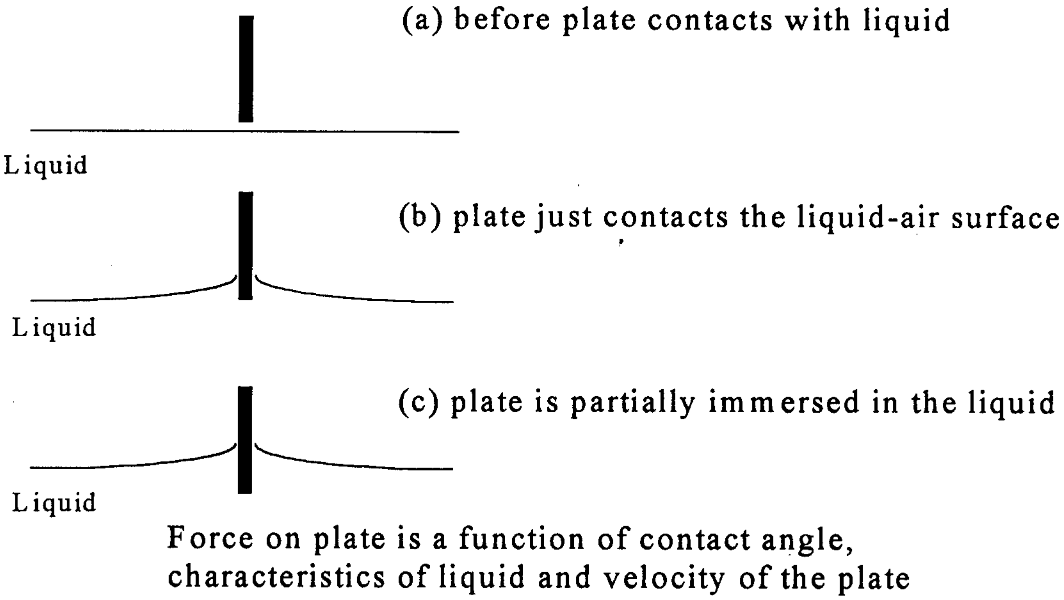

Figure 2. The Three Possible Positions of the Coated Glass Plate During the Wilhelmy Plate With the Pertinent Force Relationships Necessary to Interpret the Acquired Data.

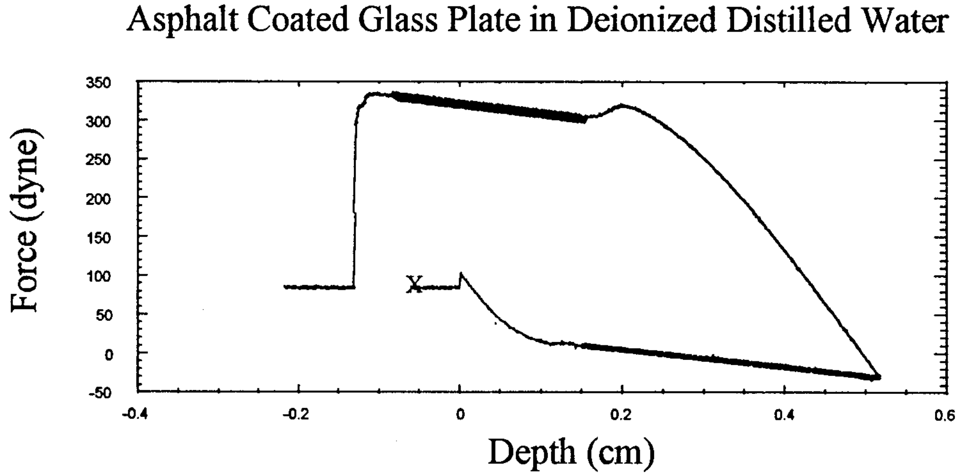
Asphalt Coated Glass Plate in Deionized Distilled Water

Figure 3. Actual Output of the Cahn C2000 Balance During a Wetting/Dewetting Cycle of a JG31-1 Binder.

Table 5. Surface Energies of Various Asphalts (mJ/M^2).

Material	Γ	σ	Γ^{LW}	σ	Γ^{AB}	σ	$\Gamma+$	σ	Γ^-	σ
AAB-1	10.1	0.5	9.4	0.5	0.7	0.2	2.4	0.4	0.06	0.03
AAD-1	14.0	0.2	13.6	0.2	0.3	0.1	0.1	.06	0.2	.05
AAF-1	10.0	0.4	6.2	0.1	3.8	0.4	4.3	0.3	0.8	0.1
AAG-1	13.0	0.1	8.2	0.1	4.8	0.1	4.8	0.1	1.2	0.1
AAM-1	58.2	0.1	5.3	0.1	2.9	0.1	5.6	0.2	0.4	0.1

In Table 5,

Γ = total surface energy,
σ = standard deviation,
Γ^{LW} = Lifschitz-van der Waals component,
Γ^{AB} = acid-base component,
Γ^+ = acid component of surface energy density (SED), and
Γ^- = base component of SED.

Surface energies were analyzed directly for variation with chemical composition and also with healing rates measured in laboratory tests. The compositional differences were modeled by a statistical linear contrast. The relationships to be explored between surface energy and healing rate are suggested based on two proposed models of fracture healing in viscoelastic materials: one proposed by Lytton in this research project (Lytton et al., 1998), and one by Dr. Richard Schapery (1988).

Models to Explain Healing Rate in Viscoelastic Materials

This work compares two proposed constitutive healing rate models derived from the same first principles of fracture. Each model is derived from Schapery's fundamental relation of cohesive fracture mechanics (1983):

$$2\Gamma_f = E_R \, D_f \, (t_d) \, J_v \tag{2}$$

where Γ_f = the surface energy density of a crack surface (units: FL^{-1}),
E_R = reference modulus (units: FL^{-2}) used to make equation (2) dimensionally correct,
$D_f(t_d)$ = tensile creep compliance at time t_d that is required for a crack to move through a distance that is the length of the process zone ahead of the crack top (units: F^{-1} L^2), and

J_v = the viscoelastic J-integral, which is the change in dissipated pseudo-strain energy (PSE) per unit of crack area from one tensile load cycle to the next (units: FL^{-1}).

Equation (2) represents an energy balance: the energy given up on the right-hand side of the equation is taken up by the newly created crack surfaces on the left-hand side of the equation.

Schapery's Model

Schapery (1988) developed a model for healing in linear, isotropic viscoelastic materials assuming " interfacial forces of attraction *and* external" or applied "loading." The inclusion of surface forces in Schapery's model is significant, accounting for the case where complete contact of the fractured surfaces is not initially achieved by dominating loading. Rather the healing process is driven in significant part by the attractive forces germane to the fractured surface. This makes for a self-sustaining process available in some quantity to all systems, virtually regardless of instantaneous loading regime. The surfaces in Schapery's scheme are assumed to be "locally flat" but not necessarily so throughout the cracked regime. After expanding the first principles approach to healing speed, Schapery (1988) derived a relationship between healing speed, $\dot{h}_2$, and several material properties including surface energy:

$$\dot{h}_2 = \left[\frac{2\gamma_m E_R^2 D_{1c} \Gamma_h}{(1 - \nu^2)\, c_m^{1/m}\, H_v}\right]^{1/mc} \beta \tag{3}$$

Where:

E_R = reference modulus, a constant derived of the stress transformation,
ν = Poisson's ratio,
D_{1c} = compressive creep compliance constant (D_0 is assumed to be zero),
H_v = healing integral,
Γ_h = wetting surface energy,
m_c = slope of compressive,
γ_m = creep compliance versus time, and
C_m = average microcrack length.

Key in this equation is the representation of healing rate $(\dot{h}_2)$ as being *directly* related to the surface energy density, i.e., a greater surface energy density signifies a greater potential for healing, all other conditions being the same. Lytton's model contends the opposite. It also bears note that the constant term of the power law compliance, D_o, is assumed to be negligible. If this is not the case, then more complicated ramifications ensue.

Lytton's Model

Lytton (Lytton et al., 1998) developed a similar model to explain the healing rate between fracture surfaces essentially by reversing the fracture laws evolved in his microdamage theory in the orientation of healing. The recovery rate depends essentially on the same properties that appear in Schapery's earlier model, but a key difference is the assumption that the surface energy is an inhibitor of healing. Viewed from a conservation standpoint, the surface energy is an energy density required to close a given area of crack face. The lower this surface energy density is then the greater is the amount of healing that can proceed under otherwise equal conditions. A higher surface energy density reduces the amount of crack surface that can be closed with the same amount of available energy. This model was <u>not</u> developed with the assumption that there is any sort of attractive force between asphalt surfaces on either side of a crack face. Lytton derived the following relationship between "healing speed" and surface energy, among other factors:

$$\dot{h}_1 = \left[\frac{(k_{th}) D_{1c}\, E_R\, H_V}{2\Gamma_h}\right]^{1/m_c} \beta \qquad (4)$$

Where K_{th} is a fitting constant.

Note the *inverse* relationship between healing rate and surface energy.

These divergent models are rooted in the same first principles and predict opposing effects. Lytton includes a new form of surface energy and a somewhat different reference modulus, while Schapery and Lytton both included a healing integral and compressive creep properties.

Laboratory Testing Program

The models defined above were compared with the data sets, acquired through the general and primary experiments. The general experiment is presented in Tables 3 and 4 while the primary experiment is presented in Table 2. Testing performed at Texas Transportation Institute included direct tensile fatigue testing of 102-mm-high by 102-mm-diameter specimens of asphalt mixes. Each sample was fabricated in accordance with SHRP A-003A mixing and compaction protocols using the California Kneading compactor; these processes are detailed in subsequent sections. Acceptable specimens (those meeting volumetric control requirements) were tested on a Cox and Sons 7000 SHRP shear test machine by applying a haversine strain wave to the samples in a direct tensile mode. To be deemed acceptable, samples were required to meet strict air void and binder content tolerances of 4.0 ± 0.5% air voids and 5.0 ± 0.1% asphalt binder by total mixture weight, respectively.

All of the above materials were stored in a dry, climate-controlled room until tested. The partial factorial experiment designed to assess the effect of bitumen composition and bitumen surface energy and healing potential (as defined by the healing index) is presented in Table 2.

Materials Tested

Samples were fabricated to meet the demands of the general and primary experiments and the test protocol established in the preceding sections.

In the primary experiment the specimens were produced using Watsonville Granite (RB) aggregate mixed with binders AAM, AAB, AAG, AAF, or AAD. These bitumens for the microdamage healing study were acquired from the SHRP Materials Reference Library (MRL).

Additionally, 600 kilograms of RB aggregate were donated by Granite Rock, Inc., of Watsonville, California, in order to fill a requirement for material passing the No. 4 sieve but retained on the No. 8 sieve and mineral fines (minus 200 sieve-size materials). These size fractions of RB aggregate were not readily available through the MRL stockpile.

Several hundred pounds of Brownwood limestone were received from Vulcan Materials in Brownwood, Texas. No gaps in size faction availability were exhibited during the sieving process.

Upon delivery of the materials, each were inspected and inventoried. One each of the 5-gallon containers of the asphalts were set aside to be split into smaller containers for mixing in accordance with SHRP A-003A protocol. The resulting asphalt quantities were kept in quart paint cans in a 10 C storage room.

The aggregates were sieved as needed into size fractions necessary to meet the SHRP A-003A medium gradation No. 2 and stored in clean 5-gallon white paint buckets marked to indicate the contents. This gradation is presented in Table 6.

Devcon Two-Ton Epoxy or Plastic Steel Epoxy was used to glue the specimens to testing platens.

Table 6. Aggregate Gradation Used in Fabrication of Specimens for Controlled-Strain Tensile Fatigue Testing.

Sieve Size, mm	**Percent Passing By Mass**	**Percent Retained on Each Sieve By Mass**
25	100	0
19	95	5
12.5	80	15
9.5	68	12
4.75	48	20
2.36	35	13
1.18	25	10
0.600	17	8
0.300	12	5
0.150	8	4
0.075	5.5	2.5
Pan		5.5

All of the above materials were stored in a dry, climate-controlled room within the labs until they were required.

Asphalt Concrete Specimen Fabrication Protocol

The aggregate was weighed and separated into specimen portions as prescribed by SHRP A-003A medium gradation No. 2 and placed overnight in an oven set to the appropriate mixing temperature prescribed in the protocol. The binder was then placed in the same oven (the following morning) until it reached the prescribed temperature. The binder was then machine-mixed with the aggregate using a Hobart mixer. The mixing lasted no more than 2.5 minutes. Once mixed, the specimen was divided into three portions of 650-700g each and placed in a 116 C oven and allowed to warm to compaction temperature.

Compaction was performed using a Cox kneading machine to a target air voids content of 4.0 percent ± 0.5 percent. The cylindrical (102 mm by 102 mm) mold was heated in the mixing oven prior to compaction, and the specimens were probed with a thermometer to ascertain when the compaction temperature of 116 C was reached. Once ready, the specimens were compacted with the following compactive effort per layer:

Lift	Blows	Pressure
1	20	1413 kPa
2	30	1413 kPa
3	40	1413 kPa

The specimens were allowed to cool, extruded from the molds, and later tested for air void content. Those which met the air voids requirement were marked, wrapped in plastic, and stored in a 25°C room prior to testing to retard aging. Specimens were moved from this controlled environment only to be glued to platens and subsequently tested.

Testing Methodology

The direct tensile testing protocol development was not a trivial task. The evolution of the development of an acceptable protocol involved the ability to capture a sufficient amount of data for analysis during testing. Furthermore, it was necessary to be able to analyze the results.

A direct tensile fatigue test with haversine strain wave application was developed to provide fracture properties of the mixture, the healing index after various levels of damage, a cumulative documentation of dissipated energy (from which microcrack growth can be determined), and the number of cycles to fatigue failure.

The haversine strain wave fatigue test was developed in early 1995 at TTI. The haversine wave test was performed on the Cox and Sons 7000 SHRP Shear Tester (SST Machine). The Cox machine features a self-adjusting gain function that can change settings dynamically as the specimen accumulates damage throughout a given fatigue test. This permits greater precision in attaining the programmed strain levels as the specimen properties change with accumulated damage.

The fatigue test procedure was initiated when the specimens were removed from the climate-controlled storage area. First, the specimen height and diameter were precisely measured. These measurements were recorded along with other pertinent observations, such as any noticeably large surface voids or irregularities on the sample surface. A thin layer of Devcon Two-Ton Epoxy was then applied to the ends of the specimen. This epoxy was used to bond specialized end caps of the specimen for tensile testing in the Cox machine. The epoxy was allowed to set in the gluing rig, which applied a 23-kg compressive load for 15 minutes after which the sample was removed. The epoxy was cured overnight.

Fatigue Test

The 102-mm by 102-mm fabricated specimens were tested using a haversine wave-based, strain-controlled test with rest periods introduced at varying intervals. In the test a trapezoid-shaped strain wave was initially applied that was used to determine tensile and compressive creep properties from the data acquired during the plateaus in the regime. The compliances are of a pure (single-term) power law form and were developed through a regression technique. Following the initial trapezoidal loading, the samples were allowed to rest for 2-minutes and were subsequently cyclically loaded using haversine-shaped strain waves. This wave shape is considered to represent the gradual build-up and subsequent dissipation of the load transmitted to the pavement by a moving wheel. The commanded signal called for a peak strain of 320 microstrain applied over a period of 0.10 second. This was immediately followed by a reciprocating movement to zero strain at the same rate for a total haversine wave duration of 0.20 seconds. The zero strain was then held for 0.40 seconds prior to the next wave repetition. Data plots depicting the commanded strain and the resulting stresses generated by the specimen reaction appear in Figures 4 and 5.

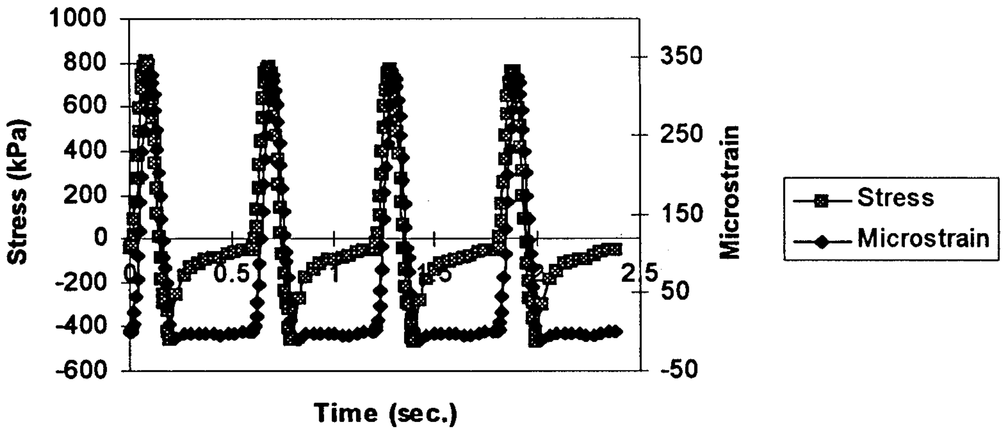

Figure 4. Commanded Haversine Strain Wave and Stress Reaction for Specimen AAD #1.

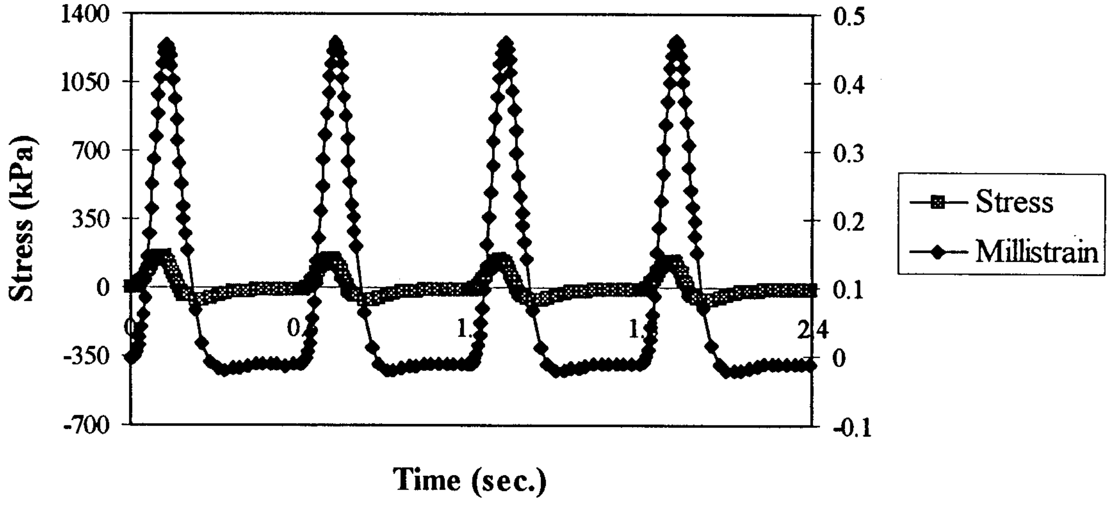

Figure 5. Commanded Haversine Strain Wave and Stress Reaction of Specimen AAM #1.

Development of Haversine Strain Wave Fatigue Test Protocol

The haversine wave test is capable of applying a loading regime somewhat resembling that experienced by an asphalt pavement in service and producing data in a format accessible to analysis, interpretation, and transport.

In its initial form, the haversine wave-based fatigue test was very useful for empirical analysis but resulted in difficulties when microdamage analysis was first attempted. The finite-element program used to backcalculate fracture parameters lacked boundary value information necessary to initiate the analysis. Attempts to calculate boundary conditions, such as a suitable reference modulus and relaxation stiffnesses, were not successful based on the data from the original haversine wave fatigue tests. Additionally, the solutions originally developed for the analysis of the first-generation trapezoid wave fatigue tests performed in phase 1 of this study were no longer valid when applied to a haversine wave function. The fatigue test was altered so that the output data were more suitable for microdamage analysis by commanding a trapezoidal strain wave at the beginning of each test with sufficient frequency of data sampling to permit the establishment of boundary conditions indigenous to each sample. A sample plot of this waveform is represented in Figure 6. Additionally, a new solution was developed to backcalculate the pseudo-strain and pseudo-stress relationships in a numerically closed form.

The primary characteristic associated with the fatigue test is the application of a haversine tensile strain wave of short duration. In the test's earliest form, the commanded signal called for a peak strain of 450 microstrain applied over a period of 0.10 second. This was immediately followed by reciprocating movement to zero strain at the same rate for a total haversine wave duration of 0.20 seconds. The zero strain was then held for 0.40 seconds prior to the next wave repetition. Data plots depicting the commanded strain and the resulting stresses generated by the specimen reaction appear in Figures 4 and 5.

This test approach used the Cox and Sons 7000 Shear Test System, also known as the SHRP Shear Tester. Previous attempts to perform the high-speed, high-strain haversine wave test proved unsuccessful on the MTS machine used to execute cyclic trapezoid wave-strain-controlled settings. The specimen accumulates damage throughout a given fatigue test. The Cox 7000 testing device permits greater precision in attaining the programmed strain levels as the specimen properties change with accumulating damage.

In summary, a trapezoidal strain wave was applied to each virgin specimen to determine data necessary to establish boundary conditions and to establish pseudo-strain calculations prior to the haversine wave fatigue test as discussed above. As portrayed in the data plots, Figure 4 and 5, the fine-tuned SHRP Shear machine easily and repeatedly achieved the required controlled-strain level. Also evident in these figures is the spread of data points that accurately define sample response. Data "snapshots" were acquired in groups of three cycles at the rate of 160 cycles per second. Figures 4 and 5 attest to the success of this data sampling rate in defining the hysteresis loop experienced by the sample in the course of the test. It should be noted that the specimens AAD #1 and AAM # 1 were subjected to continuous loading without rest periods. Data were

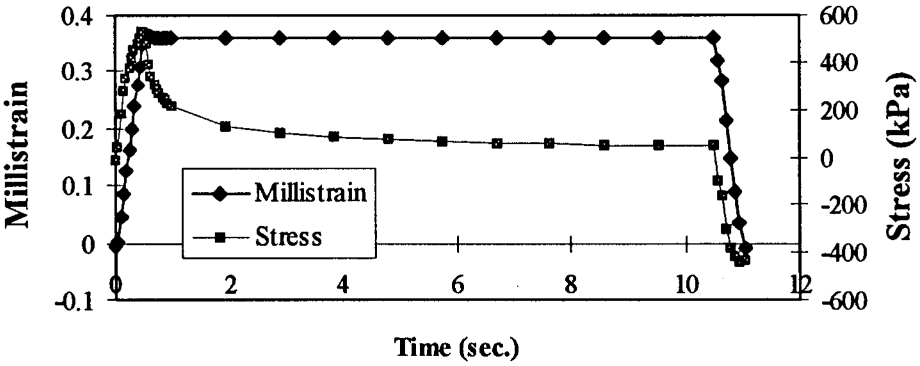

Figure 6. Commanded Trapezoidal Waveform Introduced to Haversine Wave Test to Facilitate Use of the Microdamage Model.

sampled within the first, middle, and last five loading cycles of each group, so a 100-cycle group would be sampled within cycles 1-5, 48-52, and 95-100. Tests could last as long as 100 loading groups corresponding to 98 rest periods. To study the effects of healing, one must collect data occurring before and after the selected healing period to be analyzed. To keep data file size at a manageable level, two loading periods were sampled per rest period (before and after).

The tests were performed at 25 °C in four sequences: no rest periods, and rest periods applied every 100, 200, or 300 cycles. The rest period length was standardized at 2-minutes, and this remained constant throughout each test. However, extensive testing in phase I of this research clearly showed that, as rest period length increases, healing increases, Figure 7. A test was judged to be complete when the observed load peak dropped to 50 percent of that peak load recorded during the first load cycle. Upon test completion, the sample was removed from the endcaps, and the data were copied to a floppy disk, including a backup diskette, and analyzed using the Microsoft Excel spreadsheet.

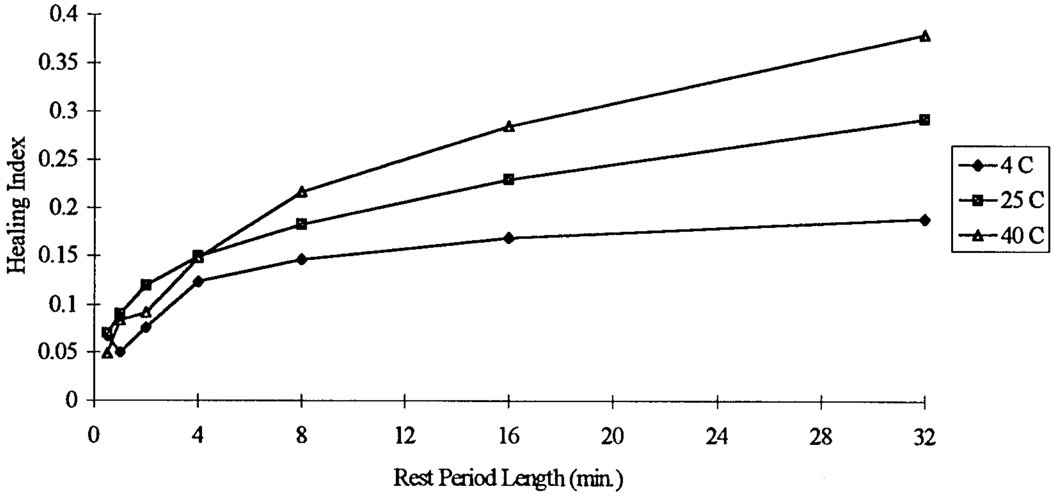

Figure 7. Effect of Rest Period Length on Magnitude of Healing as Quantified by the Healing Index (Samples Were Prepared with Bitumen AAM).

Data Analysis

The fatigue test data were analyzed to evaluate healing rate during each of the rest periods prior to sample failure. In order to remove the confounding effects of time-dependent viscoelastic behavior, a linear transformation of the data from engineering stress and strain to pseudo stress and strain was performed prior to analyzing the healing behavior. A discussion of potentially confounding factors is presented later.

Identification and Calculation of the Healing Index

The healing index is a measure of the regained strength of asphalt materials after rest periods. The data in this project were analyzed directly to calculate the healing index. Direct analysis means that the healing index is computed based on dissipated energy. A second and more complete way to measure microdamage healing is when the time-dependent effects of asphalt response are removed by the calculation of dissipated energy using pseudo strain. The value of healing index calculated using pseudo energy is considerably greater than the value computed using total dissipated energy since time-dependent (recoverable) energy is accounted for in the denominator of the healing index when pseudo energy is used in the calculation. The healing index is related to the specimen dissipated energy by equation (1).

The healing index is simply a mathematical expression to quantify the increase in energy required in the test to induce an equal strain in a given specimen after a rest period compared with the energy required to accomplish the same task on the same sample just before the rest period. The dissipated energies, represented by ϕ_d and ϕ_h , are numerically determined by calculating the area beneath the first quadrant of the stress-stain plot, which represents the specimen response in tension.

The areas beneath stress-strain curves were calculated using the Microsoft Excel spreadsheet. The imported ASCII file contained the required data to calculate stress and strain during the entire test. Once the appropriate load cycles were identified, i.e., those just before and after applied rest periods, the stress and strain columns were used to construct a graph for visual comparison. Then, a point-by-point application of the trapezoid rule was used to calculate a close approximation of the area beneath the curve between all the points on the graph occurring in the first quadrant, meaning those with positive values of stress and strain. The equation approximating the area beneath the curve between two points, X_1 ($\sigma1,\epsilon1$) and X_2 ($\sigma2$, $\epsilon2$), is:

$$\int_{x_1}^{x^2} \frac{\sigma \; d \, \epsilon \; (\sigma_1 \, + \, \sigma_2)}{2} \; x \; (\epsilon_2 \;\; \epsilon_1) \qquad (4)$$

The areas were calculated between all first quadrant points for each curve (damaged and healed) and then summed. This sum total is the respective dissipated energy:

$$\sum_{k=1}^{n} \int_{x_1}^{x_2} \sigma \, d \, \epsilon \; \frac{(\sigma_1 \; + \; \sigma_2)}{2} \; x \; (\epsilon_2 \; \epsilon_1) \tag{5}$$

The resulting dissipated energy values were input in the healing index equation and compared as a function of the rest period length and number of rest periods.

Transformation of Stress/Strain Into Pseudo Stress/Pseudo Strain

Viscoelastic materials characteristically relax under cyclic loading. The degree of relaxation or creep is dependent upon the time average strain is applied to the sample under the test conditions. If sinusoidal loading is centered about a zero-strain axis and thereby induces an average strain, then relaxation effects are minimized. Haversine tensile waves cannot be centered about a zero-strain axis like a tensile-compressive sinusoidal wave, so load declination due to relaxation must be expected. The healing index compares a load-dependent quantity, dissipated energy, by relating two key values of dissipated energy sampled about rest periods. The first, occurring at the end of a load regime, may decrease in part due to the relaxation of the specimen during the preceding loading regime. This decrease could inflate the value of the healing index, which should be used to characterize only damage in the sample, not damage and relaxation. Since the sample is held at zero strain during a rest period, the first loading following a rest period would be applied from a datum of zero strain, and therefore would not be subject to the same confounding influence of relaxation. An additional benefit in considering relaxation behavior is to explain the small compressive loads required to return the specimen to zero strain at the beginning of the rest period. During the loading regime the specimen relaxes toward a datum of the time average strain. The return to zero microstrain will therefore require a load, which, as the datum for the material returns to zero, will diminish with time as determined by the specimen's relaxation modulus. If the relaxation is not complete or very nearly so, the peak load and dissipated energy of the ensuing cycle would be inflated, also inflating the healing index.

The haversine strain wave test used in this experiment applied a strain pulse of 330 microstrain amplitude to the specimen, as shown in Figure 8. The time average of such a wave is about 52 microstrain. This means the wave could be linearly modeled by the Boltzmann superposition principle as a haversine wave with a time average of zero plus a constant applied 52 microstrain, as appears in Figure 9.

As the strain wave form must be adjusted for the effects of relaxation, so must be the measured response. The relaxation modulus can be determined based on the trapezoidal wave form preceding each fatigue test. The trapezoidal waveform produces a tensile and compressive plateau, from which pure power law compliances are regressed. This wave is plotted in Figure 10.

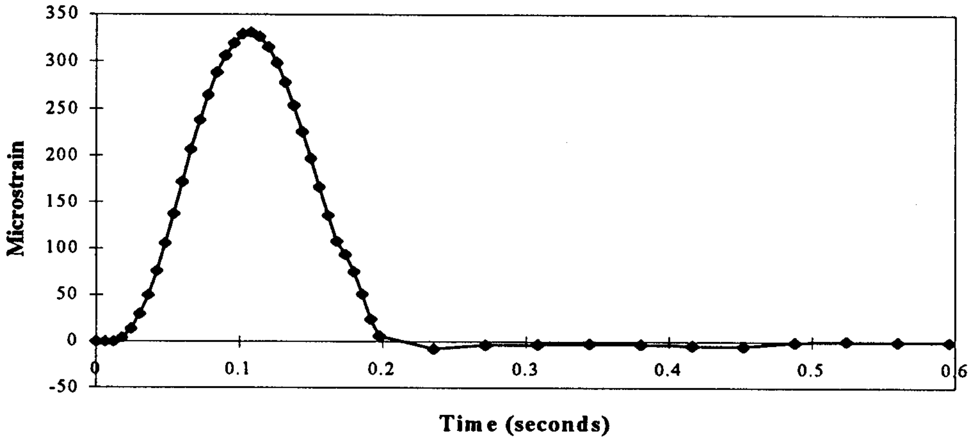

Figure 8. Typical Applied Strain Wave Collected From Haversine Wave Strain-Controlled Fatigue Test on Sample AAM #41.

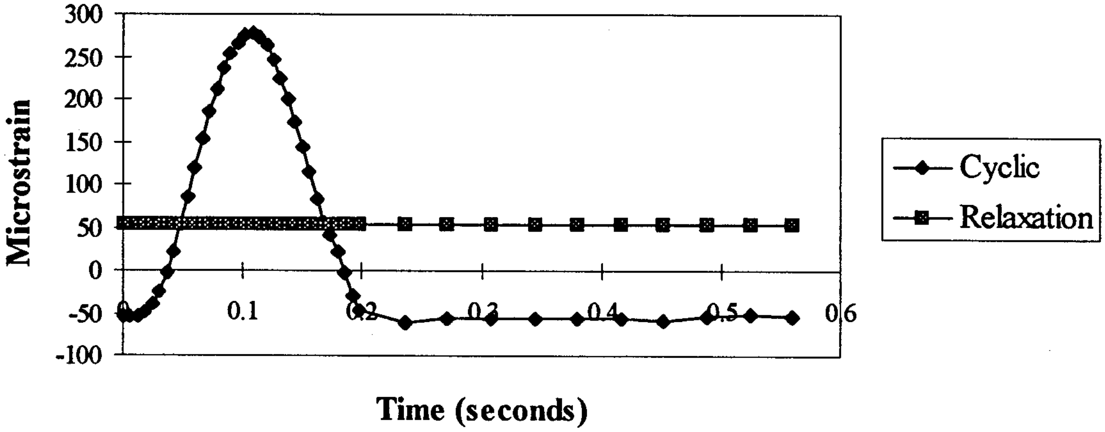

Figure 9. Linear Viscoelastic Model of the Applied Haversine Strain Wave.

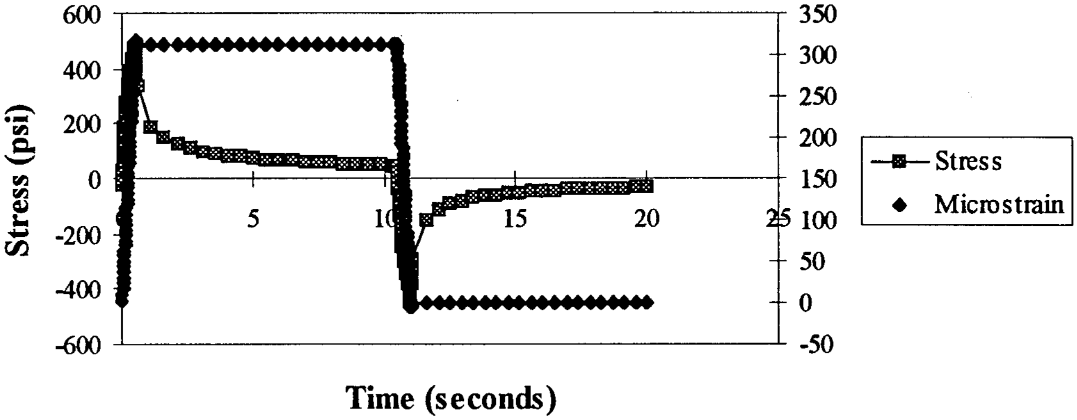

Figure 10. Trapezoidal Wave Applied to Specimen AAM #41 Used to Develop Pure Power Law From Relaxation Properties.

The pure power law relationship is then multiplied by the time average applied strain, predicting the stresses to be developed on the individual sample in question at the average applied strain calculated for that particular test. This calculated relationship appears in Figure 11 plotted against the actual measured response for sample AAM #41. Note the maximum initial stress of 1000 kPa; this was substituted for the asymptotic value normally estimated at zero time for the sake of completing the graph. The stress transformation is completed by subtracting the predicted compliance stress from the actual measured response at each point in time. The resulting transformed stress and strain are plotted against each other in Figure 12.

Creep rate properties are insensitive to damage; the phase angle (and therefore creep compliance slope) are constant for a given material with damage. Upon determination of the stress transform to be expected from relaxation at the average strain during the loading period, the healing indices are adjusted. It should be noted that the trapezoidal data exist for each individual sample, and can provide sample-specific shifts. An example of the substantial shift in the measured healing with the pseudo-energy transform is displayed for sample AAM 41 in Figures 13 and 14. The substantial effect on the measured healing index is illustrated in Figure 15. This may help circumvent some of the issues of sample rheological variability, which can be considerable.

There is no doubt that converting the measured response to pseudo-strain eliminates these time-dependent effects; that is the theoretical basis for the use of pseudo-strain transformations. Unfortunately, the difficulty in fitting a more sophisticated incremental strain function to a haversine-shaped wave is very great, and it appears it would take years to perform this nonlinear analysis on the data reported here.

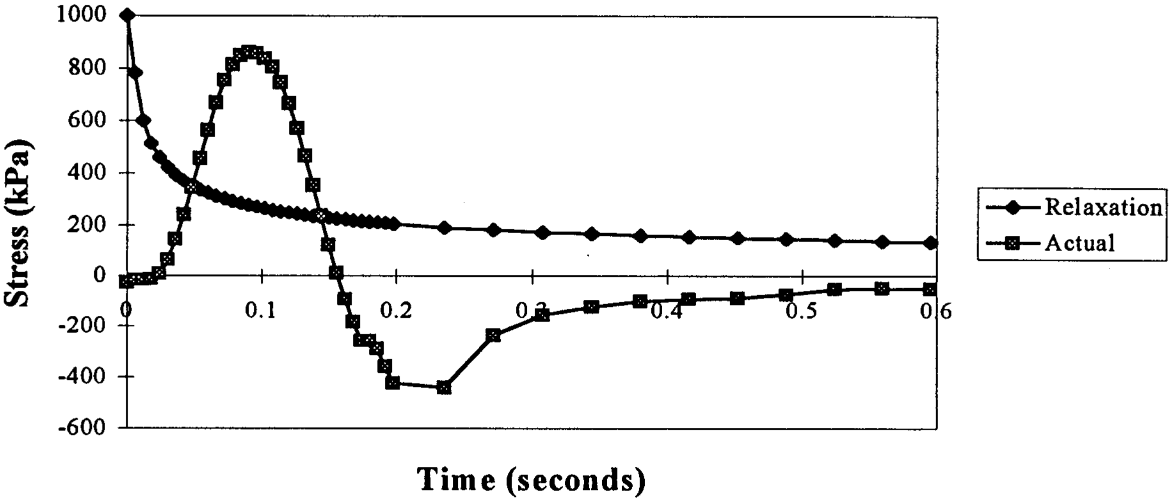

Figure 11. Comparison of Pure-Power Law Modeled Relaxation Stresses With the Actual Recorded Stresses From One Loading Cycle of the Fatigue Test Performed on AAM #41.

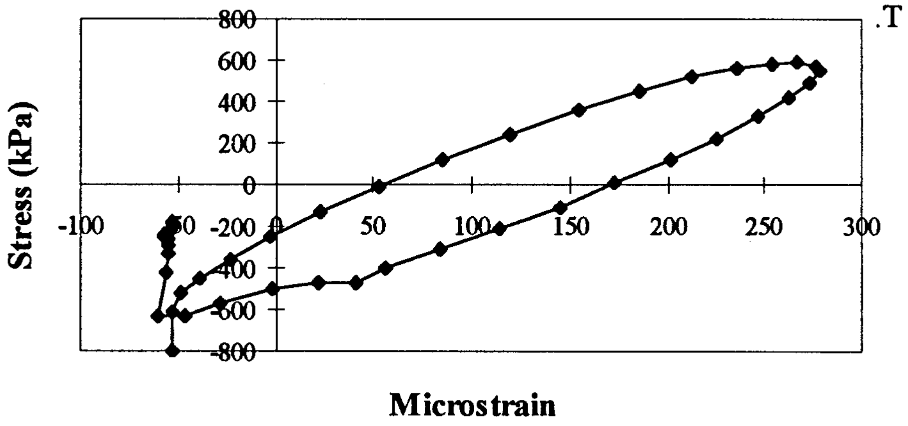

Figure 12. Transformed Stress and Strain Values for the First Haversine Wave Load Cycle Applied to Sample AAM #41.

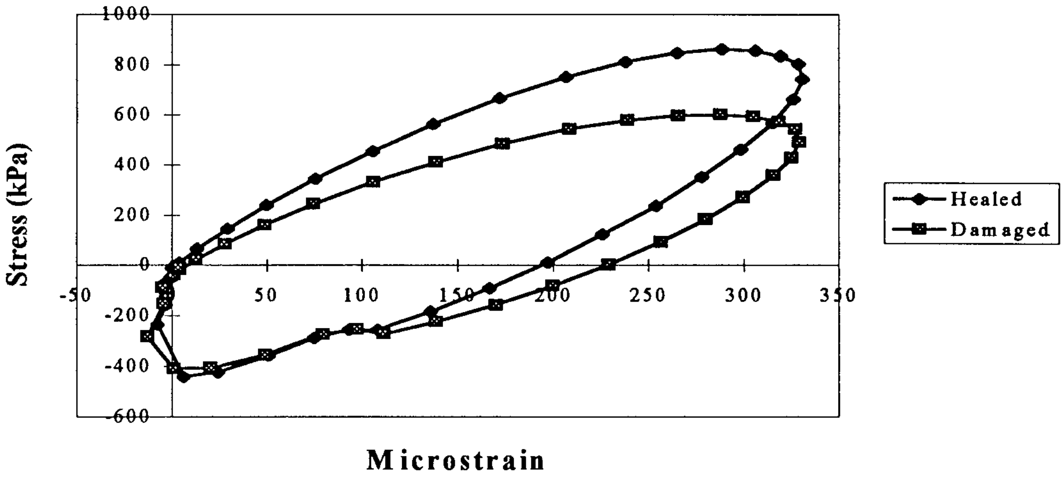

Figure 13. Data About the First Rest Period Collected During the Fatigue Test Presented in Engineering Stress and Strain.

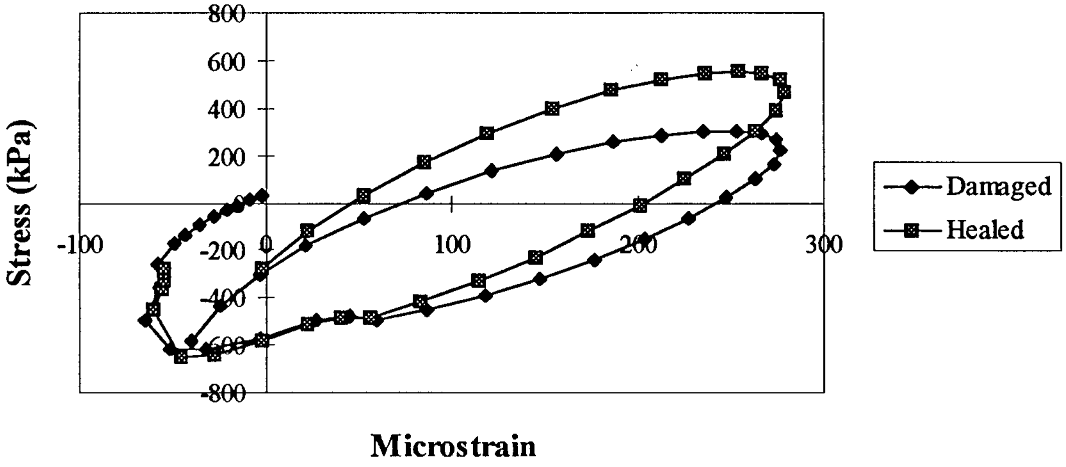

Figure 14. Data About the First Rest Period Collected During the Fatigue Test Presented in Transformed Energy Values.

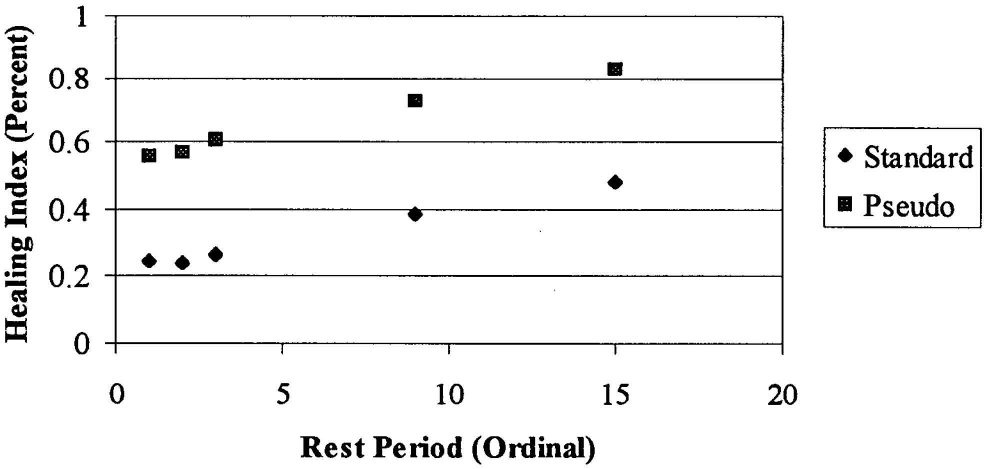

Figure 15. Healing Index Values Throughout the Fatigue Test Calculated With Standard and Transformed Energy Values.

RESULTS

General Experiment

As previously discussed (p.12), the general experiment sought to evaluate the sensitivity of microdamage healing to mixture component factors that should logically influence microdamage healing. Experiments designed to evaluate the influence of aggregate type on healing were inconclusive. Healing indices calculated for mixes fabricated with a limestone aggregate were not significantly different from those fabricated with a granite aggregate. Similarly, the effect of the type of mixture (stone mastic versus dense-graded) was not clearly established as the aggregate type did not have a statistically significant influence on the healing index in the experiment. The authors had felt that a mix that is more conducive to a high mastic content (stone mastic) would encourage cohesive fracture and hence would favor healing over a dense-graded mix where a higher percentage of adhesive fractures should occur. This could not be verified.

The following conclusive trends could be established from the general experiment. These trends will be discussed in the section below entitled "Discussion or Results."

1. Modifiers added to unaged asphalt, including low density polyethylene and styrene butadiene copolymer, reduced the healing potential as quantified by the healing index when compared with the virgin or unaged binder. The effect of hydrated lime was binder specific, demonstrating an improved healing index for bitumen AAD but no significant effect on bitumen AAM.

2. The addition of hydrated lime substantially increased the healing index of aged binder

systems regardless of the bitumen evaluated.

3. The effect of hydrated lime on the healing index is bitumen specific and is in direct agreement with the results of dynamic shear rheometric analysis of similar binder systems.

More extensive experiments are required to clearly establish the effects of aggregate-bitumen interaction and bitumen modification on fracture healing.

Primary Experiment

A major objective of the Task K research program was to identify the asphalt constituents that influence microdamage and microdamage healing. A very large and unwieldy experiment can ensue for this demanding goal. The most meaningful assessment of the effect of material components on mixture fracture healing was determined by applying the fundamental laws of fracture. From this approach based on first principles, it was shown that a mixture's susceptibility to fracture and amenability to healing is strongly rooted in the surface energy properties of the bitumen (cohesive fracture/healing) and the aggregate (affecting the adhesive properties fracture/healing). Although other mixture constituent and component features doubtlessly affect fracture and healing, the most meaningful experimental results from this study surrounded and regarded the surface energy properties of the binders. As discussed in the research approach, five very different binders were selected for the precise reason of their difference and diversity as a means to assess the effect of binder composition and binder surface energy on fracture and healing.

Figures 16 and 17 depict example plots from mixtures fabricated with bitumens AAD and AAM tested in the strain-control, haversine wave-based test. Each diagram represents data about a rest period germane to the calculation of the healing index as discussed above: the last strain pulse prior to the rest period and the corresponding pulse ensuing the rest period. All rest periods were standardized at 2-minutes in these tests to remove the confounding variable of rest period length. Data were recorded periodically throughout the tests around specified rest periods as they occurred in the course of the test (1, 3, 9, 15, 25, 35, 45, 55, 65, and 75 or until failure).

Figure 18 represents the data culled from the virgin binders used in dense-graded asphalt mixes. Each point represents an average healing index calculated for all the samples for that binder with Watsonville Granite aggregate, independent of whether the rest periods occurred every 100, 200, or 300 cycles. The data were grouped in this manner because the spacing of the rest (number of cycles between rest periods) periods seemed to have no effect on the magnitude of the healing index. It is interesting to note however, that in the phase 1 study, when rest periods are separated by more than about 500 rest periods, the effect of the rest period on the healing index was substantially reduced. The binder-specific healing indices in this figure suggest two characteristics of healing index behavior: a minimum or specific level of healing for a given duration of rest period (i.e., 2-minutes) and, for select binders, a tendency for the ability to heal to increase as the test progresses. If the curves present in Figure 18 are regressed as a natural logarithmic function, the following relationships result: (HI= healing index)

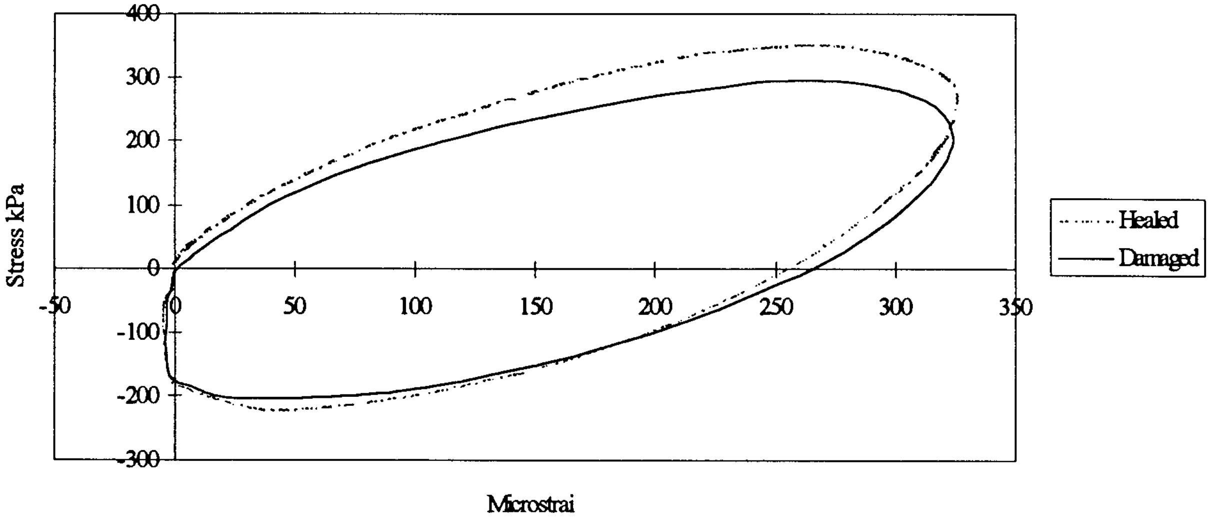

Figure 16. Shift in Hysteresis Loops or Recovered PSE Density After a Rest Period for Sample AAD #1.

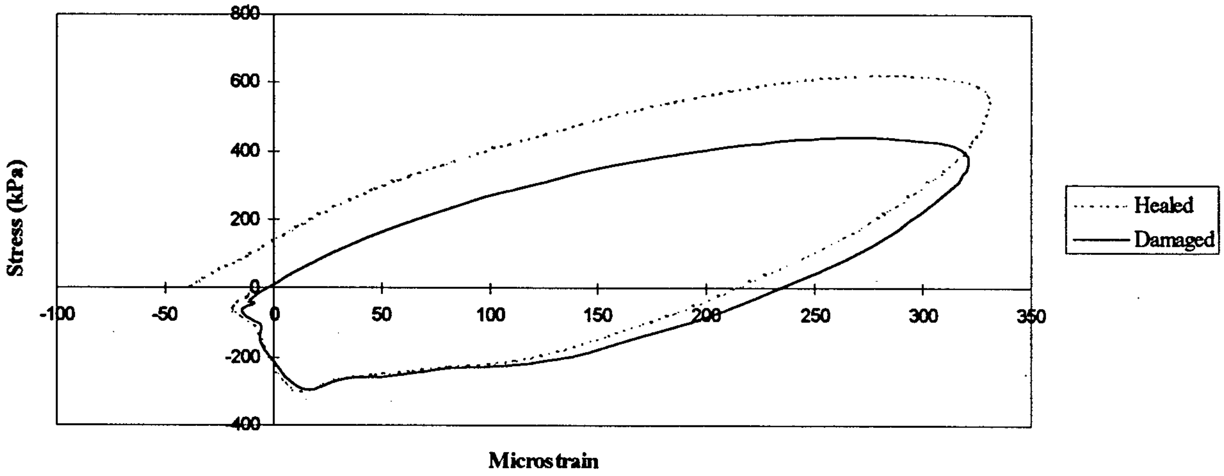

Figure 17. Shift in Hysteresis Loops or Recovered PSE Density After a Rest Period for Sample AAM #1.

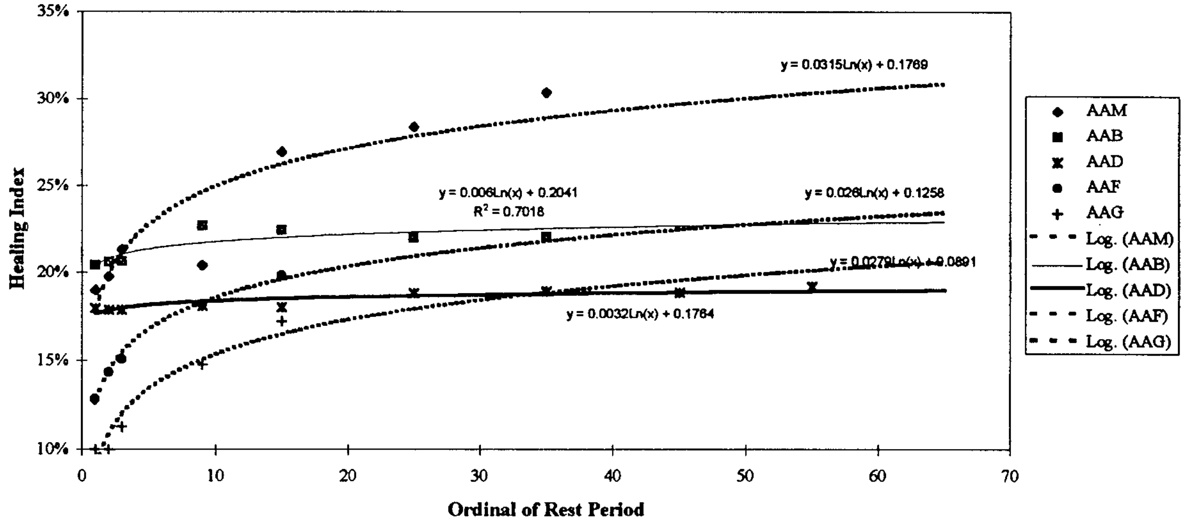

Figure 18. Relationship Between Healing Index and Number of Ordinal Rest Periods for Five Bitumens.

$$\mathrm{HI(AAB)} = 0.2236\ \ln(\text{rest period})^{.014}$$
$$\mathrm{HI(AAD)} = 0.1905\ \ln(\text{rest period})^{-.003}$$
$$\mathrm{HI(AAF)} = 0.1448\ \ln(\text{rest period})^{.031}$$
$$\mathrm{HI(AAG)} = 0.1164\ \ln(\text{rest period})^{.069}$$
$$\mathrm{HI(AAM)} = 0.2267\ \ln(\text{rest period})^{.058}$$

Notably, mixtures prepared with AAM-1, AAG-1, and AAF-1 exhibit a comparatively substantial growth in their healing indices as the test continued (as demonstrated by the magnitude of the exponent of the rest period gradual number), whereas the AAD-1 and AAB-1 mixtures did not. Additionally, the AAM-1 and AAB-1 mixtures exhibited a higher initial or minimum value of healing.

It is apparent from the above relationships that some mixtures exhibit a growth in their healing performance as the test propagates (AAM, AAG, AAF) whereas two (AAB, AAD) demonstrated very little increase in healing level as damage occurred. These trends led to the suggestion of a two-slope nonlinear model, a general representation of which appears in Figure 19. The independent variable is the time at rest, which is developed from the sum total of all rest periods occurring in the test to a given point times the rest period length of 2-minutes. The dependent variable is the measured healing index. The resulting slopes, $\dot{h}_1$ and $\dot{h}_2$, are developed from a transformed linear model in the equation below:

$$\dot{h} = \dot{h}_2 + \frac{\dot{h}_1 - \dot{h}_2}{1 + \frac{\dot{h}_1 - \dot{h}_2}{h_\beta}(\Delta t)_h} \tag{6}$$

where $\dot{h}$ = the actual healing rate;

$\dot{h}_1$ = early healing rate generated by surface energy properties rapidly realized;

$\dot{h}_2$ = long-term healing rate, generally related to the acid-base surface energy component;

$(\Delta t)_h$ = the rest period between load applications; and

h_β = a factor that varies between 0 and 1 and represents the maximum degree of healing achievable.

The pertinent values for the slopes and fit constants appear in Table 7.

Table 7. Constituents $\dot{h}_1$, $\dot{h}_2$ and Spacing Factor h_β Used to Fit Healing Index to Total Accumulated Rest Period Time Using Nonlinear Model.

Parameter	**Bitumen**				
	AAB-1	**AAD-1**	**AAF-1**	**AAG-1**	**AAM-1**
$\dot{h}_1$	0.02	0.00	0.15	0.12	0.34
$\dot{h}_2$	0.27	0.17	0.32	0.46	0.42
h_β	0.04	0.03	0.17	0.05	0.02

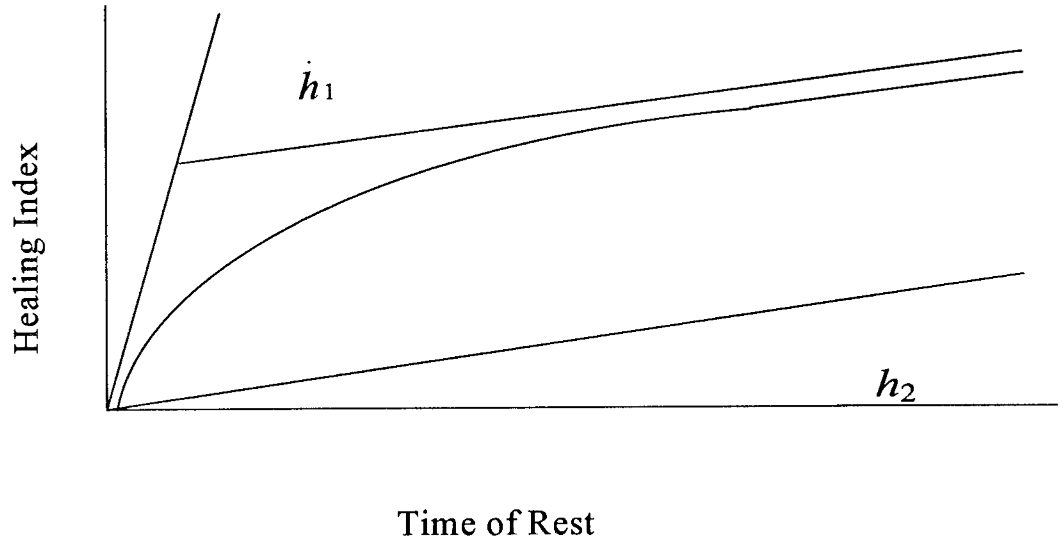

Figure 19. General Form of the Model Used to Fit Healing Index Data to the Total Amount of Rest Period Time in Asphalt Concrete Specimens as Observed During Fatigue Tests.

Discussion Of Results

The stated goal in Task K research is to determine the nature of what is termed 'healing' in asphalt specimens under fatigue loading. This section deals only with laboratory testing toward this end. Healing as measured in the laboratory is characterized by a recovery of structural stiffness in a damaged sample. A stiffness reduction can occur due to the development of microcracks, and recovery can be due to microdamage (including microcrack) healing or other effects (discussed in subsequent sections of this volume). The researchers are confident that a large part of the recovered stiffness is due to microdamage healing. Fatigue tests on asphalt samples are deemed to have "failed" when a terminal stress or strain value, translating directly to a terminal stiffness is reached. The healing index is a simple measurement of the stiffness recovered by asphalt samples during a rest period within a fatigue test. The healing index is not a fundamental property of materials like compliance and relaxation moduli, nor is it directly associated with mixture fabrication or volumetrics such as air voids are. It is simply intended to provide a picture of the change in the sample state through an understandable concept, the concept of stiffness.

Since the healing index is not a fundamental property, its values have rightly been questioned as being tainted by the numerous mechanisms of strengthening and softening germane to asphaltic and other viscoelastic materials. These factors include, but are not limited to, molecular structuring or steric hardening, hysteresis heating (or damping), and stress relaxation. Steric hardening has been advanced as a possible explanation for the modulus increase in asphalt specimens at rest, as it has been observed on essentially unused roads. Hysteresis heating is the conversion of viscoelastic damping energy into thermal energy, and it is thought that the temperature increase in the samples that may occur during loading may subside during rest periods in the tests, and thus (at least partially) account for the increased modulus apparent after the rest period. These issues will be dealt with in the ensuing paragraphs.

Finally, the healing index is also thought to be related to either the ability of the material to flow back together, or the closure of cracks from energy available in the system. The healing index was evaluated against the surface energy of the asphalt binders to determine whether the concept of surface closure is reasonable. The surface energies represent a gross surface effect. The surface energy concept and the methodology for measuring surface energies of the binders and the aggregates were discussed previously.

Effect of Steric Hardening (Molecular Structuring)

Steric hardening or molecular structuring produces a reversible phenomenon that can produce large changes in the flow properties of asphalt without altering the chemical composition of the asphalt molecules. Petersen (1984) indicates that it is a slow process that may go on for days or even years, and it can be promoted by mineral aggregate surfaces. Petersen (1984) discussed the hardening rates on selected asphalts as a function of asphalt source and found the rate and degree of steric hardening to be source dependent, with air blown asphalts showing a greater rate of structural hardening. According to the data presented by Petersen (1984), the time period required to realize significant levels of molecular structuring at 25 C is between about 10 and 1000 hours depending on the source. Molecular structuring that can be influenced by the aggregate mineral surface may occur at more rapid rates in mixtures, and it is apparent that the effect of molecular structuring is synergistic with oxidative aging. However, the researchers do not believe that molecular structuring in and of itself is sufficient to account for a significant proportion of the recovery in dissipated or pseudo-dissipated energy measured in these experiments at temperatures of between 20 and 25 C and at rest periods of only 2-minutes.

Effect of The Temperature Confoundment

The mechanical response of asphalt mixtures, like other viscoelastic materials, is very sensitive to temperature. A few degrees (Celsius) temperature change can shift modulus by a significant percentage. Additionally, viscoelastic materials dissipate the mechanical energy applied to them in part through heat. This heat is generated by what is mechanically termed damping, commonly known as hysteresis heating.

The maximum energy a specimen can store during any given cycle is developed throughout the period in which the stress is increasing, up to and including the maximum. For sinusoidal loading, this is the upload period, or the first quarter, of a sin period of 2π. The maximum energy available to be stored, W, can be calculated by integrating the increment of work through the period of time required to upload, T/4, where T is the sinusoidal period length:

$$W = \int_{0}^{T/4} \sigma \frac{d\epsilon}{dt} =dt \tag{7}$$

Substituting for the sinusoidal condition nets:

$$W = \int_{0}^{T/4} \sigma_0 \epsilon_0 \omega \sin \omega t \cos \omega t \, dt \tag{8}$$

and integrates to:

$$W = \sigma_0 \epsilon_0 / 2. \tag{9}$$

Note that the solution includes a stress term and a strain term. This maximum input energy is a theoretical maximum (and conservative) because the calculation of the maximum depends on the stress and strain waves being in phase. The energy lost to damping can be calculated by substituting a strain function with a lag angle into equation 8:

$$\Delta W = \int_{0}^{T} \epsilon_0 \sigma_0 \omega \sin \omega t \cos (\omega t - \delta) dt \tag{10}$$

which, when integrated, yields:

$$\Delta W = \pi \sigma_0 \epsilon_0 \sin \delta \tag{11}$$

This is the energy density lost per cycle to damping, which is considered to be converted entirely into heat. Since the fatigue tests performed at Texas Transportation Institute are strain-controlled, the heat evolution is dependent on the lag angle of the mix and the stiffness of the specimen, as evidenced by the sin δ and stress terms. This implies that stiffer samples develop heat in the damage zones at a greater rate than the less stiff samples and therefore the contributions of heat evolution to the drop in stiffness or peak load in a strain-controlled test are mixture -specific. In specimen groups featuring the same aggregate, the damping should be binder specific.

This heat evolution can be translated into an estimated total heat gain by multiplying the energy density calculated (equation 11) by a mixture-specific heat and the volume of the specimens. The heat evolution in asphalt mixes was measured by Di Bennedetto et al. (1990) with internal thermometers. A maximum gain was noted after roughly 75,000 cycles of about 1.2 C on beam samples subjected to a cyclic loading of 10 Hz before an apparent steady-state condition was reached. It was also observed that the specimen required at least 1000 seconds to lose half the heat developed during loading. This is understandable assuming the test environment and specimen are at the same temperature at the beginning of the test, and the environmental temperature is kept constant during the test period. As heat transfer is gradient driven, and the gradient between the air and the sample was never greater than 1.2 degrees, a slow rate of heat transfer would be expected. This means rest periods substantially longer than 1000 seconds would be required for the specimen to again reach ambient temperature. The specimen modulus would change with temperature, also, but long rest periods would also be required for this to occur.

The tests performed in the general and primary experiment consisted of haversine strain waves applied in groups of 200 cycles, which, based on Di Bennedetto's data (1984), would not lead to an appreciable sample-wide or global temperature gain. Furthermore, the rest periods applied were 2-minutes long, which implies that the stiffening accounted for in the healing indices measured about these rest periods is not the result of a long cooling time. With little potential change in global temperature during this type of rest period, it would appear such a change could not be the source of the measured stiffening during short rest periods.

However, if appreciable temperature rise were measured during the loading regimes, the temperature recovery could have an effect on the recovery of specimen stiffness. Two samples, AAG-23 and AAG-21, were fitted with an external thermometer in order to gauge whether global specimen heating occurred in the haversine strain wave fatigue test. An increase of 0.1 degrees centigrade was noted on AAG-23, and none was detected in AAG-21. Di Bennedetto (1984) had samples fitted with an internal thermometer. This was not done at TTI in order to maintain sample integrity for damage modeling. Additionally, since the recovery of stiffness due to temperature loss depends on a gradient between the sample and the surroundings, the external surface temperature of the specimen is key in estimating the degree of heat loss by providing the driving gradient.

Another temperature evolution-related concern is the localization of damage. If the deformation within the sample is assumed to be the result of the well-dispersed microcracks, and the deformation is favored to occur at the weakest point in the mixture, then nearly all the damping would occur in these same regions. If these regions are a small enough portion of the specimen volume, considerable increases in local temperature could result, forcing a substantial change in properties. The viability of this scenario depends on the heat conductivity of the asphalt; if the asphalt conducts heat poorly enough, the heat resulting from damping will remain in the local vicinity of the cracktip, radically affecting both crack propagation and healing. If the asphalt conducts heat well enough, then the heat is dispersed throughout the binder, resulting in what has been measured as insignificant on such a global basis. Also of great importance would be the heat transfer across the boundary of the asphalt and the aggregate, as well as the specific heat of that aggregate. If the heat transfer to the aggregate is significant and the aggregate has a much higher specific heat than the asphalt, or even a specific heat equal to the asphalt (considering the weight proportion in the mix), the aggregate would behave as a heat sink, negating significant temperature change. It is likely that the asphalt and aggregate are both heated. This also accounts for the length of the cooling process where thermal energy is dissipated.

In summary, asphalt samples must undergo a very large number of fatigue cycles to develop significant temperature changes that affect modulus. This is likely due to the need of the asphalt, which is exhibiting most of the damping behavior in tensile tests, to heat the aggregate, which comprises over 94% of these mixtures (by mass) evaluated in this study. Once heated, mixes cool at a very low rate, which must decrease with cooling as the thermal gradient between the specimen and the surroundings diminishes. It is unlikely that global heating has an effect on specimens, which are tested for 200 cycles per loading period, during which little temperature change could evolve, and then rested for 2 minutes, during which little heat would be lost to the surroundings.

Localized crack tip heating should be investigated further. Localized heating would indicate a potential for greater molecular mobility and activity at a crack tip, as well as change the chemical environment in which asphalt surface interactions occur in the vicinity of cracks with respect to molecular motion and interaction.

Effect of Specimen Stiffness

Specimen stiffness, in a strain-controlled test such as this, exerts a powerful effect on both the rate of material declination and the potential for temperature evolution. Obviously, since only the applied strain can be controlled, stiffer mixtures undergo much more rigorous testing in terms of the energy applied to them in a given number of cycles. This energy will be dissipated in a number of ways in asphalt specimens but chiefly through cracking damage and damping.

Damping, as discussed previously, is dependent directly on the stress amplitude. Since the strain amplitude is controlled in the haversine wave test, the damping is directly proportional to the material stiffness at the time of the loading. Thus the damping will decline with successive loading applications dependent on the rate of damage, the amount of relaxation between load cycles, and the stiffness. The degree of the effect stiffness exerts on damping (and therefore the potential for temperature evolution) can only be assessed after the relaxation behavior is removed from the scenario, so as to isolate the effects.

Stiffness exerts a great influence on the damage developed in the sample in strain-controlled tests of any kind. In the absence of relaxation, it directly relates the dissipated energy to the applied strain. Since relaxation behavior is present in asphalt mixes and independent of damage, the relaxation effects must be removed from the data before assessing the rate of damage applied to the material with the highest level of accuracy.

Effect of Plastic Deformation

The healing index is a measure of the recovery of the ability of the asphalt concrete solid to dissipate energy. However, it is possible that energy lost to plastic flow can obfuscate the effect of healing on the fatigue life.

Plastic flow without cracking can cause deformation in the solid but not necessarily a significant loss of stiffness, a parameter on which the healing index greatly depends. This behavior is similar to that observed in polymers and metals. While plastic dissipation is not necessarily noticed in a measure of stiffness in cyclic loading, it is most certainly a critical form of damage. Since the degree of plastic damage may not be directly detected using the healing index, it must be isolated in the discussion of fatigue life recovery via microcrack healing.

A finite-element model (FEM) was developed to predict damage exclusively through microcrack growth in the asphalt concrete sample tested in this study by Lytton and Chen (Lytton et al. (1998)). This model was fit with precision to data actually acquired from test specimens at 4°C and 25°C. The model incorporates the independent variable of surface energy. The FEM cracking model accurately predicted the rate of change in dissipated energy at 4° and 25°C, but the cracking-only model did not explain damage at 40 C. This indicates the effect of cracking is overwhelmingly dominant in asphalt concretes at temperatures 25°C and below, but that the energy dissipation mechanism shifts significantly at some temperature between 25° and 40°C such that plastic deformation plays an important role. Furthermore, considering the tests discussed in this volume were performed at 21°C, plastic deformation is not considered an influential variable in the analysis of the measurement of the rate and magnitude of healing.

Effect of Surface Energy

The binder wetting cohesive surface energy as measured by the Wilhelmy Plate method (discussed earlier) is a prediction of the gross effect of two asphalt surfaces coming together to form a solid. The surface energy density, Γ, is a reflection of the amount of energy required to reform a material without the fracture surfaces, i.e., a continuous solid. Schapery (1988) and Lytton et al. (1998) have both expressed the surface energy density (SED) as an integral part of the healing behavior, just as it is accepted as a critical property in the characterization of fracture behavior. Schapery and Lytton differ only in their respective interpretation of the role of surface energy density in the energy balance about the healing region, as discussed in the section entitled "Research Approach." The measured surface energies are related here to the measured healing rates.

The surface energy consists of two components; a Lifshitz-Van der Waals component and a Lewis acid-base component. The Lifschitz-van der Waals component describes the energy available on the surface to be overcome due to London dispersion forces, Debye induction forces, and Keesom orientation forces, among others. Correspondingly, the Lewis acid-base component describes the energy required to overcome forces such as hydrogen bonding. The forces comprising the Acid-Base surface behavior are much slower acting than those involved with the Lifshitz-Van der Waals behavior. The two components are related to the whole in the following way (Elphingstone, 1997):

$$\Gamma = \Gamma^{LW} + \Gamma^{AB} \tag{12}$$

Furthermore, the positive (acid) and negative (basic) components produce the acid-base surface energy density component as follows:

$$\Gamma^{AB} = (\Gamma^{-} + \Gamma^{+})^{1/2} \tag{13}$$

These relationships among surface energy components lead one to consider:

1. the effect of each component on the rate of healing, and
2. the effect of each of the component on the total healing potential.

As discussed and developed in the section entitled "Research Approach," Schapery (1988) finds that healing rate is directly related to the magnitude of surface energy. This indicates that more healing will occur as the surface energy increases, all other factors being equal. Lytton et al. (1998) found the opposite, an inverse relationship between surface energy density and healing rate. These relationships are developed with the important caveat that $D_0 = 0$ in the mechanical analysis.

The five SHRP binders sampled in this study each have unique surface energy density characteristics as presented in Table 1. The acid-base and Liftshitz-van der Waals components of each binder are compared with the slope's fit to the data for each binder in the two-slope model discussed in the "Results" section. The slope $\dot{h}_1$ represents the short-term healing rate of the asphalt mixtures, whereas $\dot{h}_2$ represents the long-term healing rate. Figure 19 depicts the correlation between the Lifshitz-Van der Waals component of surface energy density and the short-term healing rate. It is an inverse relationship that states that greater Lifshitz-Van der Waals components reduce short-term healing in the mix with a given binder. This behavior is implied by Lytton's model.

The opposite trend is apparent in the analysis of the acid-base values and the long-term healing rates $\dot{h}_2$ in Figure 20. There is a direct relationship between the significance of the acid-base component and the long-term healing rate. This infers that greater long-term cohesive healing is promoted by a higher acid-base component in the asphalt binder.

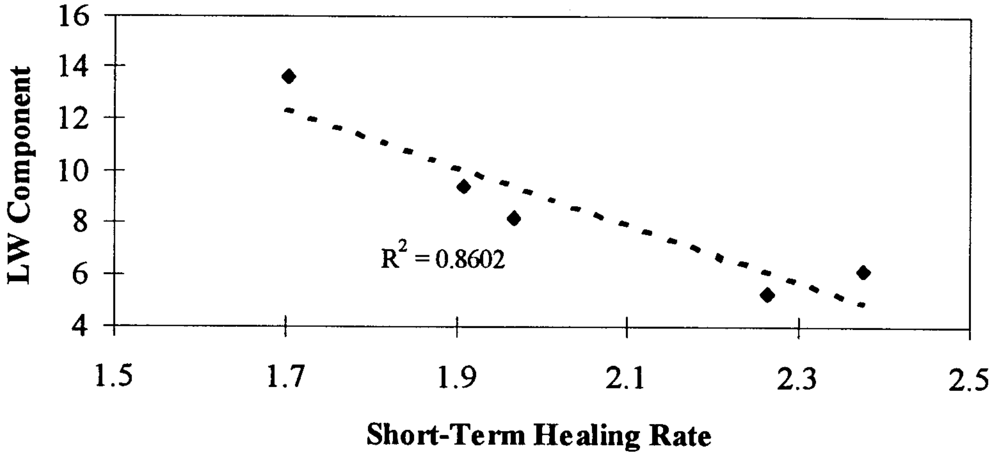

Figure 20. The Inverse Relationship Between the Magnitude of the Lifshitz-Van der Waals Component of Surface Energy Density and Healing Rate is Evident. Lifshitz-Van der Waals Behavior is Apparently Not Favorable to Healing.

These relationships are particularly exciting considering the assumptions inherent in each of the models. In the Lytton model, the energy available to reclaim a previously created surface is offset by the surface energy density of healing. This is an exact reversal of fracture theory, where the energy lost is deposited in the surface created by the fracture. In the case of healing under Lytton's theory, the surface is reclaimed in much the same process, presenting the surface energy density as a requirement that must be met by available energy. In light of the correspondence between Lytton's theory and the short-term healing rate slopes presented in Figure 19, the Lifshitz-Van der Waals component can be viewed as an immediate effect, one that requires energy to overcome the intermolecular interactions present on either face of the closing system. Local secondary forces such as these rapidly reach equilibrium, and this is evident in the spacing value (h_β) in the general model as well as the general shapes of the data fits. A large spacing factor implies a great difference between a line through the origin with a slope of $\dot{h}_2$ and the actual $\dot{h}_2$ line at the healing index plateau; however, low h_β values imply that short-term healing necessitates only a small shift in the data from the long-term $(\dot{h}_2)$ line.

Schapery's model assumes the energy present on the surface exerts a direct effect on the force balance driving healing, so there is a direct effect in his model between the magnitude of the surface energy and the healing rate. The correspondence between his modeled behavior and the observed increase in healing rate with acid-base component measurement implies that the acid-base component is a measure of an asphalt's ability to drive forth its own cohesive healing process. This is sensible considering the polar nature of the acid-base component, which can include secondary bonds much stronger and less likely to reach rapid equilibrium than those characterized by the Lifshitz-Van der Waals component. These forces can act over a much longer term than the weakest of secondary forces and can potentially form a more stable group of intermolecular interactions as well.

A final picture of the healing rate related to surface energy is simply two components at work simultaneously. The Lifshitz-Van der Waals and acid-base components have individual effects, and the sum of these concurrent properties is the healing behavior. The Lifshitz-Van der Waals component represents a local obstacle to the reformation of the cohesive asphalt solid region, while the acid-base component apparently contributes a driving, re-organizational force among the secondary bond network, which promotes healing. The Lifshitz-Van der Waals component rapidly reaches a para-equilibrium, and its corresponding effect remains stable, whereas the acid-base effect is longer term and drives forth healing for an indefinitely long period.

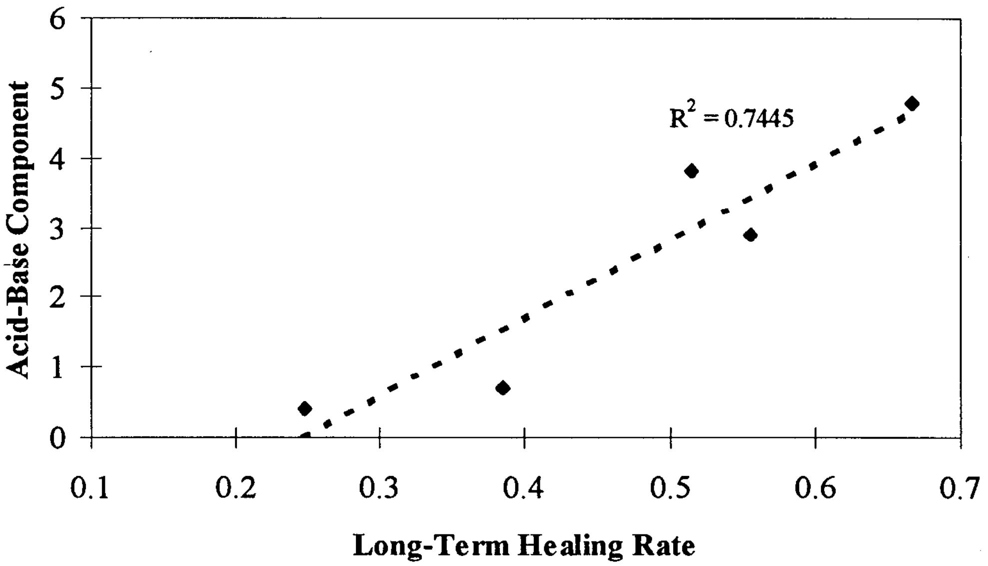

Figure 21. Comparison of the Healing Rates Observed in Asphalt Concretes With the Acid-Base Component of Surface Energy Density.

Chemical Composition

This experiment was designed to characterize the binder-specific healing behavior of asphalt mixtures based on chemical properties of five well-characterized asphalt binders. The SHRP Materials Reference Library contains numerous asphalt binders, which have been extensively characterized chemically and physically. The binders selected from this group, with the aid of Dr. Jan Branthaver of Western Research Institute, were AAB-1, AAD-1, AAF-1, AAG-1, and AAM-1. These binders differ in wax, amphoteric, and aromatic component contents as presented earlier in Table 1. The surface energy characteristics measured in a separate experiment by Elphingstone (1997) appear in Table 4. These surface energy data from a Wilhemly Plate experiment were compared with one another in the compositional matrices outlined in this experiment to determine whether measured asphalt composition could be related to measured asphalt surface energies. Such a link attempts to explain the relationship between observed healing behavior and chemical makeup of the neat asphalt binder.

Linear contrasts are frequently used to analyze differences across factorial experiments in the comparison of multiple factors. This technique is uniquely suited to the compositional analysis due to the placement of the five incorporated SHRP asphalts in two different experimental matrices. Differences in the surface energy data and its components can be analyzed across both matrices to pinpoint what chemical attributes appear to be most desirable for maximum healing behavior.

Based on this statistical analysis, the following linear contrast trials indicate a significant effect:

1. A low amphoteric content appears linked to a high acid-base component of surface energy (level of significance = 99.5%).

2. A high aromatic content is linked to a high acid-base component of surface energy (level of significance = 99.5%). The interaction of trials 1 and 2 is interesting. The relationship between a high aromatic content and a high acid-base surface energy is logical since the aromatic fraction is potentially a source of polarity in the form of pi-pi, multidirectional bonds and through polar appendages on the benzenic structure. While the amphoterics have polar ends, curiously they do not contribute to the measured acid-base surface energy from the Wilhelmy Plate experiments.

3. A high amphoteric content is linked to a high Lifshitz-Van der Waals component of surface energy (level of significance = 99.5%).

4. The combination of a high amphoteric content and low aromatic content suggests a low Lifshitz-Van der Waals component (level of significance = 99.5%).

Wax content did not have a significant predictive effect. Perhaps the nature of the wax is also important and can mask the simple effect of wax content. For example, the wax contained in

AAM is a microcrystalline wax and is present in far greater abundance in AAM than in any other bitumen evaluated.

This statistical analysis strongly implies that bitumen composition can be used to assess fracture and healing potential. However, more detailed and extensive experiments are required to identify and verify these relationships.

Effect of Miscellaneous Additives

Styrene butadiene (SB) copolymer was added to bitumens AAD, AAG, and AAM. The polymer additive significantly reduced the healing indices of bitumens AAD and AAG when compared with the unmodified versions. However, SB modification did not significantly change the healing index of mixtures with bitumen AAD. Low density polyethylene (LDPE) was added to bitumens AAD and AAM. The effect of LDPE was to significantly reduce the healing index of AAM and to improve the healing index of AAD. The effect of adding hydrated lime to AAD and AAM was very similar to the effect produced by adding LDPE to these same bitumens.

The negative effect of SB, LDPE, and HL modification on the healing index of binder AAM (and AAG for LDPE modification) was not expected. However, bitumen AAM is unique with a high percentage of "mobile" aromatics that apparently enhance healing. The addition of any additive seems to diminish the healing potential of AAM perhaps because it interrupts the polar mobility, which may be the reason for the excellent microcrack healing ability of AAM. Bitumen AAG is different from AAM, but it is also a dispersed system. On the other hand AAD is a highly associated bitumen in which the asphaltene fraction is highly interactive. It therefore is reasonable that the addition of any additive to AAM (and to a lesser extent AAG) may interrupt the "mobile" polarity of the system and diminish the healing capability. Part of this effect may be due to swelling of the polymer, which may result in an enriched matrix of asphaltenes, which may reduce mobility. On the other hand, polymer or HL modification of AAD has a positive effect. This may be due to an interactive effect between the additive surface and bitumen components that promotes healing. This can be visualized with HL as an interaction between the polar functionalities and the HL surface.

The effect of HL is perhaps the most interesting. The more reactive nature of HL with AAD than with AAM is verified in dynamic shear rheometer (DSR) testing where HL also demonstrates a more compatible and effective interaction with AAD than with AAM. In the unaged systems, the effect of HL on AAM is to actually depress the healing index (from 0.52 to 0.30). When AAM is aged, the ultimate or maximum value of healing index diminishes from approximately 0.51 to 0.31 due to the effects of aging. The effect of HL in the aged binder system is to slightly increase the ultimate healing index from about 0.31 for the aged control to about 0.33 for the aged HL - modified AAM. The effect of HL on the aged AAD bitumens is quite pronounced. The HL significantly improves the healing index from about 0.23 for the aged AAD to about 0.34 for the aged AAD with 12.5% HL.

Thus, HL appears to be a physico-chemically interactive additive that is bitumen specific in its effect on the rheological properties of the binder system and reduces the effects of aging and inhibits the ability of aging to diminish the healing potential of the bitumen. More study is needed in this fascinating area.

Table 8. Summary of Healing Indices for Mixture with Bitumens AAD and AAM.

Condition	**Bitumen**	
	AAD	**AAM**
Tank	0.23	0.52
Aged	0.23	0.31
Tank - 12.5% Lime	0.28	0.30
Tank - 20% Lime	0.30	----
Aged - 12.5% Lime	0.34	0.31
Aged - 20% Lime	----	----

Conclusions of Chapter 1

General Experiment

The general experiment was designed to evaluate the effects of mixture variables that might influence the type of fracture induced within the mixture and the rate of fracture and rate of healing within the mixture. From the general experiment, several conclusions were drawn, as presented in the following paragraphs.

1. Since SMA type mixtures are mastic-rich, it was hypothesized that this mix type might influence the mode of fracture and promote cohesive fracture instead of adhesive fracture. When the healing responses of SMA and dense-graded mixes (DGM) were compared, the mix type did not have an apparent effect on healing. However, when analyzed using the micromechanics approach, it was established that the cohesive mode of fracture was prevalent in not only the SMA but also the DGM.

2. The research team felt that polymer modification would enhance microdamage healing as reflected in the healing index. However, the effect was found to be highly bitumen dependent. Any modification of AAM was found to diminish its healing capability. Although this was surprising, it can be explained if the polymer absorbs certain bitumen components that result in an enrichment of the remaining bitumen phase (perhaps with

polar and interactive asphaltenes). This bitumen phase, enriched with polars and interactive molecules, may be less likely to flow and heal. In this sense the modified bitumen would behave similar to an aged bitumen. The LDPE does not normally interact significantly with bitumen through swelling. However, some swelling does occur and the LDPE bundles probably act as filler, which applies significant steric hindrance that may well resist healing. Apparently, AAM is an excellent healer because it is so rich in "mobile" polars. Any interruption of this characteristic is detrimental. On the other hand, modification of bitumen AAD (a very poor healer and a highly structured bitumen - immobile polars) always had some positive effect.

3. Hydrated lime can act as a filler in asphalt. It also has the ability to reduce the effects of oxidative aging. The effect of hydrated lime on the healing index when bitumen AAM was used was to diminish the healing index as the other additives did. However, the effect of adding hydrated lime to bitumen AAD was to enhance the healing index. This seems to be a logical trend if one considers that the effect of adding hydrated lime to AAM (a highly aromatic bitumen with a very low asphaltene content) may be to act as a filler or inclusion that may inhibit healing. On the other hand, the addition of hydrated lime to bitumen AAD (a highly associated bitumen and one with a high asphaltene fraction) may enhance the healing ability because the hydrated lime adsorbs or interacts with some of the more polar asphaltene fractions in the bitumen that may enhance flow and healing properties of AAD. Rheological tests show that hydrated lime is much more effective in altering the high temperature rheology of bitumen AAD when compared with bitumen AAM. Apparently, hydrated lime acts as a filler, which may have a coupling effect with AAD through physico-chemical surface interactions. These interactions may work to promote resistance to high temperature flow and also enhance healing.

4. Aged AAD and AAM systems both benefit significantly in terms of healing capability by the addition of hydrated lime. Apparently, the hydrated lime offers a mechanism for both bitumens (albeit better for AAD than for AAM) to interact with oxidation products so that the effects of these oxidation products does not inhibit the ability to flow and heal.

Primary Experiment

5. The rate of fracture and the rate of healing have been described by Schapery (1989) from the first principles of fracture theory. The fundamental explanation relates asphalt component and mixture properties to fracture (i.e., surface energy of the bitumen and aggregate and mixture compliance). Lytton et al. (1998) offered an alternative interpretation of healing based on Schapery's fracture explanation. Both Schapery's and Lytton's explanations of healing are based on first principles and relate fracture healing to surface energy of the bitumen and the aggregate and the compliance of the mixture. The primary experiment established the importance of surface energy of the bitumen to healing potential. A unified model of healing, which marries Schapery's and Lytton's models, was successfully used to explain how two components of surface energy (Lifschitz-Van der Waals and acid-base) relate to healing.

6. Bitumens with high acid base surface energy components are better long-term healers than those with low acid base surface energy components. Therefore, it is good to have a bitumen with a high acid base surface energy component. Bitumens with high Lifschitz-Van der Waals surface energy components inhibit short-term healing. Therefore, it is good to have a bitumen with a low Lifschitz-Van der Waals component of surface energy.

7. Based on the contrast-comparison statistical analysis of the primary experiment, bitumens with high aromatic content yet low amphoteric content possess the favorable surface energy components that promote good short- and long-term healing. AAM is an example of a good healer and AAM is a highly aromatic bitumen; yet it has a very low asphaltene content. This may mean that bitumens with "mobile aromatics," like AAM and AAG, are more amenable to healing than bitumens that are polar yet the polarity is "immobilized" through a high, interactive asphaltene content, which is perhaps promoted by the presence of amphoterics. The effect of hydrated lime, which may interrupt the effect of highly polar and immobilizing molecules by adsorption on the surface of the hydrated lime, seems to support this hypothetical conclusion.

8. The quantification of healing via the healing index may be confounded by other effects such as molecular structuring, temperature build-up during cyclic loading, and temperature dissipation during rest periods, plastic deformation during loading, and stiffness differences among bitumens evaluated. Each of these factors was carefully considered in this study. Although these factors are important, they do not diminish or replace the dominant effect of healing.

9. Testing from which the healing index was calculated was performed at temperatures between 20°C and 21°C. Backcalculations of material properties using the micromechanics fracture and healing model (MFHM) developed by Lytton et al. (1998) demonstrate that damage at these temperatures is primarily due to microcrack development and growth and that recovery or healing is primarily due to microcrack healing. At temperatures above about 25°C, the MFHM proved that this was not the case and plastic flow damage dominated. This leads to the conclusion that the healing discussed in this chapter is dominated by recovery or healing at microcrack interfaces.

CHAPTER 2. LABORATORY EVALUATION OF MICROCRACK GROWTH AND HEALING VIA VIBRATIONAL ANALYSIS

Summary

The purpose of this task was to evaluate the change in stiffness of asphalt concrete due to temperature effects, damage growth, and healing during rest periods. Specifically, two asphalt mixtures were compared to qualitatively determine which had a greater potential for healing when subjected to fatigue loading. A combination of impact resonance and beam fatigue testing was used to accomplish this research objective.

Materials and Sample Fabrication

The laboratory generated specimens tested during the course of this research were fabricated using Watsonville granite aggregates and AAD and AAM asphalt cements. Detailed information on the asphalts and aggregate is given in Volume 4.

The mixture was compacted into a 76-mm (3-in) deep, 450-mm (18-in) square wood and steel mold using the rolling wheel compaction method. Target air void content was 4%   0.5%. The slab was allowed to cool for 24 hours before being removed from the mold. Then, 76-mm (3-in) square by 381-mm (15-in) beams were sawn from the slab after conditioning at room temperature for 2 days. The beams were then subjected to the testing described below.

Test Method

The impact resonance method was chosen as the standard means of evaluating changes in stiffness due to temperature, damage growth, and healing during rest periods. The dynamic modulus of elasticity from the impact resonance test is a 'smear modulus,' meaning it is the modulus of the entire specimen, not just a central, damaged portion.

The impact resonance method is described in ASTM C 215 as a means of determining elastic properties of a given material based on the resonant vibrational response due to an impact load. The impact resonance method has been shown to produce very repetitive, consistent results for portland cement concrete (Carino, 1992) and for asphalt concrete (Whitmoyer and Kim, 1994). The error associated with the impact resonance tests for the two mixtures in this research is less than 3%. Due to the impact nature of loading, the impact resonance method measures the elastic modulus in the glassy (purely elastic) region. Thus, the increase in modulus after rest periods is not affected by time-dependent relaxation and is attributed to microcrack healing in the asphalt concrete. The inexpensive associated equipment costs and the small amount of time required to set up, conduct, and analyze the results from the impact resonance method are additional positive aspects for choosing this as a standard method.

To understand the effect of an impact load on a given body, one must start with the fundamental concepts of continuum mechanics. When dealing with the theory of elasticity, a given body is considered in equilibrium under the action of applied forces with the deformations already reaching their static displacements. These assumptions are sufficiently accurate for problems in which the time between the application of force and the resulting equilibrium is short compared with the time in which the observations are made. When considering the effect of forces applied over a very short observational time period, the effects should be evaluated in terms of stress wave propagation (Kolsky, 1963). ASTM C 215 involves an impact force of short duration and therefore needs to be evaluated in the light of stress wave propagation.

A stress wave can be defined as a traveling dynamic transient in a solid that involves a disturbance of particles away from their previous positions, thus involving motion and changes in relative position. Therefore, the concepts of strain, stress, kinetic energy, potential energy, and momentum can be applied.

The dispersion produced by a radial motion of a stress pulse traveling through a bar and the resulting internal friction will cause the length of the stress pulse to continually increase. The discontinuous step-like motion of the stress pulse will become rounded. When the length of the stress pulse becomes longer than the rod, the system can be considered as a whole bar moving with a constant velocity while simultaneously performing free oscillations about its center of gravity. The oscillations will decay, leaving only forward momentum, which is the motion considered in basic rigid dynamics (Kolsky, 1963).

Every cylinder or prismatic bar has particular resonant longitudinal, transverse, and torsional frequencies. These frequencies are a function of the specimen's size, shape, mass, elastic properties, and the mode of vibration produced in the specimen (McGonnagle, 1961). Whitmoyer and Kim (1994) have demonstrated that the above fundamental principles behind the impact resonance method, which were originally developed for testing portland cement concrete, can be applied to the testing of asphalt concrete.

Only one mode of testing, longitudinal, was performed on the beam specimens in this research. The test configuration used in this research is shown in Figure 22. The impact was produced by a steel ball with a 2.5-cm (1.0-in) diameter. A piezoelectric accelerometer with an operating frequency range of 100 to 10,000 Hz and a resonant frequency of 100,000 Hz was used. The maximum data acquisition rate was 500,000 points per second using the Rapid Systems data acquisition system.

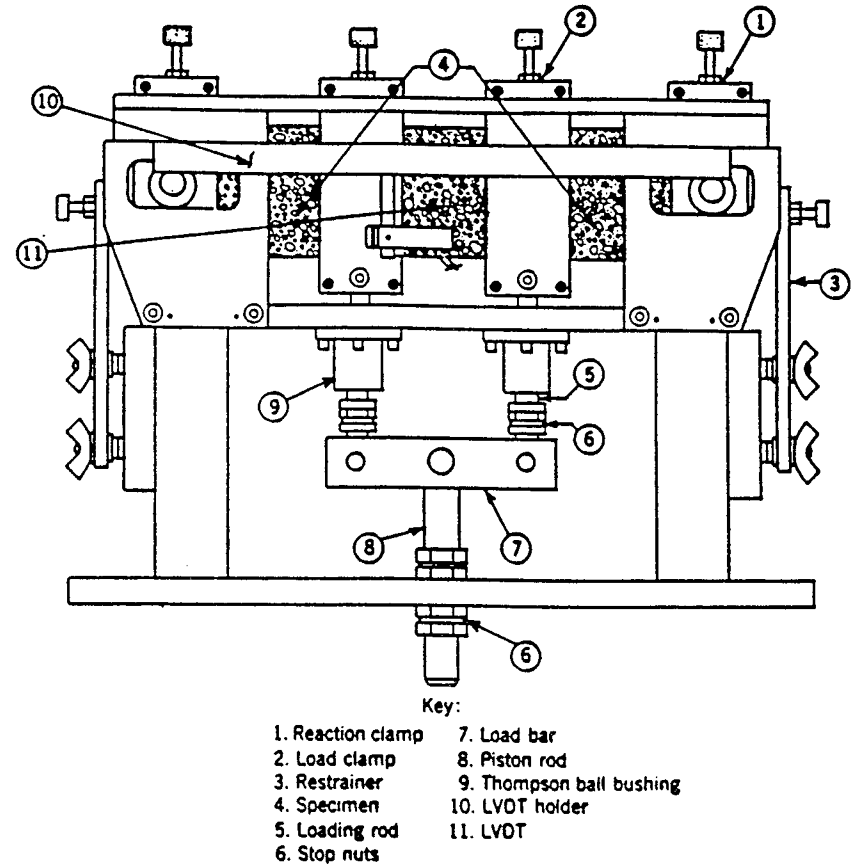

Figure 22. ASTM C 215 Experimental Test Setup.

The effect of support type on the moduli values calculated from the impact resonance test are negligible (Whitmoyer, 1993). Therefore, a 7.6-cm (3-in) by 3.8-cm (1.5-in) by 1.3-cm (0.5-in) foam support was placed at each end and in the middle of the beam to minimize the sagging effect of the beam specimens at higher temperatures.

The vibrational signal was sampled and processed using Fast Fourier Transform (FFT) technique to determine the maximum resonant frequency of the material under the longitudinal testing mode. From the resonant frequency, the elastic modulus was determined using the following equations from ASTM C 215 in English units:

$$E = D\,W\,N_L^2 \tag{13}$$

where:

E = elastic modulus (psi),

W = weight of specimen in pounds,
N_L = resonant longitudinal frequency in Hz,
for a cylinder,
D = 0.01318 (L / d^2) (s^2/in^2),
L = length of specimen (in),
d = diameter of specimen (in),
for a prism,
D = 0.01035 (L / bt) (s^2/in^2),
L = length of specimen (in),
b,t = dimensions of cross section of prism (in)

The third-point loading bending beam fatigue machine in Figure 23 was the means by which flexural damage was induced in the beam specimens. The third-point loading creates a constant bending moment in the center third of the beam, where the damage is concentrated. Flexural stiffness can be calculated from load and deflection readings. This is a measure of the stiffness for the center or damaged portion of the specimen only, not the entire specimen as in the impact resonance method.

To accurately control the test temperature, a 1.2-m (4-ft) by 1.2-m (4-ft) by 2.4-m (8-ft) environmental chamber was constructed to house the beam fatigue machine. A specifically designed air temperature control system was installed to maintain the test temperature at 20°C (68°F). All the laboratory experiments using the beam fatigue machine were performed in the environmental chamber, which controlled the test temperature within ±0.26°C (1°F) of the target temperature.

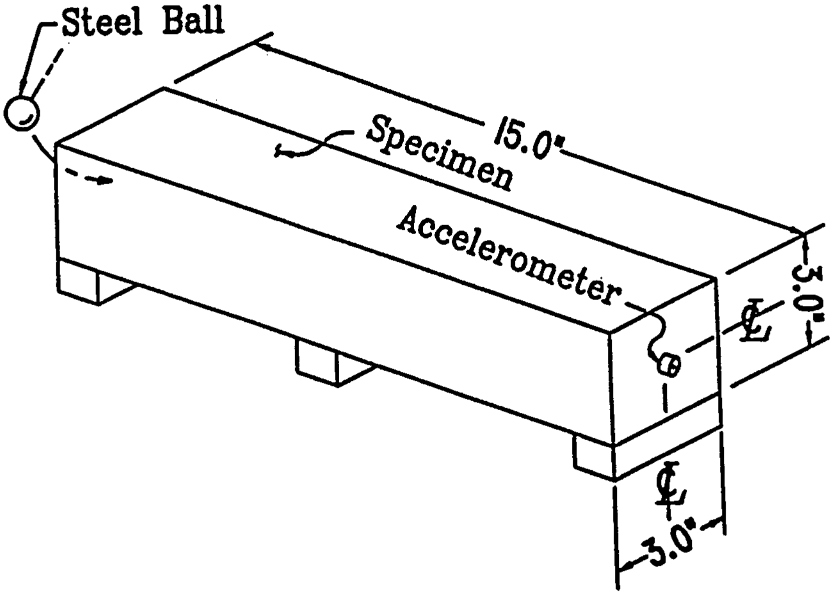

Figure 23. Schematic Diagram of Third-Point Load Beam Fatigue Testing Machine (Courtesy of the Asphalt Institute).

Experimental Plan

The experimental procedure aimed to evaluate the effect of rest periods and temperature on fatigue damage and healing potentials of different mixtures. First, impact resonance tests were performed on three specimens at several temperatures ranging from -5°C to 40°C to develop modulus-temperature relationships for each mixture type. Beam specimens of each mixture (AAM and AAD) were then subjected to the following test procedure:

1. All the specimens were initially tested at 20°C in the longitudinal testing mode to obtain the longitudinal resonant frequencies. Base temperature for this procedure was 20°C because of clearer signals than at higher temperatures and to minimize the effects of sagging on the resonant frequency measurement.
2. The same set of fatigue loading was applied to two specimens, which were then tested using the impact resonance method. The number of fatigue cycles for this loading group was small to induce a low level of damage in the specimens.
3. The two fatigued beams were exposed to healing temperatures of 20°C and 60°C respectively for 4 hours.
4. The beams were then conditioned to 20°C for at least 6 hours and tested again using the impact resonance method.
5. More loading cycles were applied to the specimens to induce a medium damage level.
6. Steps 2 through 4 were then repeated.
7. Steps 5 and 6 were then repeated with a high damage level.
8. The two beam specimens were then fatigued to failure, defined as 50% reduction in flexural stiffness. Number of loading cycles to failure (N_f) was recorded for each specimen.

Load and deflection data were collected periodically throughout the fatigue tests to determine the flexural stiffness of the beam specimens. Impact resonance tests were also performed at intermediate fatigue cycles to define the shape of the dynamic modulus of elasticity versus number of fatigue cycles curve.

Discussion of Results

Modulus-Temperature Relationship

Undamaged beam and cylindrical specimens were tested in the longitudinal mode at several temperatures ranging from -15°C to 50°C to develop the modulus-temperature relationships for both the AAM and AAD mixtures. The dynamic moduli of elasticity were then calculated from the longitudinal resonant frequencies. As seen in Figure 24, the impact resonance method is able to measure the change in stiffness of the mixtures as the temperature increases.

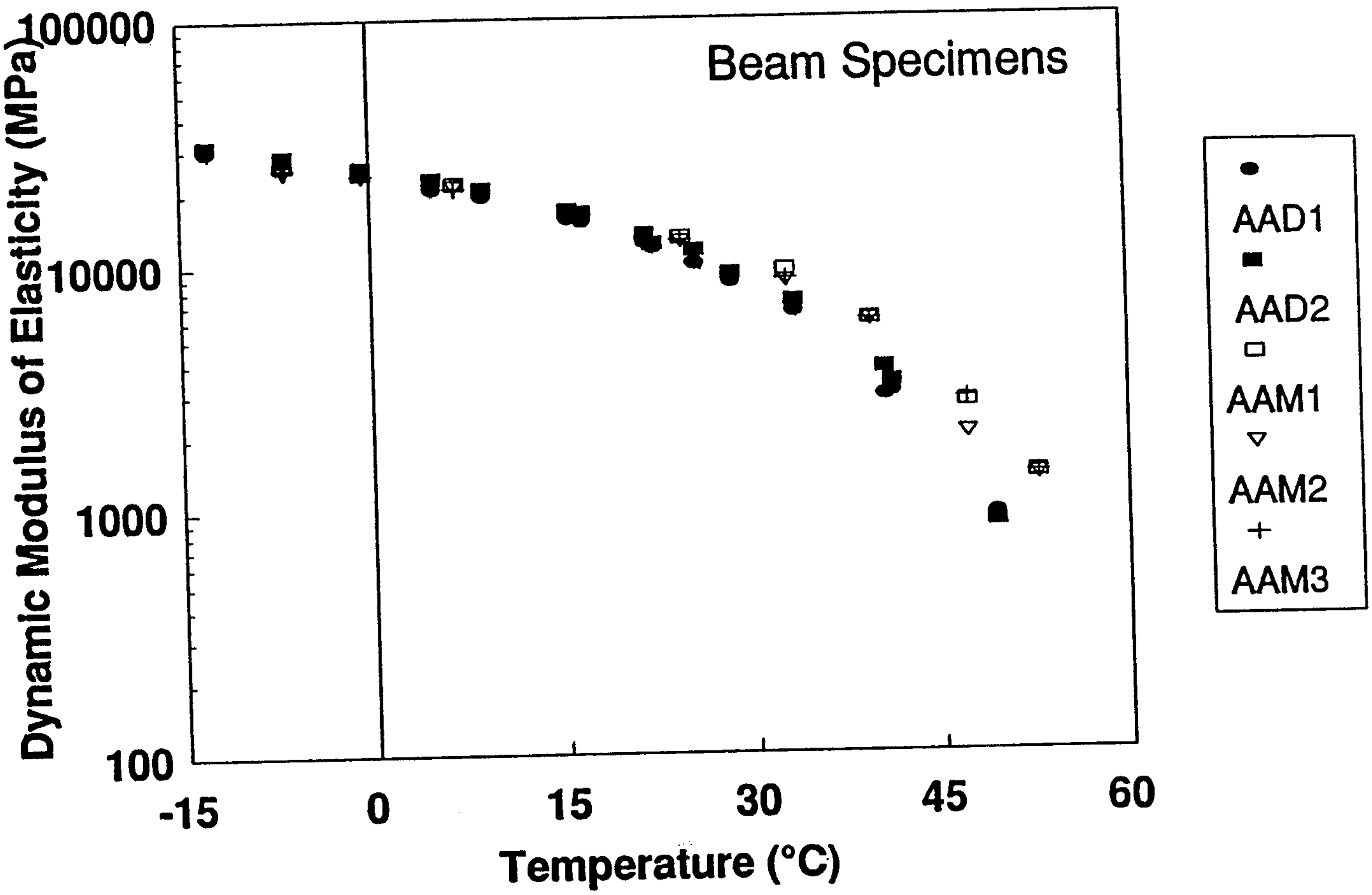

Figure 24. Comparison of Modulus-Temperature Relationship for AAM and AAD Beam Specimens.

At higher temperatures, above about 25°C, the AAM mixture specimens have a greater dynamic modulus of elasticity than the AAD mixture specimens. Below 25°C, it is difficult to determine, according to the modulus temperature curve, which mixture has a higher dynamic modulus of elasticity. In previous creep, relaxation, and dynamic modulus testing, higher moduli values were observed from the AAM mixture, even at the lower temperatures (Kim et al., 1994a). The fact that this trend is not seen with the impact resonance testing indicates that the temperature range where the effect of asphalt binder type becomes relatively insignificant is higher in the impact resonance testing than in the creep, relaxation, and dynamic modulus testing. This difference is due to a combination of the faster rate of loading and lower strain employed in the impact resonance testing over the other testing methods.

At the testing temperature (20°C), the dynamic moduli of elasticity of the AAM specimens are generally greater than the moduli measured from the AAD specimens, but that difference is usually less than 10%.

Evaluation of Microcrack Growth and Healing

As a means of evaluating the fatigue damage growth and healing, a combination of the flexural beam fatigue test and the longitudinal impact resonance test is performed on beam specimens at 20°C (68°F). Three different loading histories are applied to evaluate the effect of rest period, healing temperature, and mixture type:

1. Repetitive loading to failure at 20°C, interrupted periodically to conduct the impact resonance testing,
2. Repetitive loading to failure at 20°C with three rest periods at 20°C, and
3. Repetitive loading to failure at 20°C with three rest periods at 60°C.

During all three tests, load and deflection data are collected periodically to calculate the flexural stiffness of the specimens. After the healing periods in tests 2 and 3, 200 loading cycles are applied to the beams before the first flexural stiffness is determined in order to allow stabilization of the loading and measurement devices. In the healing tests, the impact resonance test is conducted at several points between rest periods, in addition to immediately prior to, and after the completion of each rest period. The specimens subjected to the 60°C healing temperature in test 3 are allowed to cool for at least 6 hours to reach 20°C before testing resumed.

Changes in the dynamic modulus of elasticity and flexural stiffness measured from test 1 are presented in Figures 25a and 25b, respectively. Both the dynamic modulus of elasticity measured from the impact resonance method and the flexural stiffness obtained from load and deflection data decrease as more loading cycles are applied (i.e., the damage in the beam increases). The damage evolution curves for both AAM and AAD mixtures follow the classic S-shape for load controlled fatigue.

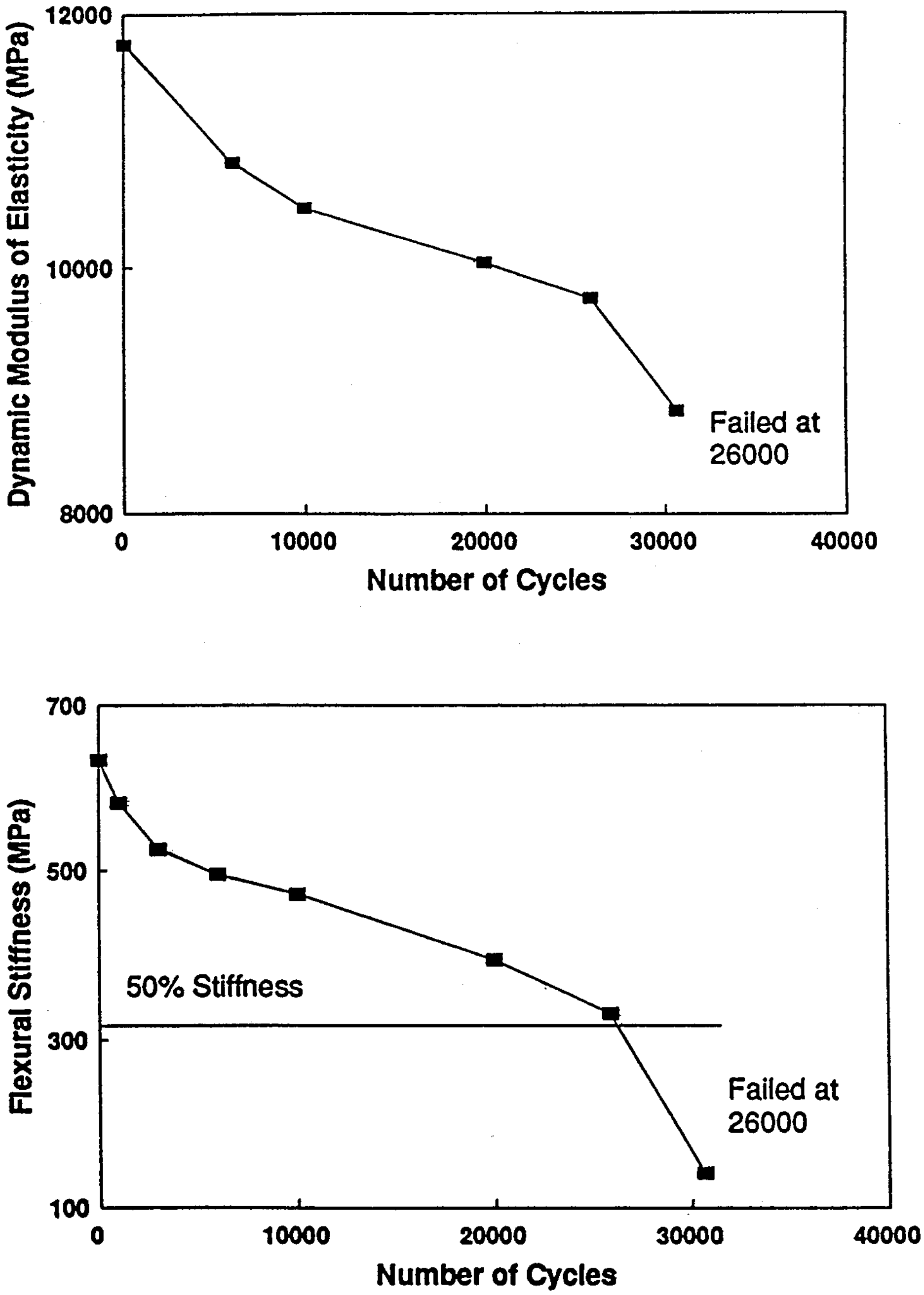

Figure 25. Typical Fatigue Damage With No Rest Periods (a) Dynamic Modulus of Elasticity (b) Flexural Stiffness.

The number of cycles to failure in test 1 depends on the load applied, the test temperature, and the type of mixture tested. In this research, the test temperature is fixed at 20°C. The AAM mixture is stiffer than the AAD mixture, and hence to enable direct comparison between the two, the load level applied to the AAM specimens is greater than that for the AAD specimens. Based on the number of cycles to failure determined from test 1, an appropriate number of cycles representing low, medium, and high damage are selected for introduction of rest periods.

Changes in the dynamic modulus of elasticity and the flexural stiffness during the healing tests are presented in Figures 26 and 27, respectively. These are typical curves for both the AAM and AAD mixtures. In both Figures 26 and 27, the beneficial effect of the healing periods on both the dynamic modulus of elasticity and flexural stiffness is obvious. An increase in the dynamic modulus of elasticity and flexural stiffness occurs after each rest period. This phenomenon has also been observed in surface wave testing of in-service pavements (Kim and Kim, 1997, Kim et al., 1995b).

Rest periods extend the fatigue life of the specimen by essentially shifting the fatigue curve to the right. After each rest period, the modulus or stiffness follows a negative power curve until it re-establishes the curvature that would have been created if no rest periods were applied. This is the point where the healed microcracks have reopened to the extent prior to the rest period and additional crack growth starts to occur. The benefit of the rest period has diminished and the stiffness continues to decrease as though no healing had occurred. Since there was a period where original crack growth was not happening (instead refracture of the healed surfaces), the new fatigue curve is shifted to the right, i.e., the same level of damage is occurring at a greater number of cycles. This increases the ultimate number of cycles the specimen endures before failure.

In effect, the fatigue failure curve is 'stretched' with the application of rest periods, as seen in Figure 28. This lateral 'stretching' of the stiffness versus number of cycles has been shown previously by Raithby and Sterling (1970). The rest periods in Raithby's work were applied after each loading cycle and were very short in duration; however, the effect of the rest periods remains the same as in this research:; to extend the number of cycles to failure.

In general, the increases in dynamic modulus of elasticity and flexural stiffness for 60°C healing periods are greater than the corresponding increases for the 20°C healing periods. The healing capacity of the asphalt cement is enhanced as a result of its increased ability to flow and further close more microcracks at higher temperatures.

An interesting feature in Figure 26b is that the flexural stiffnesses after rest periods at the 60°C healing temperature are greater than the original flexural stiffness. Typically, this is seen with both AAM and AAD specimens healed at 60°C. Experimental error associated with repositioning the beam specimen in the beam fatigue machine and

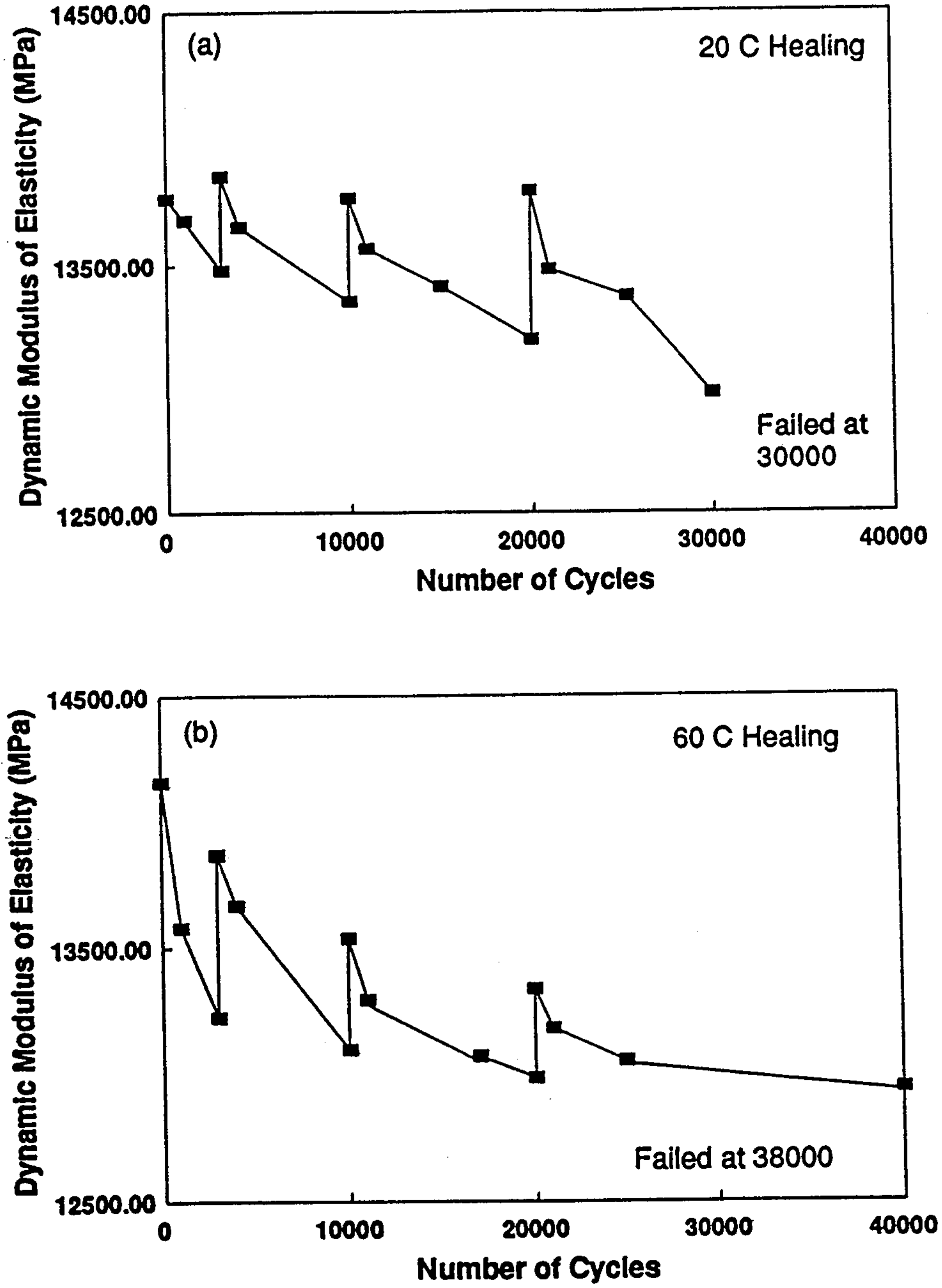

Figure 26. Typical Dynamic Modulus of Elasticity Through Fatigue Damage and Rest Periods (a) 20°C Healing (b) 60°C Healing.

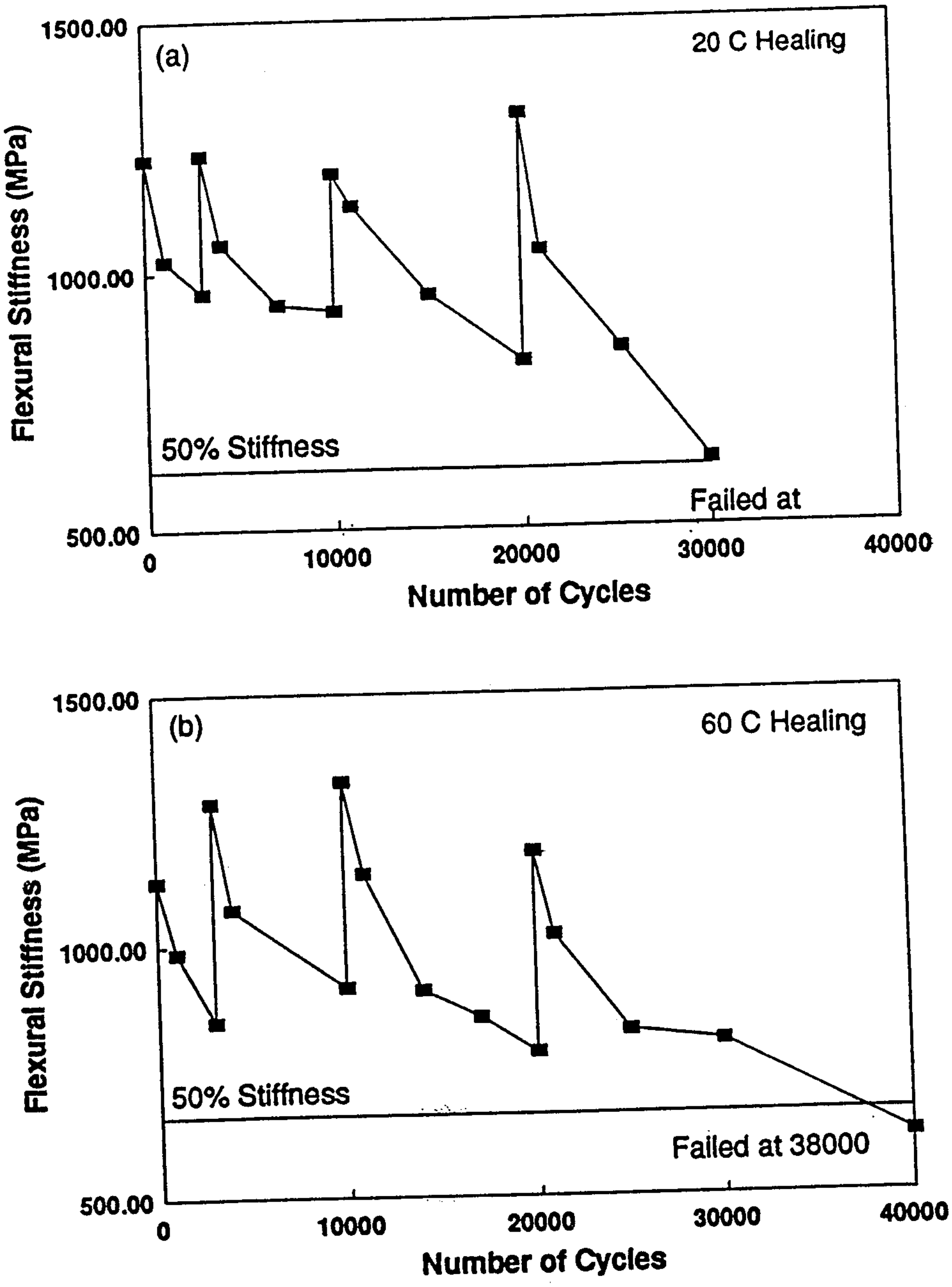

Figure 27. Typical Flexural Stiffness Through Fatigue Damage and Rest Periods (a) 20°C Healing (b) 60°C Healing.

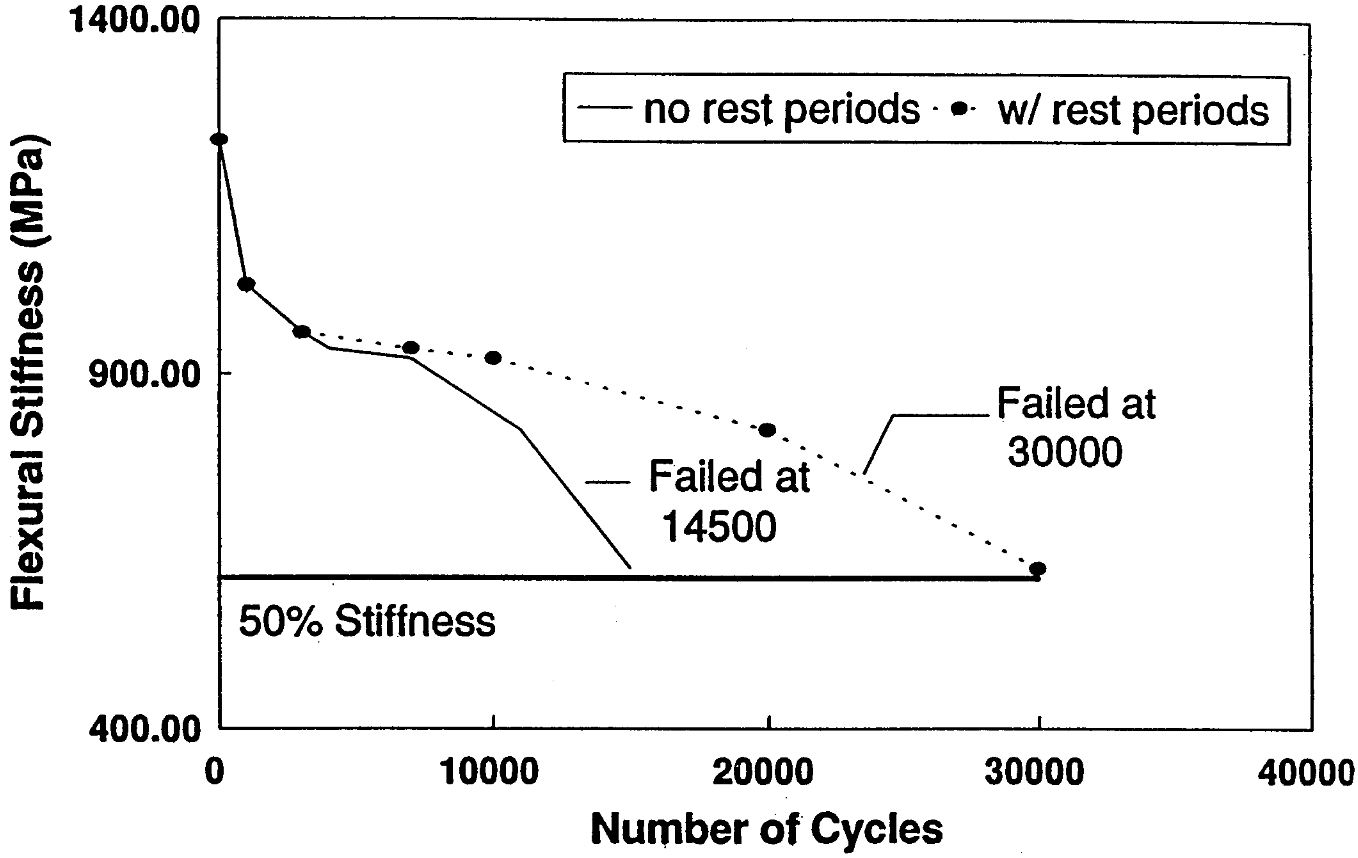

Figure 28. Flexural Stiffness Versus Number of Cycles to Failure With and Without Rest Periods.

attaching the LVDT to the specimen in the same spot as prior to the rest period are responsible for this difference. A slight change in placement of the beam or LVDT has the potential to significantly change the deflection reading, depending on where damage is concentrated. Only the flexural stiffness is affected by the deflection readings, and hence this discrepancy is not seen with the dynamic modulus of elasticity measurements.

Comparison of AAM and AAD Healing Characteristics

The healing performance of the AAM and AAD mixtures are compared to determine which mixture has a better healing potential. The four methods of measuring healing potential used to compare the two mixtures are summarized in table 9.

The percentage increase in number of cycles to failure is calculated based on the differences between control tests without rest periods and healing tests where the specimens were allowed three rest periods. Using this method, the AAM mixture shows a much greater potential for healing than the AAD mixture at both temperatures. Also, for both mixtures, the higher healing temperature results in greater increases in the number of cycles to failure. The N_f values for the AAM control tests are significantly lower than those for the AAD control tests, which contributes to the large difference between the two mixtures using this healing indicator. The percentages reported are averages of at least two replicate tests at 4% air voids.

Table 9. Comparison of Healing Potentials of the Two Mixtures.

Method	**Percent Increase**			
	AAM		**AAD**	
	20°C	**60°C**	**20°C**	**60°C**
Number of Cycles to Failure	150	280	41	60
Damage Indicator	42	45	18	15
Horizontal Increase	52	47	32	25
Increase/Drop	70	92	50	70

In an effort to eliminate the effects of the different number of cycles to failure for the control tests, a damage indicator was developed. The damage indicator is defined as the ratio between the number of cycles a specimen has endured at a particular rest period and the number of cycles to failure for that particular specimen. Alternatively, the damage indicator can be described as the percentage of fatigue life consumed at a specific time. The damage indicator is shown graphically in Figure 29. The percentage increases in modulus and flexural stiffness at rest periods with similar damage indicators are reported in table 9. These values are based on most of the tests run, regardless of air void content. The damage indicator shows that the AAM mixture is a better healer than the AAD mixture but does not indicate much difference between the healing temperatures. It is unknown why the damage indicator shows higher healing at 20°C than at 60°C in the AAD mixture .

The horizontal increase is the ratio between the total number of cycles gained from the three rest periods and the number of cycles to failure. The number of cycles gained is determined by evaluating when the modulus or stiffness returns to the value prior to the rest period. This is graphically illustrated in Figure 29. Each value that is reported in table 1 is an average of at least three specimens. This method is actually a measure of how long it takes for the healed surfaces to refracture once fatigue loading resumes. It indicates the healed material's resistance to damage evolution. Assuming that a higher healing temperature only increases the amount of healed cracks and not the strength of the healed cracks, this indicator cannot conclusively evaluate the effect of healing temperatures. At higher temperatures, the number of cycles gained from the rest periods (numerator) and N_f (denominator) increase by the same number of cycles. The magnitude of the increase is such that the indicator (ratio of the two) essentially remains the same for a specific mixture. The number of cycles gained is determined graphically and the increase due to healing temperature can be close to the errors associated with this method, contributing to the similar values and the reversed trend with respect to healing temperature in table 1.

A fourth method of evaluating the healing potential of the two mixtures is to compare the drop in modulus and flexural stiffness before each rest period to the corresponding increase after the rest period. To do this, the increase (C-B in Figure 29) was divided by the drop (A-B), expressing the benefit of the rest period as a percentage of the modulus lost during the previous fatigue cycles. This indicates that AAM has a greater healing potential than AAD and that the higher temperature increases healing. The values reported are averages for both flexural stiffness and dynamic modulus of elasticity at all rest periods for specimens with approximately 4% air voids.

All four methods of evaluating the healing potential indicate that AAM is a better healer than AAD. This has been observed in uniaxial cyclic fatigue testing of the two mixtures as well (Kim et al., 1997). The results also present a general increased potential for healing at higher healing temperatures, with the exception of the horizontal increase method for the reasons described above.

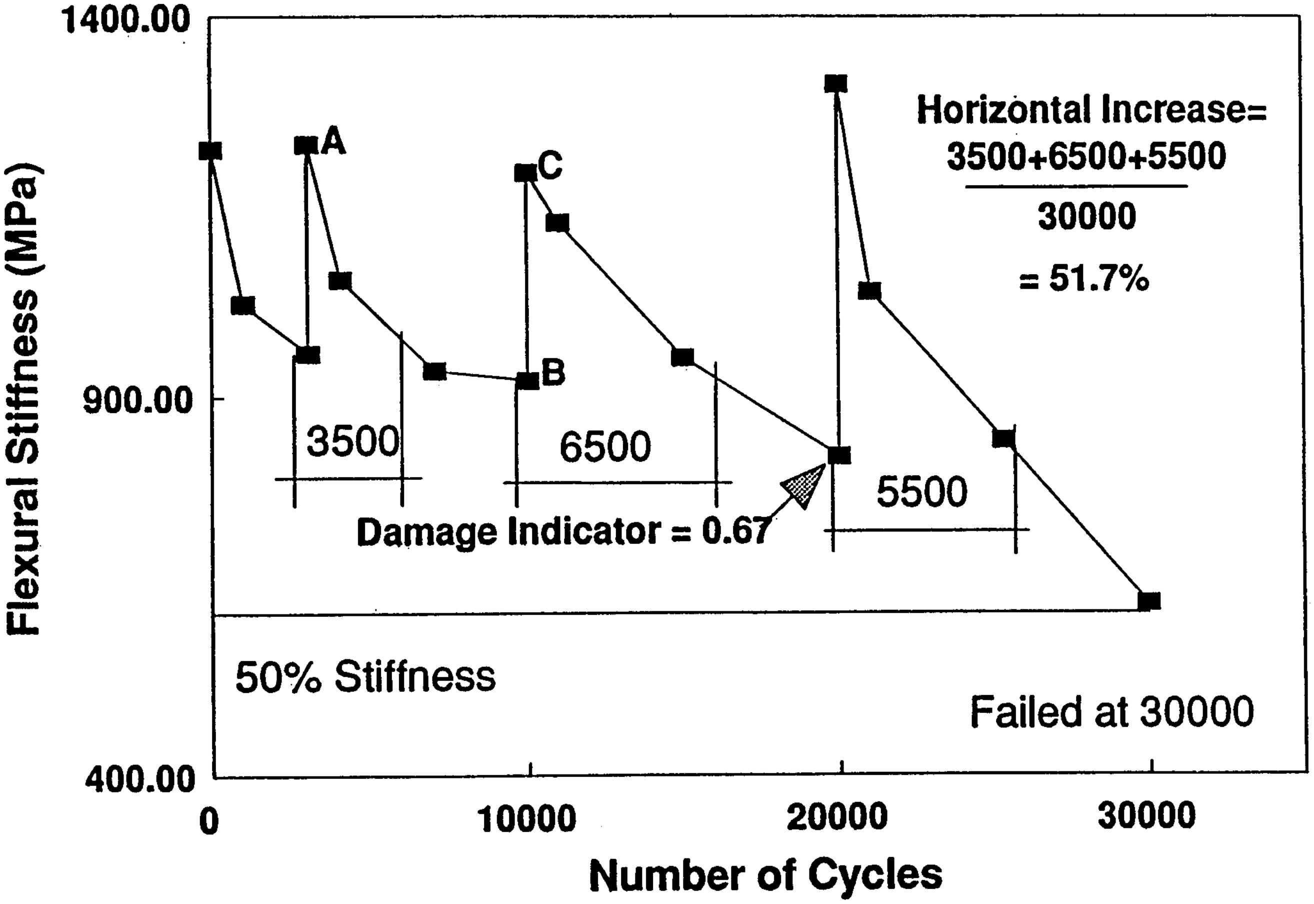

Figure 29. Graphical Representation of Healing Comparison Methods.

Conclusions

With increases in temperature or damage, the dynamic modulus of elasticity as measured from the impact resonance test decreased, as would be expected. When rest periods were applied, increases in dynamic modulus of elasticity and flexural stiffness were observed. Due to the impact nature of loading for the impact resonance test, the increases were attributed to healing of microcracks within the specimen. Generally, greater increases occurred when the rest periods were conducted at 60°C than at 20°C. The difference is attributed to increased flow of the asphalt cement at the higher temperature.

The healing potentials of AAM and AAD asphalt cements were evaluated using four different indicators. Each of the comparisons indicates that the AAM asphalt cement is a better healer than the AAD asphalt cement, agreeing with uniaxial cyclic fatigue test results documented in Volume 4.

CHAPTER 3: FIELD EVALUATION OF FATIGUE DAMAGE GROWTH AND HEALING USING STRESS WAVE METHOD

Summary

The first objective of this task is to detect the microcrack damage and healing of asphalt surface layers in in-situ pavements. Therefore, monitoring the pavement condition for the whole or a large portion of the service life is intended. The second objective is to establish a dependable stress wave test method and its analysis.

The test procedure and the results of four pavement sections at the FHWA Turner-Fairbank Highway Research Center in McLean, Virginia, are described in this section. Repetitive wheel loads have been applied to these pavements using the Accelerated Loading Facility (ALF) with periodic introduction of 24-hour-long rest periods. The dispersion analysis results are presented as a function of elapsed loading time, and discussions are made based on the comparison of the test results and crack information obtained from the visual condition survey.

In addition, the results from testing on seven pavement test sections at the Minnesota Road Research Project (Mn/ROAD) during nine trips are presented. The significance of this study is that the test pavements are loaded by vehicular highway and rural road traffic and are subjected to actual environmental conditions. Therefore, this work will determine the ability of stress wave testing to measure microcrack damage growth and healing of asphalt concrete pavements in the field. Wavespeed and attenuation measurements are used to quantify the damage growth and healing. Comparisons are made with visual condition surveys and lab tests on cores taken from the pavement sections.

To maintain the effectiveness of the flow, only the results that are necessary for discussion are presented in this section. Some additional figures for the ALF study and the Mn/ROAD project are presented in Appendix A, and numerical solutions for wave propagation in layered media in Appendix B. Also, detailed information on surface wave testing and analysis methods is presented in Appendix C.

Stress Wave Test Method

An effective pavement maintenance management program requires a procedure by which the in-situ condition of existing pavements can be evaluated. Such a procedure should have the capability to yield data from which estimates can be made of the remaining life of the structure. One part of the procedure involves a determination of the in-situ elastic properties of the materials in the existing pavement. Commonly used nondestructive devices for pavement evaluation, such as the falling weight deflectometer or Dynaflect, are known to be fairly insensitive to the changes in asphalt surface layer due to the low-frequency (or long wave length) impulse or vibration these devices generate.

A method with considerable potential to provide the type of data required to determine the material and/or geometric characteristics of in-situ pavements is the stress wave method. It is a nondestructive method of testing that involves the excitation of the pavement by means of a suitable impact source and the measurement of the response of the structure to this loading. This method makes use of the surface wave transients created by an impulse load on the pavement surface to determine the wave speed in each layer, which is related to layer material properties.

In this study, four accelerometers (model 303A02) and a power supply (model 482A05) from Piezotronics, Inc. (PCB) are used for capturing the acceleration of the pavement surface due to impact. The data is acquired via 4-channel oscilloscope (model 420A) from Tektronics, Inc. attached to a 486 portable computer.

Prior to any loading on a pavement, hexhead nuts were epoxied to the pavement surface at the locations 152 mm (6 in), 305 mm (12 in), 457 mm (18 in), and 610 mm (24 in) away from designated impact locations. The sensors were attached on the nuts using magnetic bases. A typical configuration of the stress wave test is shown in figure 30. Since the objective of this study was to investigate the changes in surface layer properties during fatigue loading and rest periods, a lightweight hammer of 257 g (8 oz) was used to generate an impact, which contains most energy in high frequency components.

Stress Wave Theory

In an unbounded isotropic solid, only two types of wave (longitudinal and shear) can propagate. In a solid half-space with a bounded surface (like the surface of a pavement), however, an elastic surface wave may also occur. Surface waves are nondispersive in the homogeneous, isotropic, linear elastic, solid half-space. However, when the half-space is a layered medium, surface waves are dispersive in nature: that is, the phase velocity (the velocity of each frequency) depends on the frequency. Surface waves contain vastly more energy (about 67% under a vertical impact to a half-space) and travel slightly slower than the shear wave, whose wave speed is around 60% of the longitudinal wave speed.

The relationship between the surface and shear wave velocities arises from the solution of the two-dimensional equations of motion for a continuum. The solution to the following sixth order expression relates the surface wave speed to the shear wave speed (Kolsky, 1963):

$$\alpha^6 - 8\alpha^4 + 8\left(3 - \frac{1-2v}{1-v}\right)\alpha^2 - 16\left(1 - \frac{1-2v}{1-v}\right) = 0 \tag{14}$$

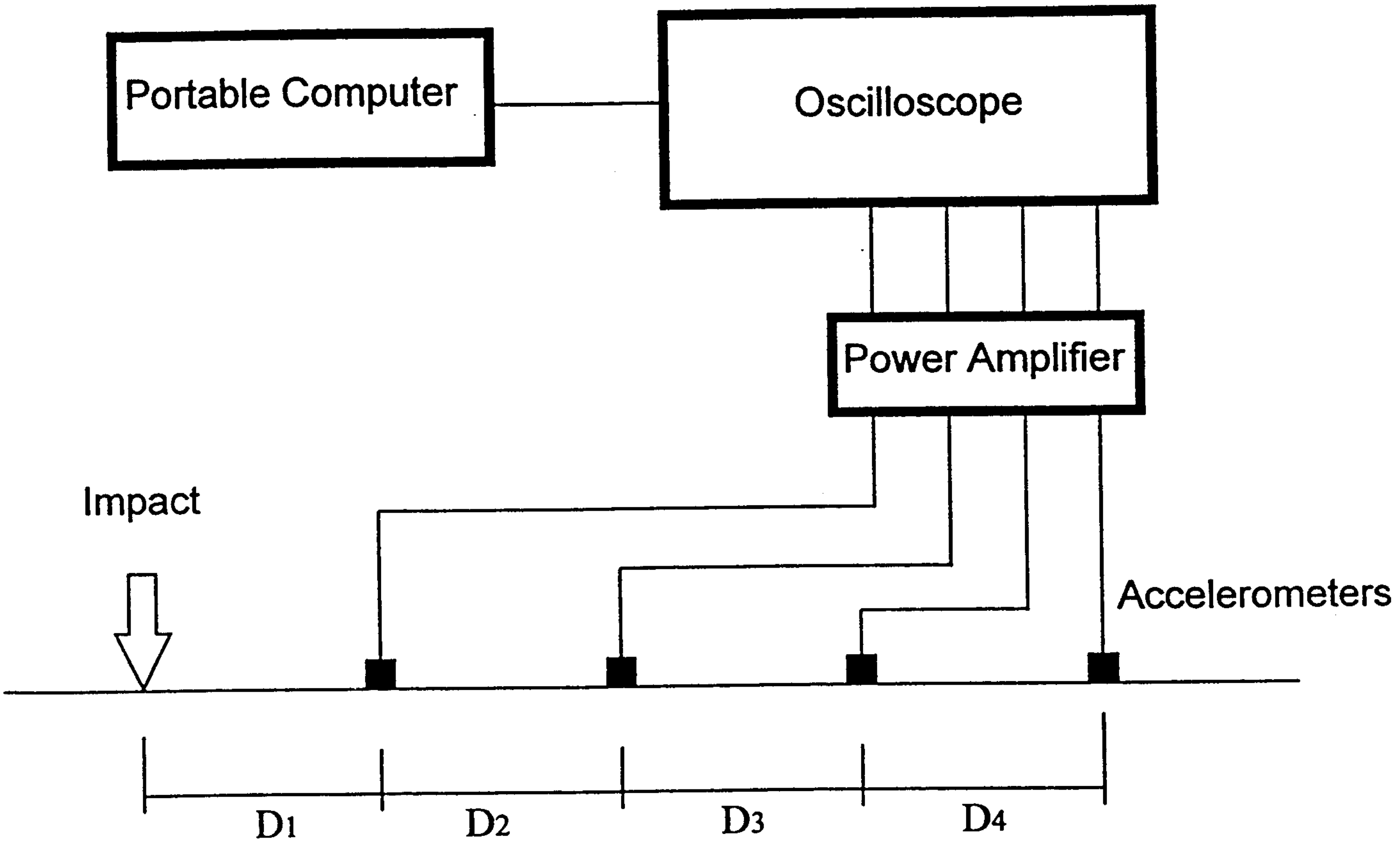

Figure 30. Stress Wave Test Configuration.

where α is the ratio of the surface wave speed to the shear wave speed, and ν is Poisson's ratio.

In an elastic, isotropic medium, the elastic constants are determined from the surface wave velocity according to the following relationships:

$$V_R = \alpha \cdot V_s \tag{15}$$

$$G=\rho \cdot V_S^2 = (\gamma \; / \; g) \cdot V_S^2 \tag{16}$$

$$E = 2G(1+\nu) \tag{17}$$

where:

V_S = shear wave velocity,
V_R = surface wave velocity,
ρ = density of the material in the layer,
G = shear modulus,
γ = unit weight,
g = acceleration of gravity, and
E = elastic modulus.

These relationships allow one to calculate elastic modulus from a surface wve velocity measured from the SASW test. A more detailed explanation of wave propagation theory can be found in Appendix C.

PART I: EVALUATION OF PAVEMENT SECTIONS IN FHWA TURNER-FAIRBANK HIGHWAY RESEARCH CENTER

Selected Pavements

Four pavement sections selected for this research were constructed on the same subgrade and the same 457-mm- (1.5-ft-) thick aggregate base with full-factorial combinations of two types of asphalt layer (AC 5 and AC 20) and two AC layer thicknesses (102 mm and 204 mm). The subgrade was plowed and recompacted up to 610 mm (2.0 ft) to ensure their homogeneity.

ALF Test Procedure

A combination of the ALF loading and the stress wave test was conducted on 102-mm (4-in-) thick pavements with AC 5 and AC 20 surface layers during their entire fatigue lives (between early December of 1994 and June of 1995). The same type of test was conducted on 204-mm- (8- in-) thick pavements with AC 5 and AC 20 surface layers from December 1995 until May 1996. Due to the FHWA's constraints in the operation of the ALF, the testing program of the 204-mm- thick pavements ended before the complete failure of these pavements.

The ALF applies cyclic loading with a period of 10 seconds per cycle. The wheel used in this study was 318-mm (12.5-in) wide with a load of 53.4 kN (12,000 lb) and tire pressure of 689.5 kPa (100 psi). The position of wheel load was controlled to produce normally distributed wandering transverse to the traffic direction. The resulting width of the wheel path was 1.07 m (42 in). The major reason for the wandering of the wheel is to minimize the rutting in the pavement due to concentrated loading so as to allow more isolated evaluation of fatigue performance.

The pavements were subjected to repetitions of a group of loading cycles followed by a 24-hour rest period. During the ALF loading and rest periods, the pavement temperature was maintained at 20°C (68°F) using a temperature control system mounted on the ALF. The temperature control system is composed of heaters, thermocouples installed in pavements, and a computer that controls that heaters based on the temperatures measured from the thermocouples. In addition, plastic barriers were placed on both sides of the ALF to minimize the temperature variation due to ambient air flow. Although higher temperatures during rest periods would have amplified the effects of microdamage healing, it was decided to keep the temperature constant throughout the fatigue life due to long periods required for heating and cooling cycles.

The number of loading cycles in each group of loading changed from 8000 cycles in the early days of testing to 25,000 cycles in the latter part of testing of 102-mm pavements. The number of loading cycles within a group was up to 50,000 cycles on 204-mm pavements. In the 102-mm sections, one section was tested for 1 week, and the ALF was moved to the other section at the end of the week. This alternating test program was repeated until the two sections failed. In the 204- mm sections, the two ALF machines were used at the same time, and therefore, there was no need of alternating the machine.

Surface wave tests were performed at the following times: before any loads were applied, immediately after each group of loading ends, and at the end of 24-hour rest periods. Surface wave data were collected from six different positions in each section. As shown in Figure 31, Positions 1 and 5 were on the center of the wheel path. Positions 2, 3, and 4 were located 152-mm (6-in), 305-mm (12-in), and 457-mm (18-in) apart from the center. One more position, named control, was selected at the outside of the wheel path and tested to monitor the effects of non-load-related variables, if there were any.

Detailed visual surface condition surveys were made periodically so that cracks on the pavement surface were mapped and crack lengths were measured throughout the fatigue life.

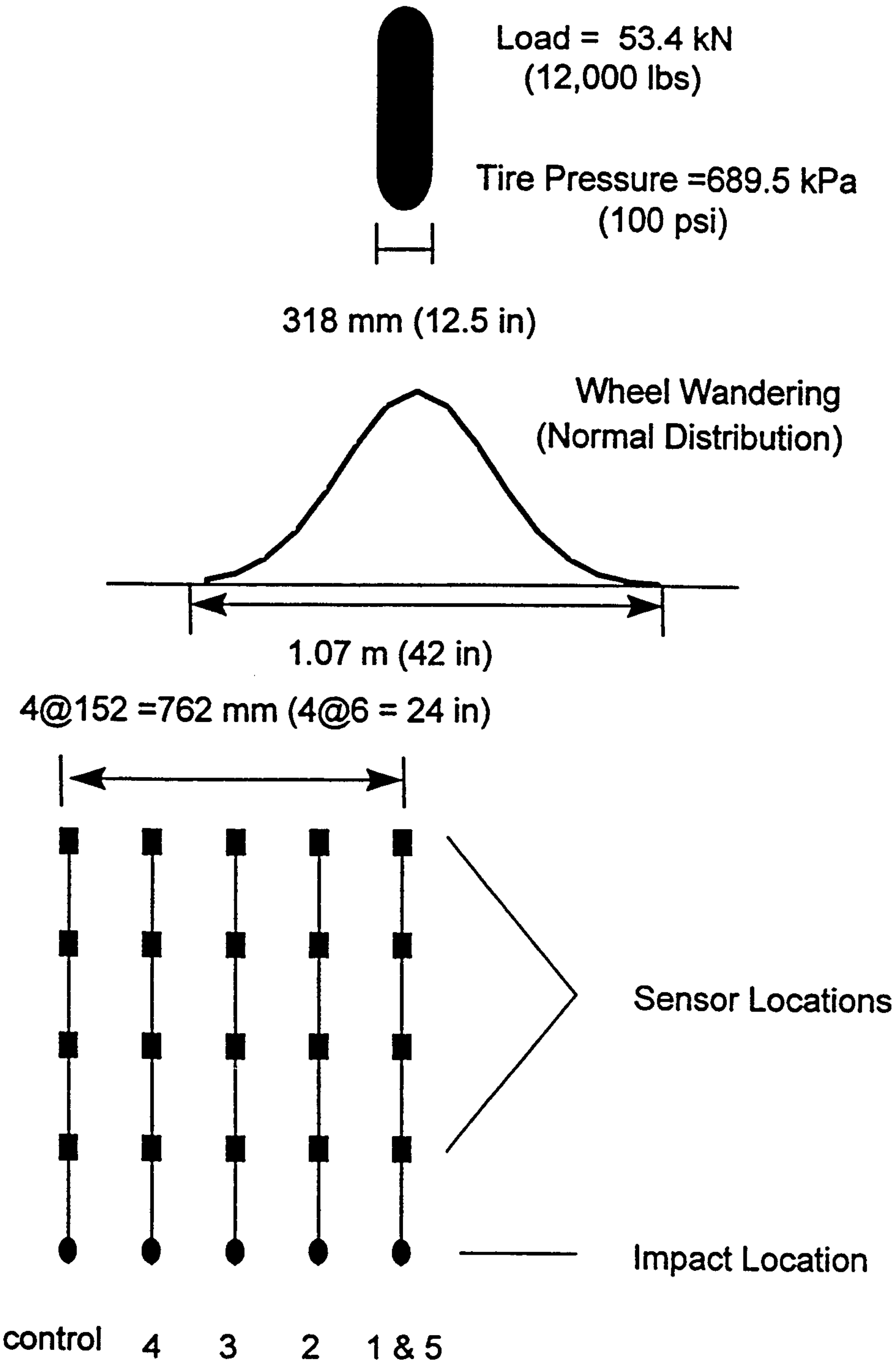

Figure 31. Test Section Layout.

ALF Section Properties

The asphalt concrete used in the test sections is a 19.0-mm nominal maximum size mixture meeting Virginia Department of Transportation designation SM-3B (Road and Bridge Specification, 1992). It is a dense-graded asphalt concrete mixture. AC 5 corresponds to PG 58-34 and AC 20 corresponds to PG 64-22 in the Superpave Binder Specification. They are unmodified binders from Venezuela's Lagoven base stock. More detailed information regarding the binder properties are found in Bonaquist and Mogawer (1997). Table 10 presents the average aggregate gradations for the asphalt concrete mixtures used in this research.

Table 10. Gradation of the Asphalt Concrete Mixture.

Sieve Size, mm	% Passing
25	100
19	98.7
12.5	76
9.5	62
4.75	44
2.36	32.5
1.18	23.5
0.6	17.5
0.3	11.5
0.15	8
0.075	5.1
% Binder	4.8

Data Analysis Methods

Dispersion Analysis

The data acquisition and the signal analysis were performed using the computer program SWAP (Stress Wave Analysis Package) developed at North Carolina State University. This program has a graphic user interface and is capable of performing Fast Fourier Transform (FFT), Spectral Analysis of Surface Waves Method (SASW), and Short Kernel Method (SKM).

The data signals were reviewed initially via an FFT routine to determine the frequency range that contained the largest amount of energy. Phase velocities of individual frequencies were then determined using the SKM. The SKM is a frequency-dependent scanning operation based upon the cross-correlation procedure described by Bendat and Piersol (1980). This method amplifies a given frequency within the time domain of a signal for purposes of determining the time that the wave took to travel between the two gauge points.

Mathematically, a single value of the SKM at a particular frequency can be determined from the following:

$$S_k(t) = \sum_{i=0}^{n-1} x\ (t+i\Delta t)\ f_k\ [i\Delta t] \tag{18}$$

where:

$S_k(t)$ = data point from SKM transform at assigned kth kernel frequency,
$f_k(i\Delta t)$ = data point from SKM kernel at assigned kth kernel frequency,
$x(t)$ = data point from real time record,
t = data point location at real time axis,
k = index of assigned SKM kernel frequency,
n = total number of data points in the assigned SKM kernel, and
Δt = time step at real time record and SKM kernel.

Detailed information and other applications of the SKM can be found elsewhere (Douglas et al., 1989; Holt et al., 1994; Kim et al., 1994). Further information about the SKM and other signal processing techniques used in this research can also be found in Appendix C.

Numerical Solution for the Multilayered System

When testing a layered structure such as asphalt pavement, surface waves can penetrate more than one layer. Thus, if one needs to obtain information from a specific layer, phase velocities of surface waves have to be converted to shear wave velocities of different layers. In this section, numerical solutions using Hankel transform are presented as a means of inverting phase velocities to shear wave velocities.

In a cylindrical coordinate system, the harmonic displacements in the spatial domain are expressed by "inverse Hankel transform" of the harmonic displacements in the wave number domain. The general solution to the wave equation formulated from the equations of motion can be expressed by

$$U(r,\theta,z,\omega)=\sum_{\mu=0}^{\infty} D_\mu \int_{k=0}^{\infty} kC_\mu\ \overline{U_\mu}\ (k,\mu,z,\omega)dk \tag{19}$$

where Cμ is the cylindrical function in the radial direction, and Dμ is the diagonal matrix corresponding to Fourier components.

For determining the displacement U(r,θ,x,ω) corresponding to the external load in the spatial domain, the displacement $\overline{U}\mu(k,\mu.z,\omega)$ in the wave number domain needs to be solved for a transformed load $\overline{P}\mu(k,\mu,z,\omega)$ in the same domain. The transformed load in the wave number domain is determined by the Hankel transform of the load in the spatial domain. Hankel transform is given by

$$\overline{P_{\mu}}(k,\mu,z,\omega) = \alpha_{\mu} \int_{r=0}^{\infty} rC_{\mu} \int_{\theta=0}^{2\pi} D_{\mu}P(r,\theta,z,\omega)d\theta dr \tag{20}$$

where the is the orthogonalization factor. The response of a layered medium in the wave number domain is given by the following:

$$[K] \cdot \overline{U_{\mu}}(k,\mu,z,\omega) = \overline{P_{\mu}}(k,\mu,z,\omega) \tag{21}$$

where [K] is the stiffness matrix of a layered system in the wave number domain. The global stiffness matrix of the layered system is constructed by combining the individual layer stiffness matrix K^j for each layer. Some elements in the matrices are overlapped considering the compatibility of displacements and the force equilibrium at layer interfaces. This procedure was first developed by Kausel (1981, 1982), in which the mathematical procedure is described in more detail. The procedure was applied to the surface wave tests of soil and pavement structure by Kausel (1981) and Gucunski and Woods (1992). Further explanation of the numerical solution for a multilayered system can be found in Appendix B.

ALF Test Results

The surface wave speeds and the elastic moduli were calculated using equations 14 through 17. Poisson's ratio was determined by equating the elastic and shear moduli obtained from the laboratory impact resonance tests (ASTM C215) in longitudinal and torsional modes. The resulting Poisson's ratio was 0.30 for the pavement temperature of 20°C. Surface wave velocities at different damage conditions were determined using the SKM. Dispersion curves (i.e., relationships between surface wave velocity and frequency) generated for the 102-mm sections at the pre-loading state are plotted in Figure 32. According to Roesset et al., (1990), the top flat portion of the curve, which has the high frequencies and the short wave lengths, can be used for the calculation of the shear wave velocity and therefore the stiffness of the asphalt layer. This procedure has been used in the analysis of pavement structures by Marwan et al., (1993) as well. Therefore, the solid arrow indicates the surface wave speed of the AC 20 pavement, and the empty arrow indicates the surface wave speed of the AC 5 pavement. The surface wave velocity from the AC 20 section is higher than that from the AC 5 section because of the higher stiffness of AC 20 surface layer.

Since the surface wave penetrates at different depths depending upon the wave length, the surface wave velocities need to be inverted to shear wave velocities of individual layers for more precise and complete evaluation of pavement layers. However, if the impact made on the pavement surface creates wave transients with frequencies that are high enough for the surface wave to stay within the asphalt surface layer, the surface wave velocity could then be directly used for the calculation of the shear wave velocity of the surface layer using equations 14 through 17 without inversion. For practical purposes, the direct calculation of shear wave velocities from the surface wave velocities is much faster and simpler than the analysis involving the inversion process. In the following, some analyses were performed to check the validity of the direct approach.

The effective sampling depth of a frequency is about 1/3 to 1/2 of the wave length of that frequency, and at a depth equal to 1.5 times the wave length, the amplitude of the particle motion is only 10% of that at the surface (Nazarian et al., 1986, 1983). The dominant frequency of typical signals obtained from the test setup and the pavements used in this study is about 10 kHz. The wave length of this frequency is about 125-mm, which yields the effective sampling depth of about 40 to 60 mm. Comparing the effective sampling depth of the dominant frequency and the thicknesses of surface layers investigated in this study, it was concluded that the direct calculation of the shear wave velocities from the surface wave velocities would be good enough to evaluate the surface layer properties. This conclusion will be supported again in a later section by comparing results from the direct approach described above and the inversion approach.

Based on these observations, the surface wave velocity obtained from the top flat portion of the dispersion curve was used as the one representing the asphalt surface layer properties. In the following two subsections dealing with fatigue damage growth and healing, the elastic modulus of asphalt surface layer reported are the ones obtained from the direct approach.

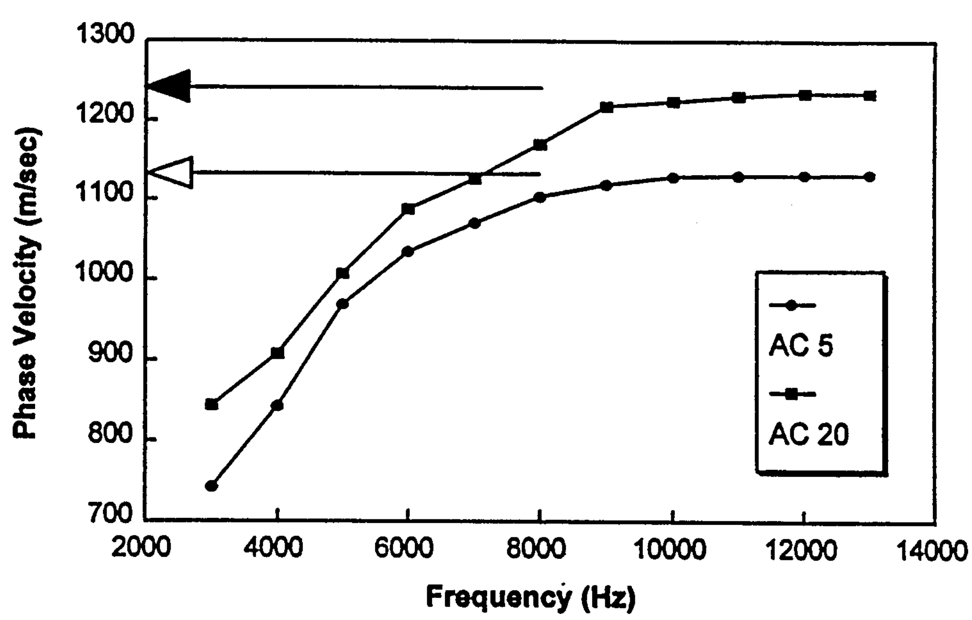

Figure 32. Dispersion Curves of the 102-mm (4-in) Pavements Before Loading.

Fatigue Damage Growth

Figures 33 and 34 present the surface wave speed change at each position as a function of the elapsed testing time for the 204-mm-thick AC 5 and AC 20 sections, respectively. Points with "-" symbol in these figures represent the data collected immediately after a group of loading cycles (i.e., at the beginning of each rest period) and those with "+" symbol indicate the data obtained at the end of a 24-hour rest period (i.e., immediately before another group of loading starts). When the phase velocity after the rest period (marked with +) is higher than that before the rest period (marked with -), the + symbol is positioned above the curve and - symbol below the curve and vice versa.

In general, except in the control, the phase velocity decreases as the number of loading cycles increases. The same trend was found from the 102-mm pavement sections. Figure 35(a) summarizes the different trends of the modulus reduction at different positions of the 204-mm AC 20 section. In Position 1 with the greatest number of load applications, the major portion of the modulus reduction occurred within 200,000 loading cycles and then the curve became relatively flat afterwards. In Figures 33 and 34 for the 102-mm pavements, most of the modulus reduction in the center positions (Positions 1 and 5) occurred within 25,000 cycles. In all the pavements tested in this study, this initial reduction in the elastic modulus appears at a later time with a more gradual slope as the offset of the testing position from the center increases. This trend is obviously related to decreasing number of loading cycles of outer positions due to the wandering load applications with the normal distribution.

In order to relate the modulus reduction observed in these figures to the cracking phenomenon, surface crack lengths measured from the condition surveys and phase velocities of the center position of the 102-mm-thick AC 5 and AC 20 sections are plotted together against the number of loading cycles in Figure 35(b). It can be observed that the AC 20 section started with a higher phase velocity because of the stiffer surface layer, but resulted in more rapid reduction of the phase velocity, earlier development of visible surface cracks, and shorter fatigue life. This figure clearly indicates that, even a long time before cracks are observed on the pavement surface, significant modulus reduction occurs in pavement systems. Since the initial densification due to the ALF loading would have increased the phase velocity and therefore the elastic modulus, the early reduction in the elastic modulus is assumed to be related to structural degradation of pavements due to microcrack initiation, propagation, and densification. This assumption is somewhat supported by the fact that the additional reduction in the phase velocity after 150,000 cycles in the AC 5 section in figure 35(b) coincides with a dramatic increase in surface crack length, indicating the failure of the pavement. This observation is less obvious in the AC 20 section.

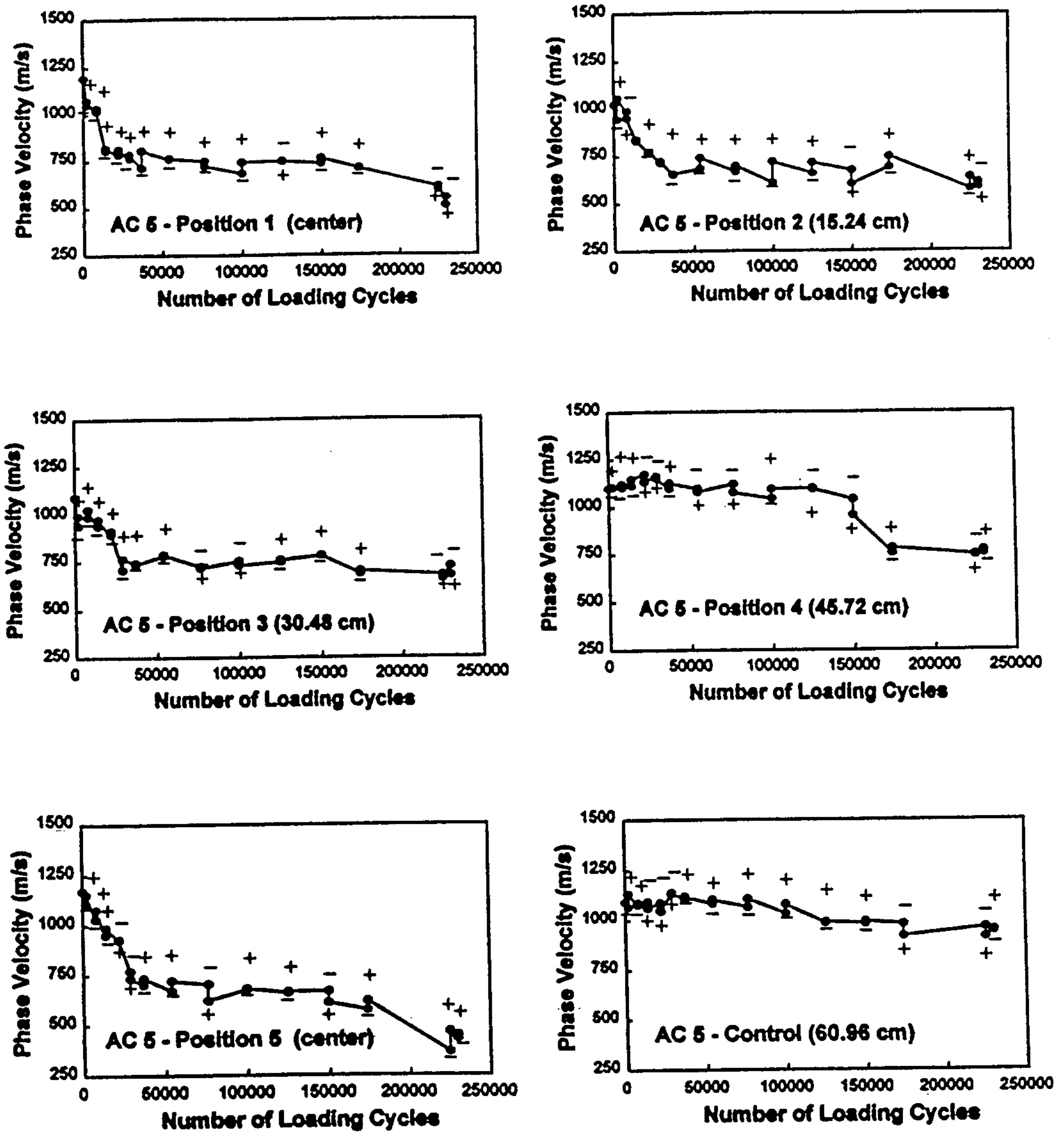

Figure 33. Changes in Phase Velocity During Fatigue Loading and Rest Periods (102-mm AC 5 Section).

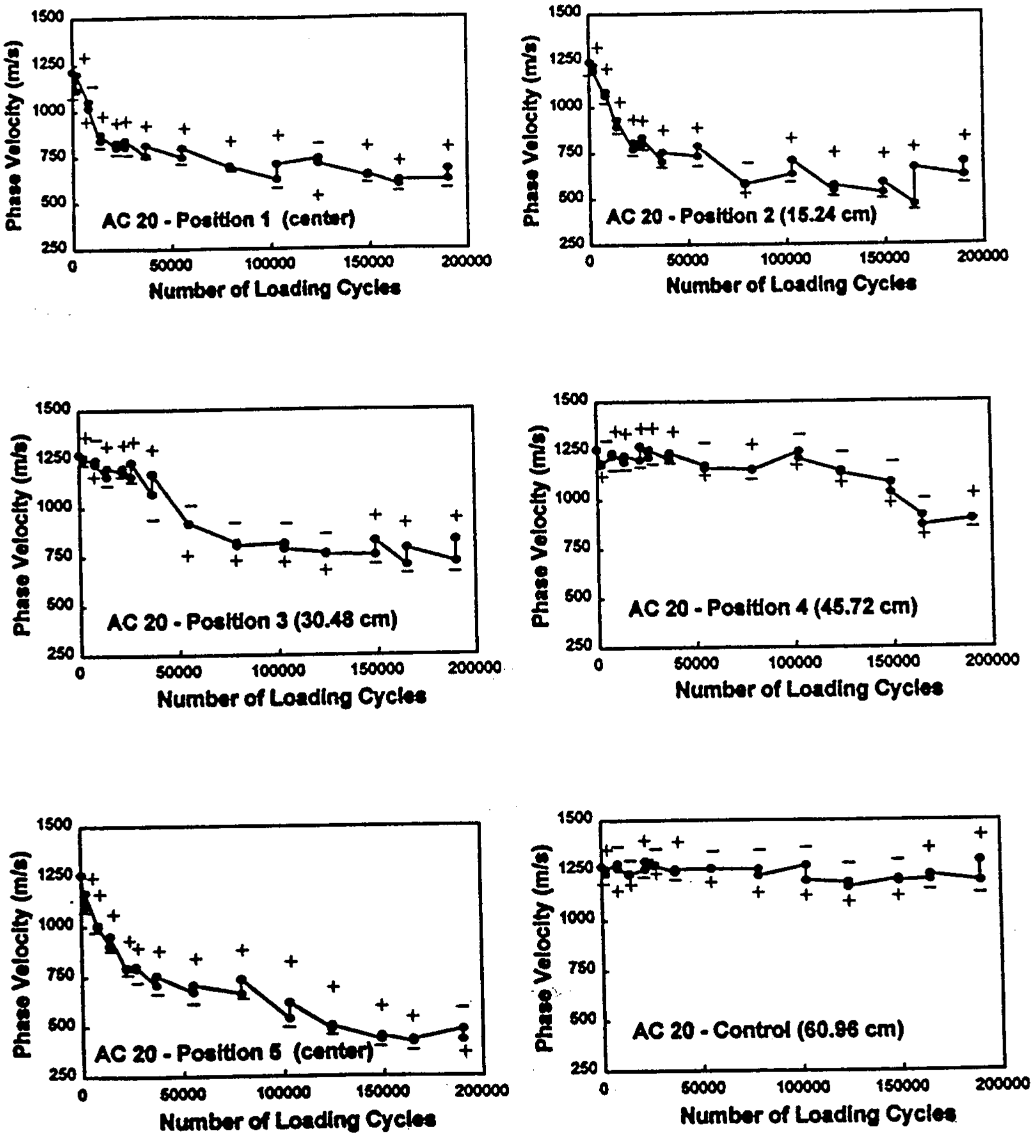

Figure 34. Changes in Phase Velocity During Fatigue Loading and Rest Periods (102-mm AC 20 Section).

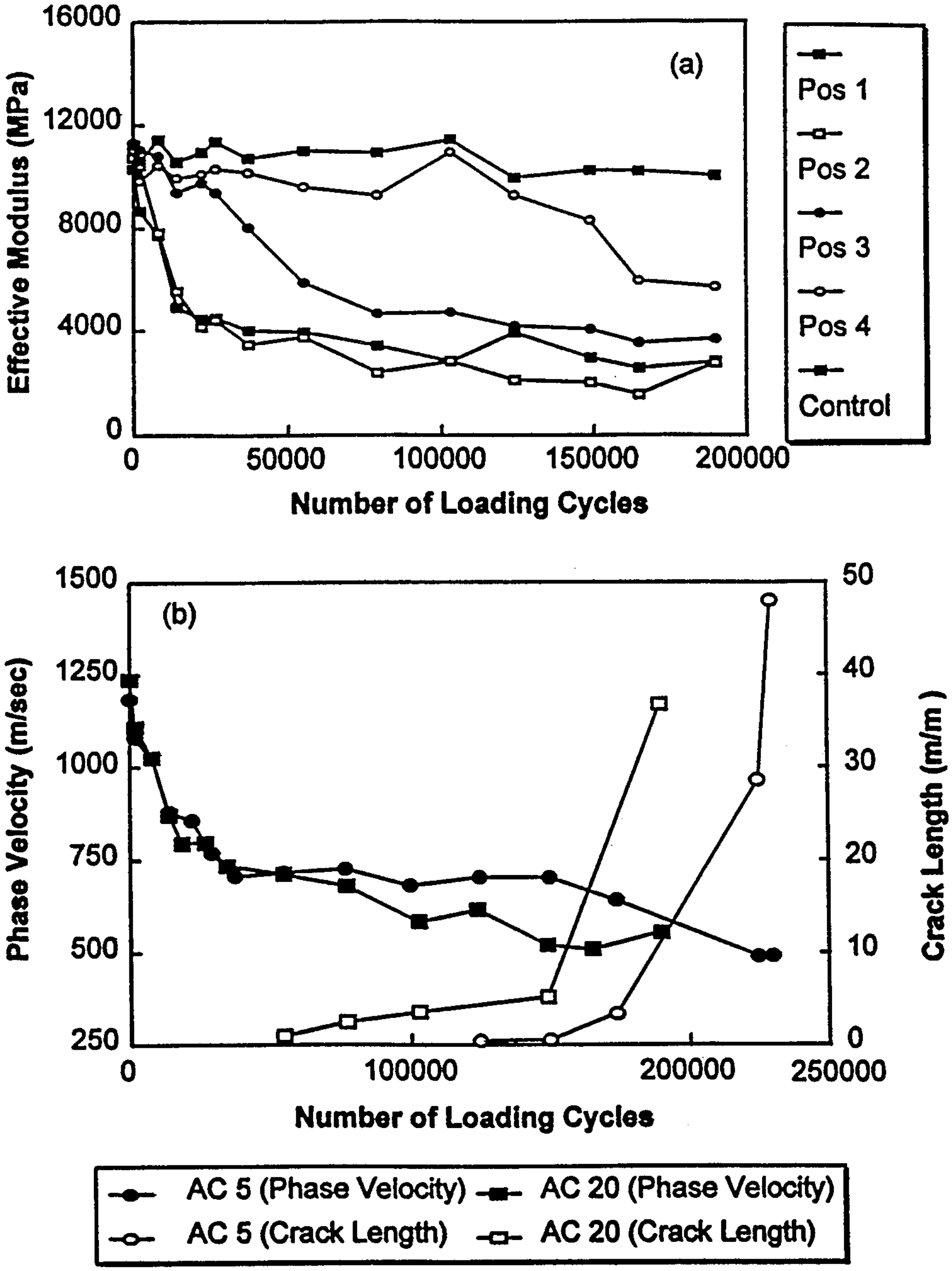

Figure 35. (a) Different Reduction of the Plastic Modulus at Different Positions in 102-mm AC 20 Pavement; and (b) Changes in Phase Velocity and Crack Length During Fatigue Lives of 102-mm Pavements.

A similar behavior can be observed from asphalt concrete specimens subjected to the laboratory indirect tensile or beam flexural fatigue tests. Figure 36 shows a typical trend between the flexural stiffness and number of loading cycles obtained from third-point-load beam flexural fatigue test (Sias, 1996). During these tests, most of the fatigue life and the flexural stiffness of an asphalt concrete specimen are consumed without any visible cracks on the specimen surface. Once some hairline cracks are observed on the surface, they propagate and coalesce quickly to develop major cracks that lead to failure. Since microcracks in the specimen inevitably precede any visible cracks, it is reasonable to attribute the early reduction of stiffness to degradation of asphalt concrete due to microcrack initiation, propagation, and densification.

In Appendix A, Figures A.1 and A.2 present the surface wave speed change at each position as a function of the loading passes applied to the 204-mm-thick AC 5 and AC 20 sections, respectively. Figures A.3 (a) and (b) show the effective modulus versus <u>actual</u> number of loading cycles applied to the different positions after accounting for the distribution of wheel passes using the probability density function. The damage caused by actual number of loading applied to Position 2 was higher than that in Position 1. Figures A.4 (a) and (b) show a similar trend in 204-mm sections, although the trend is not as obvious as in 102-mm sections.

Microdamage Healing of Asphalt Concrete

Effects of rest period on the phase velocity and therefore the elastic modulus can be investigated by simply checking the positions of the + symbols in relation to the - symbols in Figures 33 and 34. In most cases, except Position 4 and Control which are on the edge of the wheel path, and outside of the wheel path, respectively, the phase velocity increased after the 24-hour rest period.

There are several reasons that can be attributed to this trend. The first is the relaxation of the material due to its inherent viscoelastic nature. During the rest periods, the deformation induced in asphalt concrete from loading relaxes, and the structure of asphalt concrete changes, which can cause the change in the phase velocity. The second possible reason is the steric hardening of asphalt binder due to molecular restructuring during rest periods. The third reason for the increase in the elastic modulus during rest periods is the healing of microcracks, which is a well-proven phenomenon in polymer engineering. Determining how much of the beneficial effects of rest periods are contributed from each of these factors is an extremely difficult problem, if not impossible. Instead, all the beneficial effects of rest periods are included under the term of "microdamage healing" for convenience.

A very similar trend has been observed from the beam flexural fatigue test with 24-hour rest periods (Sias, 1996). As shown in Figure 36, the introduction of the rest periods increased the flexural stiffness and shifted the stiffness versus number of loading cycles curve toward the longer fatigue cycles, resulting in the longer fatigue life.

In order to compare the amount of healing at different positions, the healing index is defined as:

$$Healing\ Index(\%) = \frac{V_{after} - V_{before}}{V_{before}} x100 \tag{22}$$

where V_{before} = phase velocity after completion of each loading group, and
V_{after} = phase velocity after a 24-hour rest period.

Figure 37 shows the healing index in each test position for all the pavement sections. It is noticeable regardless of the pavement type that a larger offset of test location from the center of the wheel path (i.e., the position with a smaller number of loading applications and less damage) has a smaller healing index, except Position 2, which is located under the edge of the tire when the tire is positioned in the center of the wheel path. This trend suggests that more fatigue damage results in a greater magnitude of microdamage healing. Because the load was normal distribution, the probability that the wheel is on each test location is as follows:

Center (Positions 1 and 5) : 0.6102
15.24 cm (6 in) (Position 2) : 0.4564
30.48 cm (12 in) (Position 3) : 0.1898
45.72 cm (18 in) (Position 4) : 0.0436

The highest number of loading was applied on Position 1. Compared with Position 1, about 74% of loading is applied on Position 2. However, the reduction of the phase velocity was slightly greater in Position 2 than in Position 1. Recognizing that the type of damage in Position 2 is mostly due to shear stresses, this finding seems to indicate that the fatigue damage is more pronounced under the tire wall (due to shear stresses) than at the center of the wheel path (due to tensile stresses at the bottom of the AC layer). This can be explained by considering different fracture modes prevalent in the two locations. At the center of the wheel path, the opening mode of fracture prevails. Under the tire wall, however, all three fracture modes (opening, shearing, and tearing modes) occur, which would result in greater fatigue damage. These fracture modes and the locations are shown in Figures 38 and 39.

Another important observation to be made in Figure 37 is that the healing index is the highest in Position 2. Since the healing index is determined by normalizing the increase in the elastic modulus due to a rest period by the elastic modulus before the rest, the test locations with more fatigue damage yield greater healing index values in Figure 37.

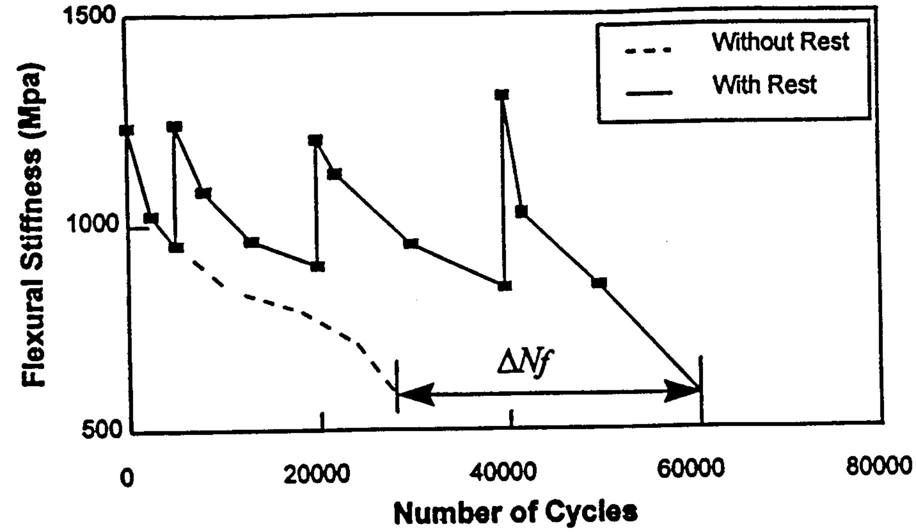

Figure 36. Changes in Flexural Stiffness During Fatigue Life of Asphalt Concrete.

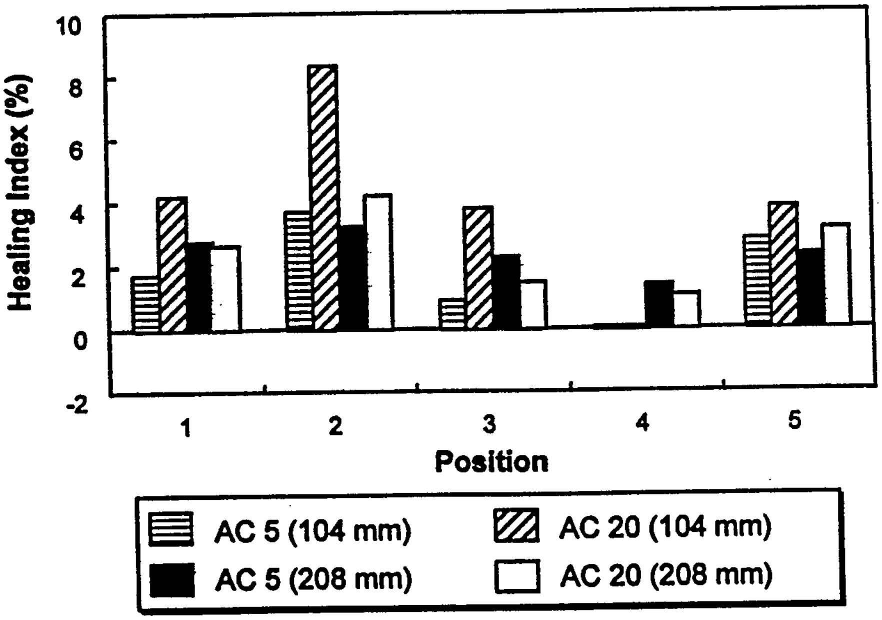

Figure 37. Healing Indices of Different Test Locations.

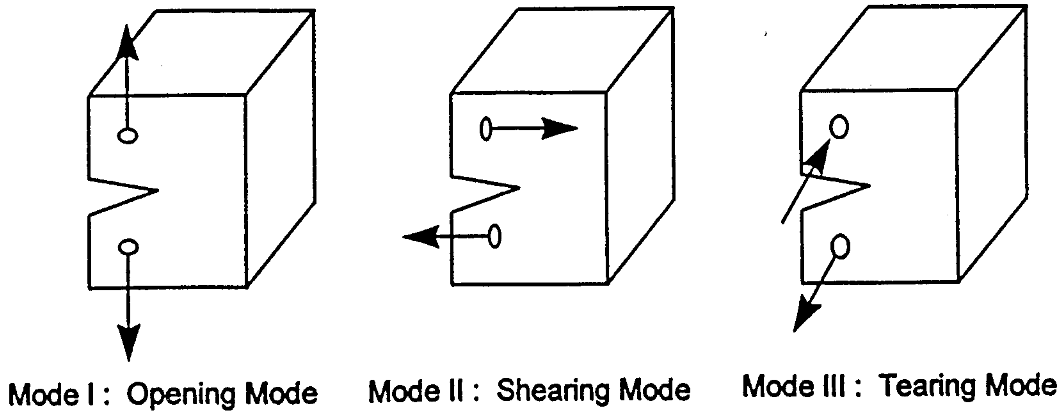

Figure 38. Fracture Modes.

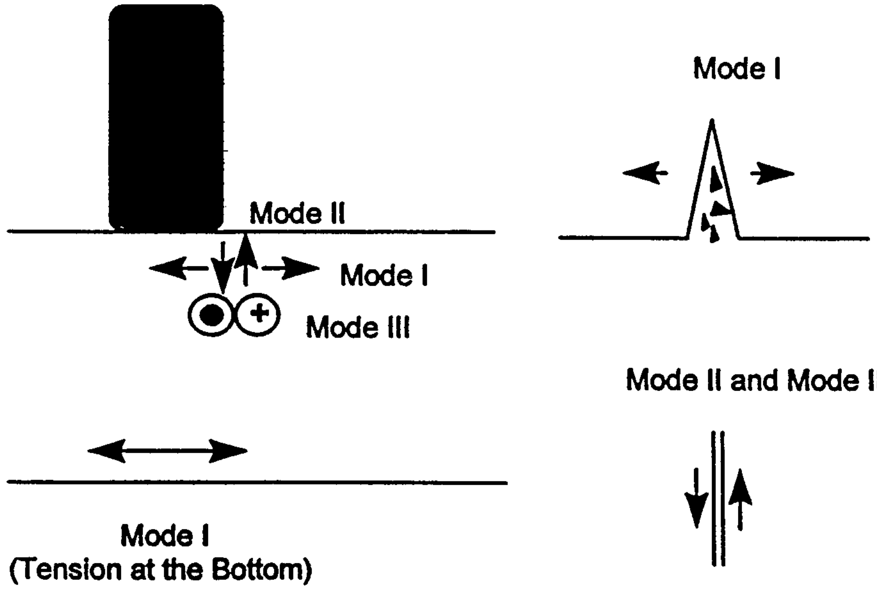

Figure 39. Fracture Modes Under the Center of the Wheel Path and Under the Tire Edge.

Therefore, the greatest fatigue damage in Position 2 results in the highest healing index value. Also, it is reasonable to speculate that microcracks in Position 2 that have been developed in the shear and tearing modes have better chances of maintaining closer contacts between crack surfaces and thus a greater amount of healing than the cracks developed under the opening mode.

In general, the AC 20 pavements displayed higher healing indices than the AC 5 pavements. It needs to be noted that the rest period used in these experiments was 24 hours long. Asphalt mixtures with higher viscosity may take a longer time to heal completely because of lower mobility, but may exhibit greater strength regain due to higher stiffness when healed completely.

Comparison of the Moduli From the Direct Approach and the Inversion Approach

Since the direct approach used in calculating the elastic modulus is still approximate in nature, the results from the direct approach are compared in this section against more accurate results from the inversion. Hereinafter, the elastic modulus calculated from the direct approach is referred to as "effective" elastic modulus to distinguish from the elastic modulus determined from the inversion method.

The inversion procedure allows the backcalculation of the shear wave velocity profile from the dispersion curve using an appropriate forward numerical model for the multilayered system. A theoretical dispersion curve is calculated from an assumed shear wave velocity profile by using the forward model. The theoretical dispersion curve is then compared with the experimental dispersion curve measured from the SASW test. The assumed shear wave velocities and the thicknesses of the layers in the model are adjusted until a satisfactory agreement between the two dispersion curves is obtained.

In this study, the numerical forward model based on Hankel transform described earlier and the trial-and-error procedure for matching the theoretical and the experimental dispersion curves was employed to process some data points from the 102-mm pavements. Figure 40 shows the matched theoretical and experimental dispersion curves of the AC 5 pavement at three different damage conditions: the pre-loading state, after 120,000 loading applications, and near the failure. Figure 40 displays the reduction of the elastic moduli of the asphalt layers calculated from the inversion procedure as fatigue damage grows.

The percentage difference of the elastic moduli determined from the direct approach and from the inversion was below 4% for all the cases investigated in this study. Therefore, it is concluded that the direct approach and the test setup used in this study are appropriate for the evaluation of surface layer properties.

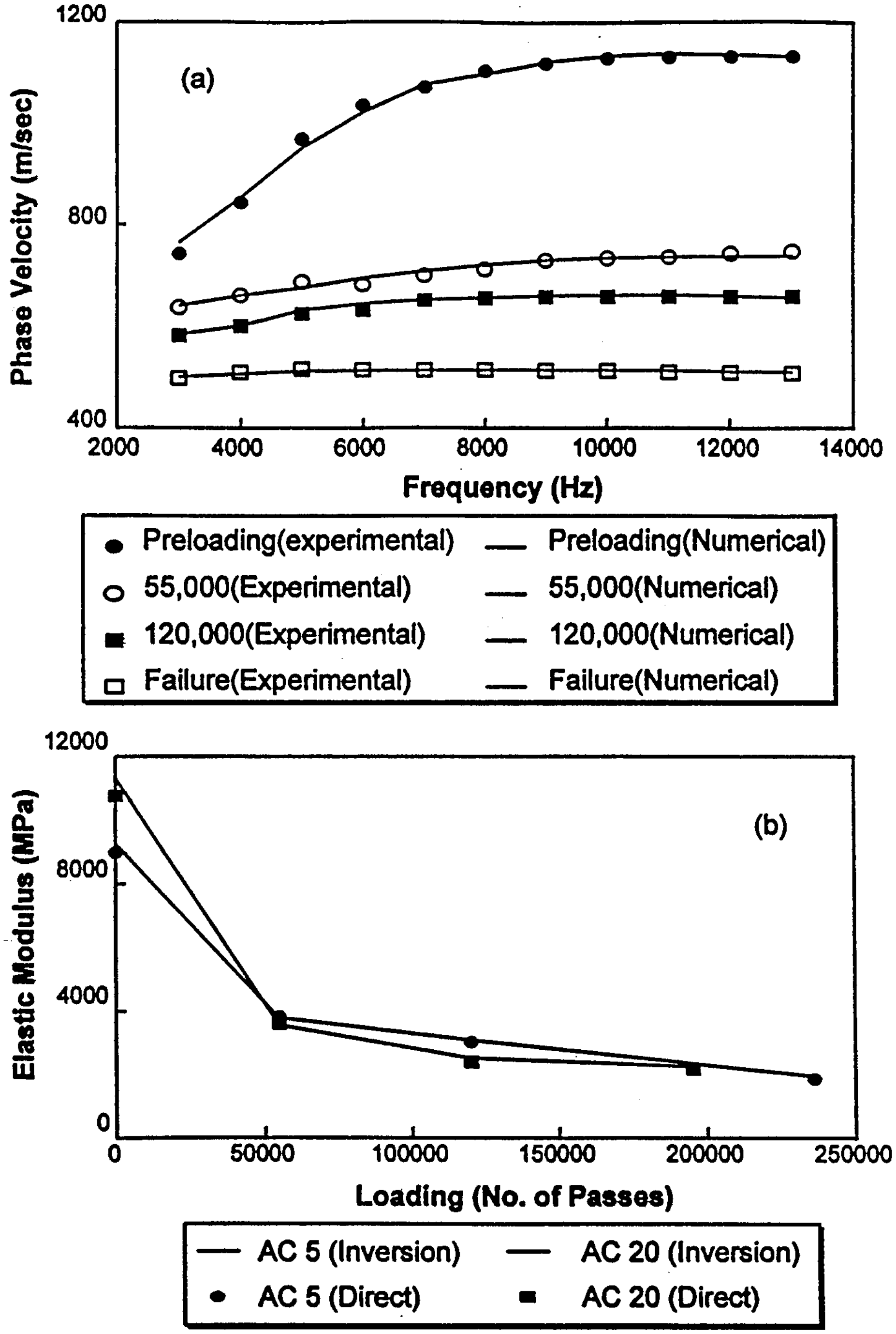

Figure 40. (a) Agreement Between Experimental and Numerical Dispersion Curves in 3 Loading Stages of AC 5 102-mm Pavements; and (b) Elastic Moduli Obtained by the Direct and the Inversion Approaches.

PART II: EVALUATION OF PAVEMENT SECTIONS IN MINNESOTA RESEARCH PROJECT (MN/ROAD)

The Minnesota Road Research Project is a vast pavement research and analysis facility 40 miles northwest of Minneapolis, Minnesota. The site consists of two test roads, which contain a total of 40 different 500-foot pavement test sections as shown in Figure 41. Several parameters are varied in each section, such as layer thicknesses, type of pavement structure, asphalt binder, base layers, and performance period. There are 4,572 sensors of 17 types embedded in the test sections that continuously measure and send data to the Mn/Road computer system. These data can be accessed by researchers all over the world by use of the Internet.

A 3.5-mile Mainline roadway (part of Interstate-94) contains 23 test sections and is loaded with freeway traffic. The remaining sections are located in a 2.5-mile loop called the Low Volume Road and are loaded with a calibrated truck. Since the Mainline is loaded with interstate traffic, the data collected represent actual highway traffic loading and volume conditions. The Low Volume Road is loaded with a controlled truck weight and volume to simulate conditions on rural roads.

Selection of Test Sections

Seven of the 40 pavement test sections at Mn/Road were selected for testing during this research. The selections were based on varying the thicknesses of the asphalt and base layers, and the design life of the pavements. It was desirable to test a wide range of asphalt layer thicknesses since the surface layer is where microcrack growth occurs and its thickness is a primary variable in pavement design. In addition, sections with a shorter design life were more practical due to the desire to obtain conclusive results within the limited project length.

The sections chosen were F3 and F4 on the Mainline, and Cells 25, 26, 27, 29, and 31 on the Low Volume Road. The locations of these test sections are shown hatched on the plan view of all the sections in Figure 41. All the sections are bituminous test sections. The Mainline sections both have a 5-year service life with layer properties as shown in Figure 42. The Low Volume Road sections are all 3-year sections with layer properties also shown in Figure 21. The asphalt cement used in all seven sections is graded as Pen 120/150. Class 6 aggregate is 100% crushed granite and is the highest quality aggregate used in the Mn/Road test sections. Classes 5, 4, and 3 are each reduced in quality successively.

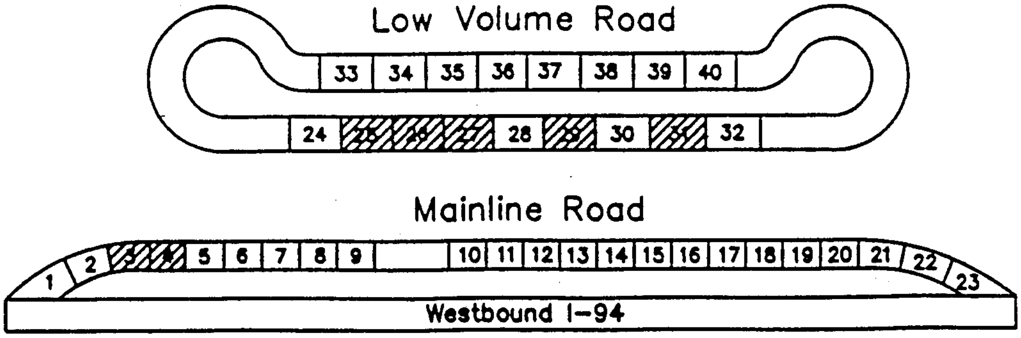

Figure 41. Mn/Road Test Pavement Sections.

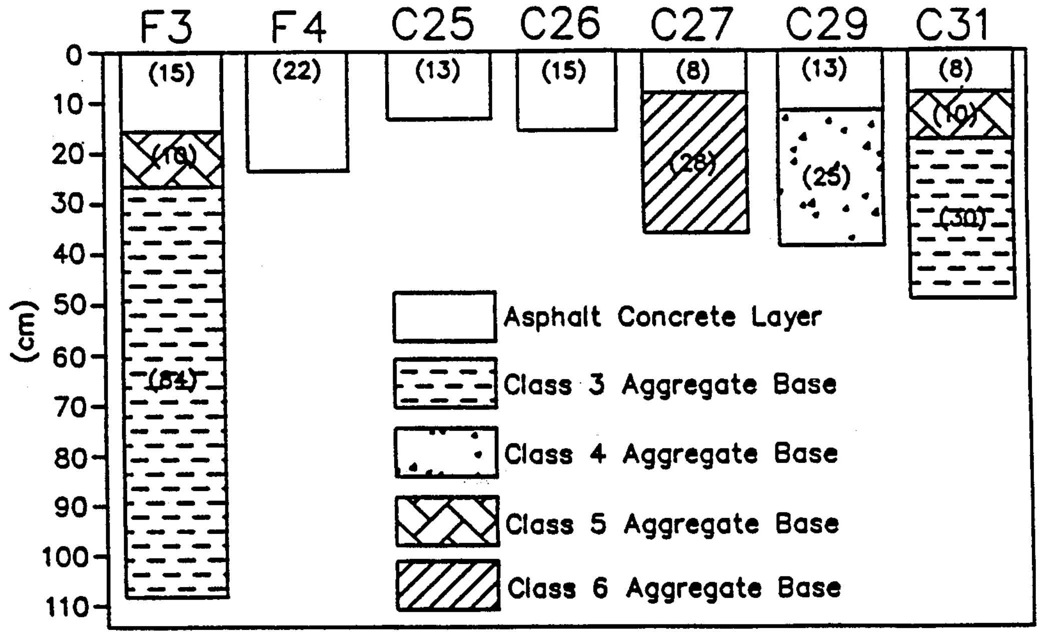

Figure 42. Mn/Road Test Section Properties.

Testing at Mn/Road

Nine trips to Mn/Road for surface wave testing were completed. Testing at Mn/Road occurred over 5-7 days for each trip. The surface wave test setup began with locating the areas for the testing arrays. Two spots for each cell were selected in the center of the far right wheelpath. In addition, during the last two trips to Mn/Road (August 96 and October 96), a centerline location was also tested for all cells. This was marked by measuring the width of the lane and placing the array in the center. Care was taken in selecting testing locations that were free of thermal cracking and loose debris.

After all the sections of either road were set up and tested once, testing followed at approximately 1 hour intervals. Testing consisted of recording three impacts for each test array. When the impact device was also used, an additional three impacts were recorded for each testing spot. It often took more than three impacts to obtain good signals for each test. This was due to slight variations in the pavement surface and energy source. If the plate was not held firm enough or it was placed on an unstable aggregate, the resulting signal might contain unwanted high frequency noise. These signals were not recorded and the test was performed again until a reasonable signal was obtained. Sometimes it was necessary to slightly move the impact location due to an unstable area causing erratic signals. It was also occasionally necessary to check the accelerometers to be sure the magnetic contact was free of debris and that the bases of the accelerometers were screwed on tightly.

Temperature Data Acquisition

The collection of temperatures was performed by use of implanted thermocouples in the Mn/Road pavement sections. Temperatures at Mn/Road are measured continuously by the Mn/Road computer system, usually at 15 minute intervals. An Mn/Road engineer gathered the temperature data for the stress wave testing times and sent it to North Carolina State University via e-mail after each trip. These temperature files consisted of data from the thermocouples, which were located at various depths in the surface layer. A study was conducted in order to determine the best "effective" surface layer temperature for use in analysis. It was concluded that the mid-depth temperature of the asphalt concrete layer provided a good "effective" temperature for the surface layer. The asphalt layer mid-depth temperatures (in Celcius) were obtained by linear interpolation between the thermocouples in the pavement and the times of the temperature readings (Katzke, 1997).

Elastic Modulus Calculation

Phase velocities from the Short Kernel Method were used to compute the elastic modulus for the asphalt concrete sections. A relation between Poisson's ratio and temperature for asphalt concrete was developed by Whitmoyer (1993) by equating elastic and shear moduli from Impact Resonance tests of asphalt concrete cores in the longitudinal and torsional modes at varied temperatures. Using the mid-depth temperatures in the Mn/Road pavements, Poisson's ratio was calculated using the relation below (Whitmoyer, 1993):

$$\nu = 0.3 + 0.07\left(\frac{T-20}{10}\right) \tag{23}$$

A numerical procedure was then used to compute the value of α, the ratio of the shear wave velocity to the Rayleigh wave velocity. This procedure is based on the Newton-Raphson iteration formula used in conjunction with a Taylor's series (Bajpai et al., 1977). The iterative formula is as follows:

$$\alpha_{new} = \frac{\alpha_{old} - f(\alpha)}{f'(\alpha)} \tag{24}$$

where:
α_{new} = the new value in the iteration,
α_{old} = the previous value in the iteration, and
$f(\alpha)$ = equation 14.

After the α value has been determined, the shear modulus (G) is computed using equation 16. The elastic modulus is then determined using equation 17.

Rate-Dependence and the "Effective" Modulus

Although the wavespeed and elastic modulus are directly related as described in the previous section, it is evident that the modulus obtained from stress wave testing is not the same as the conventional elastic modulus from static lab testing. This is due to the vast difference in the frequency of loading for each test. The approximate loading frequency for the surface wave test is 10 KHz based on the resonant frequency of the waveform. Typical loading rates for laboratory complex modulus tests are between 1 and 16 Hz.

The rate dependency of viscoelastic materials such as asphalt concrete causes a large difference between the modulus values obtained from the two tests (Daniel and Kim, 1997). In addition, the modulus from the surface wave test is computed using the phase velocity from the phase velocity using the SKM, as opposed to performing the inversion process to get the exact shear wave velocity. For these two reasons, the modulus value obtained from surface wave test will be referred to as the effective modulus.

The frequency dependence of the elastic modulus was shown by determining the modulus values from several tests of varying frequency. Modulus values for the F4 asphalt concrete section of Mn/Road were calculated using four testing methods. These methods were surface wave testing and FWD testing in the field, and impact resonance (ASTM C 215) and complex modulus testing (ASTM D3497-79) on cores from the pavement. The dominant frequencies for each test are 10 KHz for stress wave testing, 3500 Hz for impact resonance, 30 Hz for FWD testing, and 2.5 to 33 Hz for the complex modulus testing. These frequencies are based on the loading frequency for the impact resonance and complex modulus tests, or the dominant frequency of the waveform for the stress wave and FWD tests. The mid-depth temperature of the pavement during the field testing was about 13.5°C (56°F) and therefore the lab testing was also performed at this temperature.

For practical use, a modulus value comparable to those used in typical pavement design and analysis must be obtained. Figure 43 shows the relationship between the elastic moduli values computed from each test method at the corresponding frequencies. The relationship shown in Figure 43 is important because it provides a way to determine the modulus values at lower frequencies from surface wave testing. This converted modulus is thus equivalent to the traditional values used for pavement design and analysis. A method using the time-temperature superposition principle was developed for this conversion by Sias (1996).

Damage Growth Measurements at Mn/Road

Wavespeed and attenuation measurements of the surface wave signals were used to quantify the presence of damage in the Mn/Road asphalt concrete sections. It should be noted that the actual amount of damage in the Mn/Road sections is not known. Visual condition surveys and lab core tests were used to estimate the extent of damage, but only an approximation could be made.

Effective modulus values were computed from the wheelpath surface wave tests on all cells and trips to Mn/Road. The FFT magnitude plots revealed that the dominant frequency was approximately 10 KHz for all the tests. Therefore, the phase velocities were all computed at 10 KHz using the SKM and then the effective modulus was computed for each phase velocity. The values were plotted against the calculated mid-depth temperatures and are presented for Section F4 on Mainline and Cell 31 on the Low Volume Road in Figures 44 and 45. The remaining sections are presented in Figures A.5 through A.9 in Appendix A. In these graphs, the Mainline sections show very little deviation from the pretraffic data. However, the Low Volume Road data show a significant increase in effective modulus during the testing period.

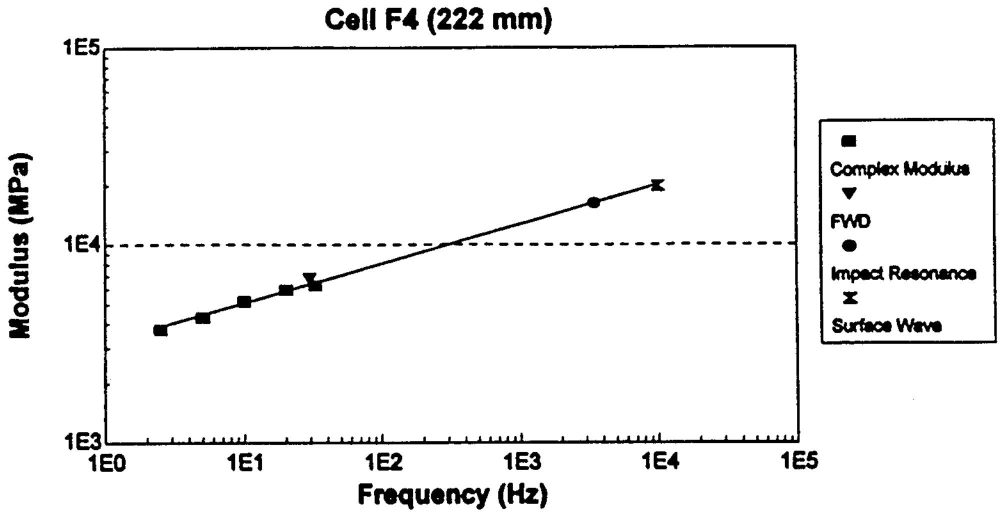

Figure 43. Frequency Dependence of Elastic Modulus.

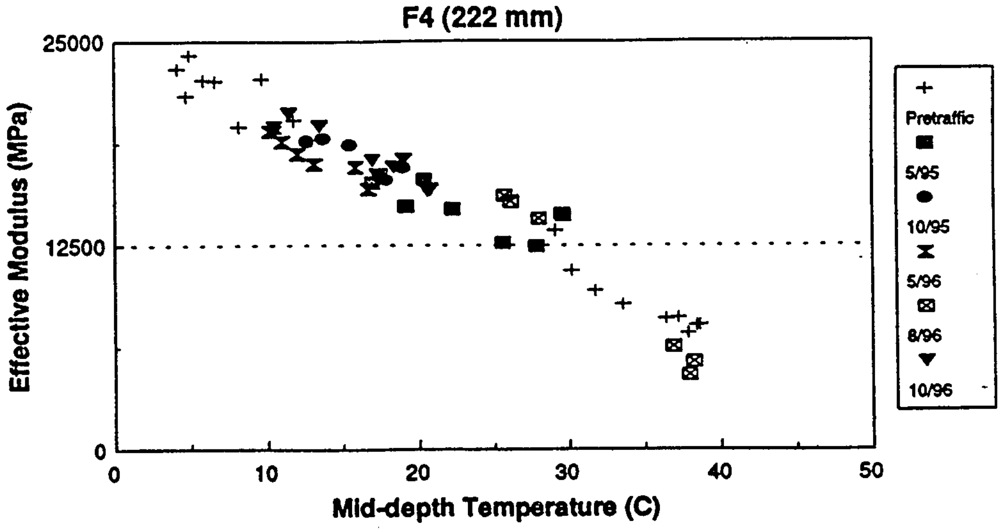

Figure 44. Effective Moduli of Cell F4.

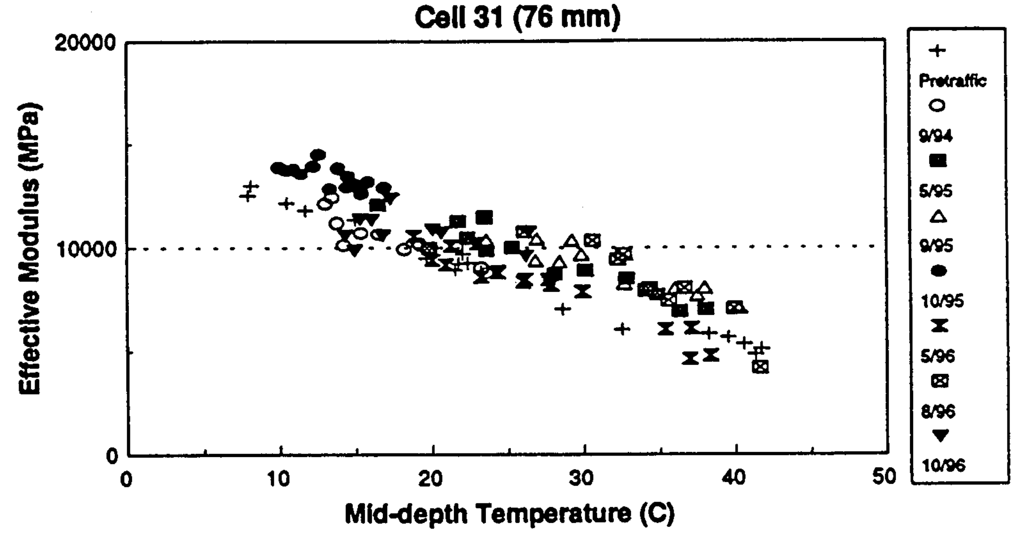

Figure 45. Effective Moduli of Cell 31.

Temperature Effect and Correction

The effect of temperature on the effective modulus is evident in the effective modulus versus temperature plots. Clearly a higher temperature reduces the effective modulus as shown in all seven plots. It should be noted that at the extreme high temperatures there is significantly more variability within each trip. This occurs because the high temperatures severely attenuate the high frequencies of the stress wave signals and reduce the quality of the SKM function. Therefore, the accuracy of the wavespeed calculation is reduced and the obtained wavespeeds are not as reliable as at lower temperatures.

The variation in the effective modulus graphs due to temperature makes it difficult to draw conclusive results. It is desirable to temperature correct all the phase velocities to one reference temperature. This can be performed by fitting a curve to the pretraffic wavespeed data and then using the curve to perform the correction to a reference temperature. Since the pretraffic data was obtained prior to any loading on the pavements, the change in modulus is purely due to the effect of temperature. This temperature correction was performed for all data at a reference temperature of 20°C (68°F) to be consistent with the ALF data.

All the pretraffic data (October 1993 and May 1994) were plotted against the mid-depth temperatures as shown in Figures A.10 through A.16 in Appendix A. These data covered a wide range of temperatures so a proper curve fit was easily obtained. A cubic polynomial fit was applied to all the pretraffic data. The equation for each fit as a function of temperature was also determined for use in the correction procedure.

It is evident that the center portion of the curves are approximately linear, while the end regions may be curving toward an asymptotic value. This is particularly evident in Figures A.12 and A.16. The higher and lower temperature values may not be extreme enough to develop the curvature for the asymptotes in all cases. This S-shape characteristic of modulus versus temperature has also been shown by past work (Sias, 1996).

In order to correct all the phase velocities to a reference temperature, the correction factor must be determined for each value. The correction factor is the phase velocity at the reference temperature divided by the phase velocity from the polynomial fit at the temperature for each test. The reference phase velocity was determined by plugging the reference temperature (20°C) into the cubic polynomial fit equation. The correction factor was then computed for each phase velocity by dividing the reference phase velocity by the phase velocity determined from the curve fit at the temperature of the test.

Once the correction factor was determined for each test, the phase velocities were all multiplied by the corresponding correction factors to obtain the temperature-corrected phase velocities. The temperature-corrected apparent moduli were then computed from the new phase velocities using the procedure outlined previously. In this manner, all the apparent moduli could be compared without the effects of temperature present.

Damage Growth Using the Temperature-Corrected Effective Modulus

The corrected effective modulus values for each trip were all averaged and plotted as a function of the number of Equivalent Single Axle Load applications (ESALs). The plots for Section F4 and Cell 31 are shown in Figures 46 and 47. The other sections are presented in Figures A.17 through A.21 in Appendix A. The ESALs represent the amount of cumulative loading on the pavements. Therefore, these plots indicate the progress of damage in the sections from pretraffic until the last trip in October 1996.

Due to the high temperatures and poor quality of the signals obtained during the September 1995 and August 1996 trips, inaccurate wavespeeds with high variability were obtained. The temperature correction procedure overcompensated for these problems and caused the corrected effective modulus values to be abnormally high. These values were excluded from the temperature-corrected effective modulus graphs.

Results from Effective Modulus Versus ESAL Plots

It is difficult to draw absolute conclusions based on the damage growth plots in Figures 46, 47, and those in Appendix A. Although the data presented have been temperature corrected, a significant amount of scatter is still evident. The cause of this variability can be attributed to the nature of this experimental method and the factors discussed earlier. However, some general conclusions can be made by observing the overall trends in the graphs.

Mainline: The data from the Mainline sections are presented in Figures 46 and A.17. An increase in effective modulus is evident on these sections after they were opened to traffic. This increase can be due to densification of the asphalt concrete, which is known to occur in the first few years after a pavement is loaded with traffic.

After the initial increase, the effective moduli appear to decrease to some extent, indicating that microcrack damage is starting to reduce the stiffness of the asphalt layer. This decrease is less evident on section F4, perhaps due to the thicker asphalt layer and higher resistance to cracking. However, the trends in Figures 46 and A.17 show that significant microcrack damage and reduction of effective modulus has not taken place. This conclusion is in agreement with the actual visual condition survey of the pavement. Between 5 and 10 mm of rutting has occurred, but fatigue cracking is not present in either section and overall the sections appeared to be in good condition at the end of the testing period. In addition, F3 and F4 were designed to have a 5-year service life and this research only studied the first three years. It appears that significant damage is not present in the Mainline sections.

Low Volume Road: The Low Volume Road sections in Figures 47 and A.18 through A.21 show trends similar to the mainline sections. There is an increase in effective modulus for all five sections, although the slope of the increase varies for each section. It is interesting to note that the two thinnest surface layer sections (Cell 27 and Cell 31) both have the steepest initial increase in effective modulus. The other three sections all have thicker surface layers and a more gradual increase in effective modulus. This should be expected because it would take longer to densify a thicker section than a thinner one. The initial increase in effective modulus was verified by lab diametral fatigue tests of cores from Cells 27 and 31 as shown in Figure 48.

After the increase in effective modulus, a slight decrease is evident in all five cells. This decrease is slight and only begins at the last one or two points for Cells 25 through 29. Cell 31 is the only cell with a significant decrease in effective modulus during the testing period. This is reasonable because Cell 31 is one of the thin surface layer sections. It is not clear why Cell 27, the other thinnest layer, does not also show this significant

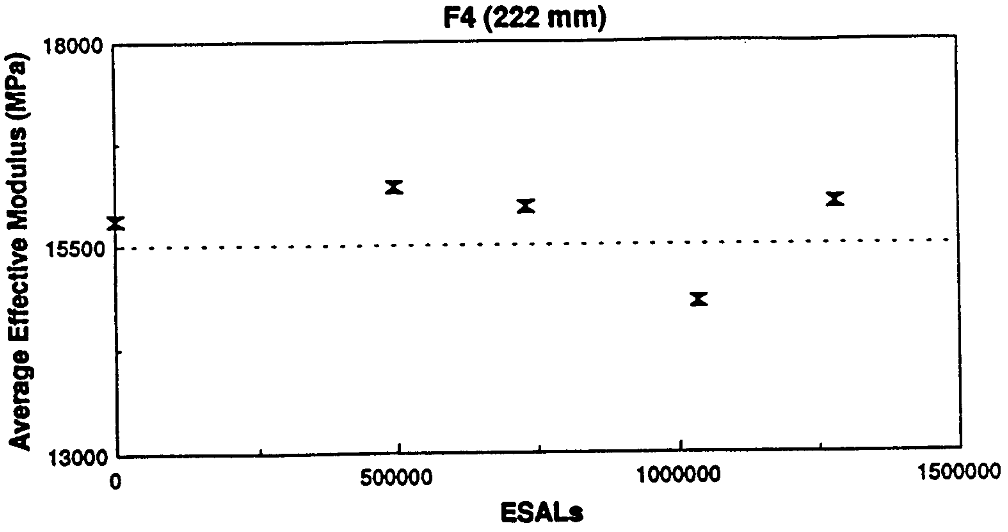

Figure 46. Cell F4 Damage Growth Using Corrected Effective Moduli.

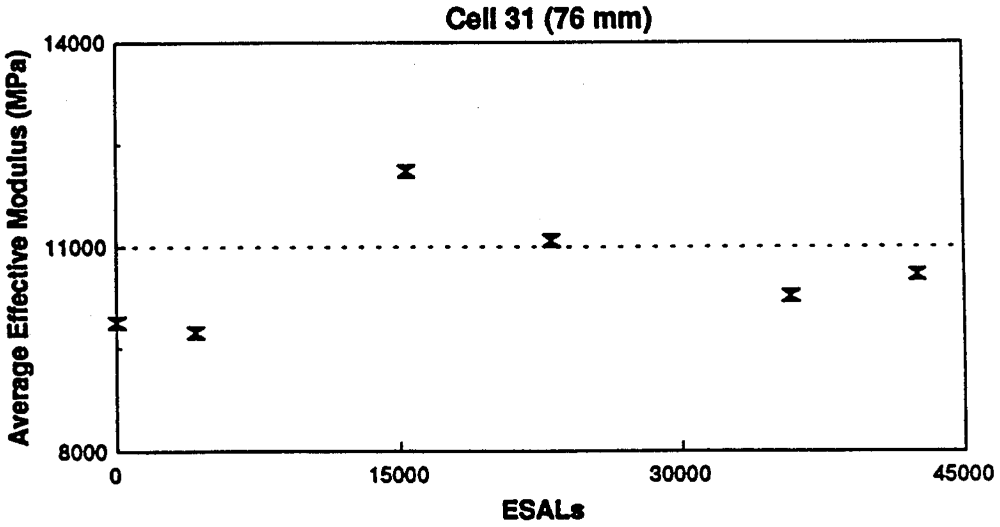

Figure 47. Cell 31 Damage Growth Using Corrected Effective Moduli.

decrease in effective modulus. The reason may pertain to the different base layers for each section. Cell 27 has the highest quality base, while Cell 31 has lower quality base layers.

The results from the diametral fatigue tests in Figure 48 also show a decrease in strength following the increase from densification. This decrease is larger for Cell 31, which agrees with the surface wave effective modulus results.

The Low Volume Road sections were all designed for a 3-year service life. It was expected that a more significant decrease in effective modulus would be observed during this research. There are several possible reasons why the results do not show this decrease as expected. The nature of the truck loading allows rest periods of 6 minutes between each cycle during business hours Monday through Friday. Additionally, the pavement rests through the night from 5pm until 8am the next morning, and all day and night on Saturday and Sunday. Rest periods between fatigue loading on asphalt concrete can heal the asphalt concrete microcracks and restore its strength. These beneficial effects have been proved by several researchers (Kim et al., 1994, Sias, 1996, Kim and Kim, 1996) and will be discussed later in this report. If these beneficial effects take place on the Low Volume Road sections during the rest periods, the pavements will have a longer service life than expected. Another factor to be considered is that all the pavements were designed conservatively due to the experimental nature of the test facility. The actual service life of the pavements is most likely longer than what is specified.

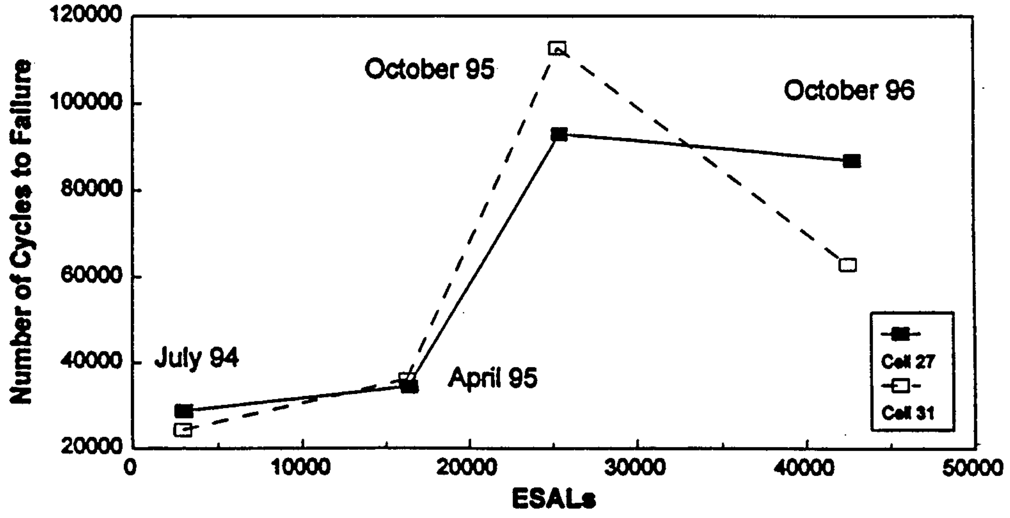

Figure 48. Diametral Fatigue Test of Mn/Road Cores.

Attenuation Measurements at Mn/Road

Attenuation of stress waves has recently become a popular method for the evaluation of damage in a material (Kalinski, 1994; Halabe et al., 1996). The loss of energy as a stress wave propagates is present in all materials due to material and radiation damping as discussed in Appendix C. However, this attenuation may be greatly magnified if the material is damaged in some way.

The use of frequency domain analysis provides a much more sensitive measure of attenuation than time domain analysis (Halabe et al., 1996). This is because the signal obtained in the time domain is composed of many sinusoidal components of varying magnitudes. By using the frequency domain, the magnitudes of the individual frequency components can be studied in detail.

Another strength of using frequency domain analysis is that unwanted frequencies can be easily filtered out. Due to the dispersive nature of the Rayleigh wave, the lower frequency components found in the signals represent information from layers below the asphalt layer. During this research, only information from the surface layer was desired. Therefore it is convenient to analyze these signals in the frequency domain so that the frequencies corresponding to the lower layers can be neglected.

In order to quantify attenuation, a parameter must be used that will represent the loss of energy as the wave propagates. Halabe et al. (1996) performed ultrasonic tests on various wood members with and without defects. Analysis in the time and frequency domains was used to quantify the attenuation due to damage in the members. The use of velocity measurements in the time domain did not provide the necessary sensitivity to identify defects in wood members. However, in the frequency domain the central frequency and the area under the FFT plot were both good indicators of defective members.

Although the central frequency can be used to show a loss of higher frequencies due to damage, it is often ineffective in a layered system due to low frequency effects from base layers. Therefore, the area under the FFT plot was chosen to quantify the effects of damage on attenuation in this study.

The area under the FFT magnitude plot represents the amount of energy present in the signal. By measuring the loss of area under the FFT plot from one channel to another, the attenuation can be accurately quantified. Also, since each impact contained a different amount of energy, the ratio of the area under the first channel to that of another channel was used. Assuming the percentage of energy lost due to attenuation will remain the same for all impacts; the variability in impact magnitude can be minimized because the ratio of the areas from two channels will remain relatively constant for each replicate test.

The ratio of areas under the FFT plots can provide an effective measure of signal attenuation. Throughout this research, the area of channel one over the area of channel two was used as an attenuation measure. A larger amount of attenuation will produce a higher ratio since channel two will have much less energy (or FFT area) than channel one.

Although the temperature varies with each test, the temperature does not have a significant effect on the attenuation until temperatures approximately greater than 32°C. The attenuation ratios during this research were all averaged if the temperature was below 32°C so that an overall estimate of the parameter could be obtained.

For use in FFT attenuation analysis, a computer program was written using MATLAB to plot the raw data and FFT magnitude graphs for surface wave data. This program is presented in Katzke (1997). The program will plot the raw signal and FFT graphs for nine tests on each page. It provided a convenient way to view many test results at once and qualitatively determine the amount of attenuation present in the signals.

Validation

A validation study was performed on several specimens to verify the use of the FFT area ratio as a measure of attenuation. Testing was performed on a portland cement concrete slab, a timber beam, and an asphalt concrete pavement (different location than Mn/Road). Results from these tests showed that the attenuation ratio was an effective measure of damage in the various specimens. An increase in damage present within each material caused an increase in attenuation ratio (Katzke, 1997).

Attenuation Ratio for Damage Assessment of Mn/Road Sections

The attenuation ratio was used to assess the condition of the Mn/Road pavement sections from surface wave tests using the 8 oz. hammer. Comparing the attenuation ratio at the wheelpath and centerline locations can provide an indication of the amount of damage present in the pavements. A higher difference in the attenuation ratios at the wheelpath and centerline locations would signify a larger amount of damage in the pavement.

The attenuation ratio was computed for centerline and wheelpath locations from the October 1996 trip using a frequency range of 5-20 KHz. The frequencies below 5 KHz were filtered out so that the effects from base layers did not affect the attenuation ratio calculation. The ratio values for wheelpath and centerline were averaged for each section and plotted as shown in Figure 49.

All the temperatures from the October 1996 trip were below 24°C and the temperature was assumed to have no effect on the attenuation. Thus, it was reasonable to average all the attenuation ratio values for each cell in order to obtain an overall attenuation value.

Mainline: The Mainline sections show very little difference in attenuation at the wheelpath and centerline locations, indicating that damage is not present or is negligible in these sections. The wavespeed-modulus analysis presented earlier shows that F3 has a sizable decrease in modulus after the initial increase. It was expected that this result would be reflected in a higher attenuation ratio at the wheelpath location. One possible explanation for this is that the Mainline sections are open to actual highway traffic and the centerline location is trafficked to some extent.

Low Volume Road: The most significant increase in the attenuation ratio from centerline to wheelpath occurs on Cell 31 as shown in Figure 49. The average attenuation ratio at the wheelpath is more than double the value at the centerline location. This increase indicates a significant amount of damage present at the wheelpath location. There is also very little variability in the actual attenuation ratio data before it is averaged as shown in Figure 50. The actual data from the other sections show more variability than Cell 31. Cell 27 has a similar increase in the attenuation ratio, although not to the extent and consistency as Cell 31. All other cells do not show this increase in attenuation ratio from centerline to wheelpath. These results are in agreement with those from the effective modulus study.

A strange phenomenon is evident in Cell 25 as shown in Figure 49. The centerline attenuation ratio is much higher than expected. A reasonable explanation for this is that a crack or void was present in the asphalt layer between the first and second sensor locations. This defect would significantly reduce the signal energy, causing the attenuation ratio to be excessively high. Unfortunately only one centerline location was tested for each cell so this hypothesis cannot be checked. However, results from both the 8 oz. hammer and spring loaded device for all tests during the October 1996 trip show this effect in Cell 25.

Damage Growth Using Attenuation

Based on the effective modulus graphs and the centerline versus wheelpath attenuation study, it is reasonable to conclude that a significant amount of damage has developed only in Cell 31. Now it is desirable to monitor the progress of damage as it develops.

The attenuation ratio was computed for the testing on Cell 31 from all trips. These values were then averaged and are plotted in Figure 51. The high temperatures during the August 1995 and September 1996 trips increased the attenuation and were therefore not included in this study. Figure 51 clearly shows an increasing trend in the attenuation ratio with each year verifying that the attenuation ratio can be used to monitor damage growth in asphalt concrete pavements.

An overall seasonal temperature effect is present in the attenuation results shown in Figure 51. The testing performed during the October trips was at much lower temperatures than that during the May trips. It would be expected that the October trip attenuation values are higher, creating a more linear increasing trend, but the colder temperatures decreased the attenuation values. The opposite result may have occurred during the May trips. This overall seasonal effect indicates that there is some temperature dependence of attenuation, but within each trip it was not found that the temperature affected the attenuation ratio below 32°C.

The increasing attenuation ratio shown in Figure 51 was not found for any other Mn/Road pavement section. A significant amount of variability was present in much of the data. Although the attenuation study shows promise for use as a measure of damage growth, it is clear that the extreme sensitivity of the frequency analysis can cause problems in the accuracy of the results. Development of better impact devices or more consistent testing methods may help eliminate much of the variability present in the data.

Mn/Road Condition Surveys

Condition surveys were performed periodically by Mn/Road employees to record the physical condition of the Mn/Road sections. Crack maps and rut depths were obtained for several dates throughout the testing period. The crack maps indicated no fatigue cracking on any of the sections tested. Only thermal cracking was present, but was avoided when choosing a surface wave testing location. The rut depths are presented for all sections as shown in table 11 below.

Table 11. Rut Depths of Mn/Road Sections (mm).

Section	10/94	3/95	7/95	9/95	6/96
F3	1.19	2.78	3.57	3.57	4.76
F4	3.57	6.35	7.94	7.94	8.73
Cell 25	3.57	4.76	6.35	7.14	7.94
Cell 26	3.57	4.76	7.54	8.73	8.73
Cell 27	5.56	7.94	8.33	9.13	11.11
Cell 29	3.97	4.76	6.35	7.54	8.33
Cell 31	2.78	4.76	5.16	5.56	7.14

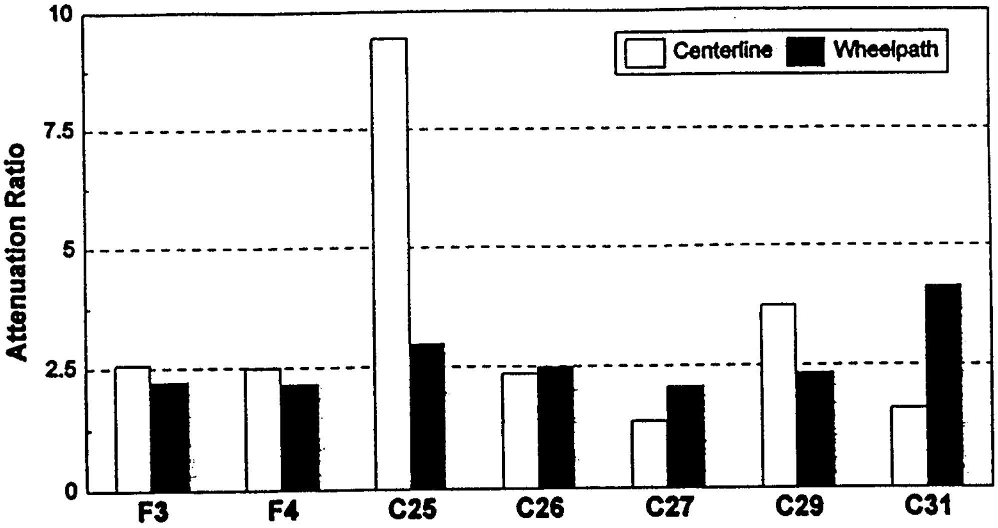

Figure 49. Attenuation at Centerline and Wheel Path for Mn/Road Cells.

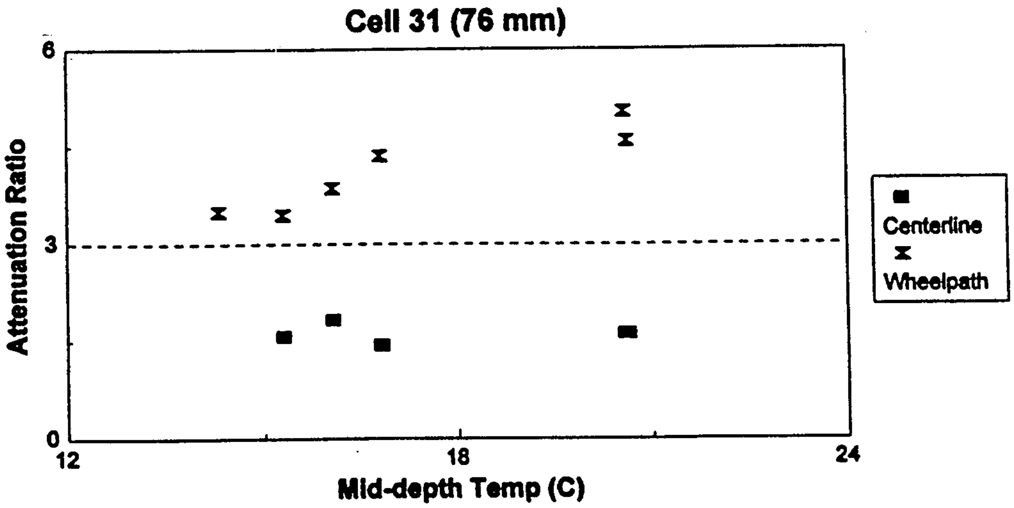

Figure 50. Attenuation at Centerline and Wheel Path on Cell 31.

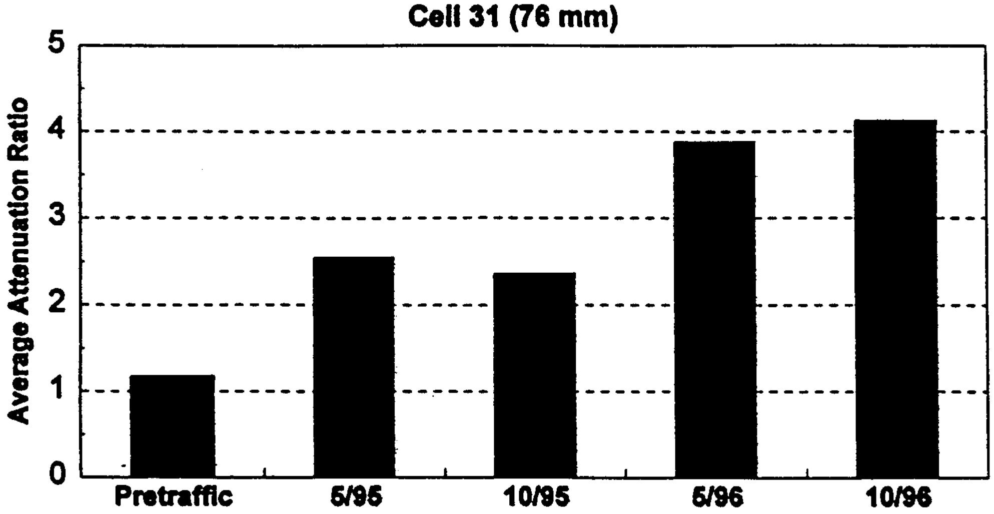

Figure 51. Cell 31 Damage Growth Using Attenuation.

Fatigue Cracking: The condition surveys of the Mn/Road sections agree with the stress wave results. No visual surface fatigue cracks were observed by October 1996. Also, the cores from October 1996 showed no visible cracking below the surface. Thus, if any fatigue cracking is present in the asphalt concrete, it is on a microcrack level.

Previous surface wave testing on US 1 in North Carolina also supports the absence of sub-surface cracks in the Mn/Road cells. At US 1, surface wave testing was attempted on an asphalt concrete pavement with no visual surface cracks. However, the surface waves were not able to propagate through the pavement. Cores of this pavement were taken and revealed that there were visible cracks below the surface of the pavement in the asphalt layer. These cracks prevented the propagation of the surface waves, resulting in complete signal attenuation prior to reaching the second sensor.

Fatigue cracking below the surface of the Mn/Road sections would have attenuated the surface waves significantly or completely prevented propagation of the waves. Therefore it is concluded that visible fatigue cracking is not present in the Mn/Road sections.

Rutting: The rut depths shown in table 11show that some rutting has developed in the Mn/Road sections. The fact that no fatigue cracking is present and rutting is present supports the finding of densification of the asphalt concrete. The surface wavespeed results indicate an increase in effective modulus over the testing period, concluded to be due to densification of the asphalt concrete. The diametral fatigue lab tests on Mn/Road cores shown in Figure 48 also support this claim.

It is interesting to note that the Low Volume Road sections have more rutting or densification than the Mainline sections. This is especially true when the ESAL values for the two roads are compared. The ESAL values for the Mainline Sections are more than six times as large as those for the Low Volume Road sections due to the much higher loading from freeway traffic. The reason for this increased densification may be less wandering of the wheelpath than on the Mainline sections.

Variation in the Damage Growth Measurements

It is imperative to note the numerous sources of variation and unavoidable error present in the data collected from the nine trips to Mn/Road. The nature of field testing inherently adds several factors beyond human control. There were also several sources of human variation that could not be eliminated.

Environmental considerations, which are constantly changing within each trip and from trip to trip, are a major source of variation. An attempt to account for temperature variation was made; however, not all temperature effects could be corrected. It is evident from the collected data that high temperatures will severely attenuate the stress waves and alter the results. The effect of high temperatures on attenuation will dominate over the effect of damage or healing on attenuation. This effect must be taken into account during analysis of the data.

Moisture content and weather patterns were also not taken into consideration. For instance, if it was abnormally rainy the week prior to testing, the moisture content may be higher and mid-depth temperatures lower than normal during testing. The effects of these parameters were not studied and therefore present a possible source of variability in the data.

Another source of error may be seasonal effects. A hot summer and a cold winter may affect the pavement in different ways. Testing in May might reflect effects from the winter while testing in August might include effects from the summer. Also, the traffic volume on the Mainline will be different during different seasons. Therefore the signals obtained may include effects from the seasons.

There are also human variations that are important to note. Throughout the testing, an 8 oz. hammer was used as the impulsive source. It is impossible for anyone to create the exact same signal magnitude and frequencies with each impact. Slight variations in the impact strength, angle, and location will result in deviations in the signals. In addition, although the same person was used to create the impact during each trip, a few different people were used from trip to trip. This will result in additional error since one person's impact may be different than another.

A final source of variation during the tests was the testing locations. During each trip, tests were conducted at the same locations. However, for each separate trip new testing spots were chosen near the previous spot because the pavement surface was slightly disturbed where the nuts were removed from the previous trips. Due to the sensitivity of the measurements, it was important to test a spot that was undisturbed and free of thermal cracks and debris. It is not known whether the slight disturbances would have altered the obtained signals, but to be sure there was no effect from the disturbance a new location was chosen each trip. In addition, the impact location would not have been able to handle impacts from all nine trips. Distortion and cracking would certainly have occurred, which would reduce the quality of the data.

It is also more realistic to choose a different testing spot during each trip to check the validity of the test method for field testing. A state highway agency would not be able to always test the same location on a road to monitor its damage. The method should be able to evaluate the pavement properties in any location (longitudinally) if the road is overall evenly trafficked.

Healing Assessment of Mn/Road Sections

Testing at Mn/Road was performed to measure the effects of healing that have been shown to occur in the lab and ALF studies. The primary requirement for this testing is a 24-hour rest period without any traffic loading. At Mn/Road, the Mainline is typically closed once a month for 2 days, but is only closed to traffic during the day and reopened at night. Rest periods of 24 hours are possible on the Low Volume Road and therefore testing to measure healing was performed on the Low Volume Road.

Two days were set for testing the Low Volume Road each trip. During the first day, the truck driver loaded the sections for a short period of time in order to reinitiate the microcrack damage after a long rest during the previous night. The sections were closed off while the truck was still running in order to obtain data as close to the beginning of the rest period as possible. Approximately 20 minutes elapsed prior to the first test for each section to epoxy the nuts at the test locations. Testing was then performed hourly throughout the day. The truck driver did not load the sections the second day, and testing continued hourly until about 5PM.

It is evident that the phase velocities will vary with temperature as shown in the effective modulus versus temperature plots. Therefore, the temperature-corrected phase velocities were used to study the healing effects. The healing index that was used during the ALF study was also used to measure healing of the Mn/Road sections.

This index was computed for the temperature-corrected phase velocities from the first and second mornings of each trip. The healing indices are shown for each section in figures 52 and A.22 through A.25. Cells 25 and 29 show the most consistently positive healing indices and the largest beneficial effects from healing of the asphalt. Every post traffic trip except August 1996 has an increase in phase velocity after the rest period. Results from the other three sections vary, showing some beneficial effects and some negative effects.

By averaging the healing indices for all the trips, an overall effect from the rest periods can be obtained. Figure 53 presents the average healing index for each section. In all the sections, the beneficial effects dominate as shown by the positive values of the average healing index. However, it is evident that significant healing may have only been observed on Cells 25, 26, and 29. Cells 27 and 31 show little benefit from the rest periods. These two sections are also the thinnest sections, which may influence the amount of healing that can occur.

It is important to note the factors that may influence the ability to measure healing in the field. There are several additional variables that were present during the Mn/Road testing and were not present during the previous lab and ALF studies.

The temperature was maintained constant for both the lab and ALF tests, but was not constant during the Mn/Road testing. Although the Mn/Road data were temperature corrected, this correction is only an approximation of the actual pavement behavior had the temperature remained constant.

Additionally, the frequency of the loading for the lab and ALF studies was much more severe than the truck loading during the Mn/Road tests. The beam flexural fatigue loading had a cyclic period of 0.6 seconds and the ALF loading had a cyclic period of 10 seconds. The Mn/Road truck loading had a much longer period of rest between loadings, about 6 minutes. This loading may not have been severe enough to propagate a significant amount of microcrack damage prior to the testing period.

The nature of the Mn/Road truck loading may actually be hindering the ability to measure healing of the asphalt sections. If healing is occurring in the Low Volume Road Mn/Road sections during rest periods, then one must consider the long rest periods each business day from 5PM until 8AM the next morning. There are also rest periods each weekend from 5PM on Friday until 8AM the following Monday morning. Although the time between each loading is small, the asphalt will experience some beneficial effects during the 6 minutes between each loading cycle. The effects of these rest periods add additional complexity to the task of measuring healing during the Mn/Road trips.

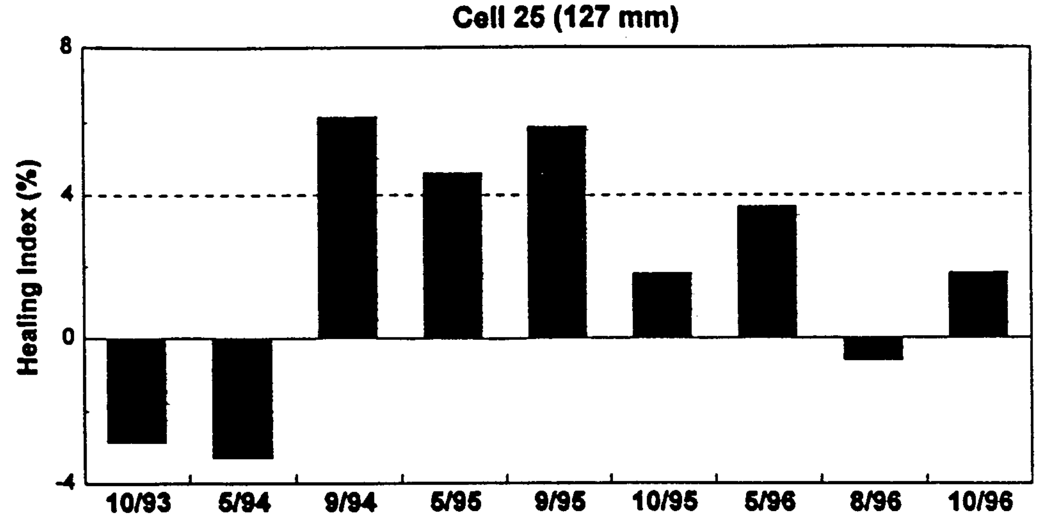

Figure 52. Healing of Asphalt Concrete of Cell 25.

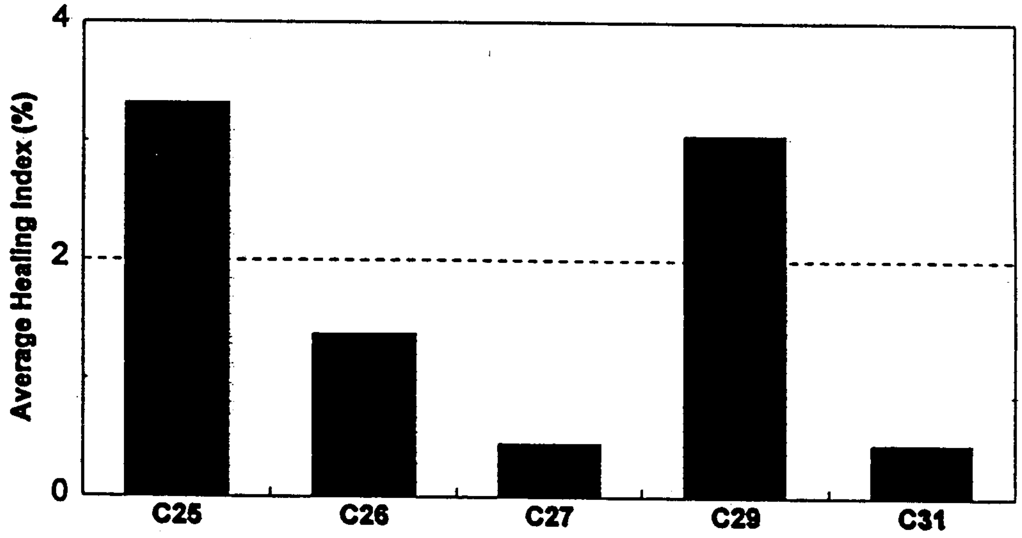

Figure 53. Average Healing Indices for Low Volume Road Cells.

Environmental factors are also present that could influence the healing ability of the asphalt. The moisture content of the sections varied depending on the amount of precipitation prior to testing. Weather conditions during the testing were also not constant. Temperature is a primary variable in determining the amount of healing that will occur in asphalt concrete. At higher temperatures, the asphalt has an increased ability to flow and close microcracks, which leads to a larger amount of healing. The results in Task 3 have shown that healing of flexural stiffness is much greater at 60°C than at 20°C during rest periods. This temperature dependence of healing will produce variability in the Mn/Road healing measurements because of temperature fluctuations that occur in the field. These environmental factors all need to be considered for accurate measurement of the healing of asphalt concrete in the field.

Conclusions

The stress wave test and analysis methods used in this study successfully detected fatigue damage growth and microdamage healing of asphalt pavements with different AC layer thicknesses and viscosities. This study demonstrated that the stress wave test can be effectively used for the condition assessment of asphalt surface layers.

The test results demonstrated the importance of microdamage healing during rest periods on the performance of asphalt concrete pavements.

The major reduction in the elastic modulus occurred during the early stage of fatigue life when there were no visible cracks on the pavement surface. This reduction was concluded to be related to microcrack initiation, propagation, and densification. Additional reduction of the elastic modulus near the failure seemed to coincide with rapid propagation of surface cracks.

The comparison between elastic moduli calculated from the direct approach and from the inversion approach at some selected damage conditions yielded less than 4% error. It was concluded that the use of an appropriate impact method can eliminate the inversion procedure when only surface layer properties need to be evaluated.

The fatigue damage under the tire edge due to shear stresses appears to be very significant. This finding suggests that, to accurately predict the fatigue performance of asphalt concrete pavements, the fatigue damage growth under the tire wall due to shear stresses needs to be evaluated in addition to tensile cracks at the bottom of the asphalt layer.

The results from the Mn/Road study have shown that stress wave testing can be used to measure microcrack damage growth and healing of asphalt concrete pavements in the field. Although uncontrolled environmental and traffic conditions provide more variability in the measurements, overall the test is capable of evaluating the in-situ pavement condition.

It was also determined that attenuation measurements are more sensitive for measuring microcrack damage growth than wavespeed measurements: however, they contain significantly more variability. This may be due to the more detailed analysis used in the frequency domain than in the time domain.

Healing of asphalt concrete pavements in the field is more difficult to measure than under controlled conditions, but can be detected by use of the stress wave test. The fact that healing does occur in pavements in the field during rest periods suggests that the performance and service life of the pavement will be increased if rest periods are introduced.

APPENDIX A

ADDITIONAL RESULTS FROM THE ALF AND THE MN/ROAD STUDIES

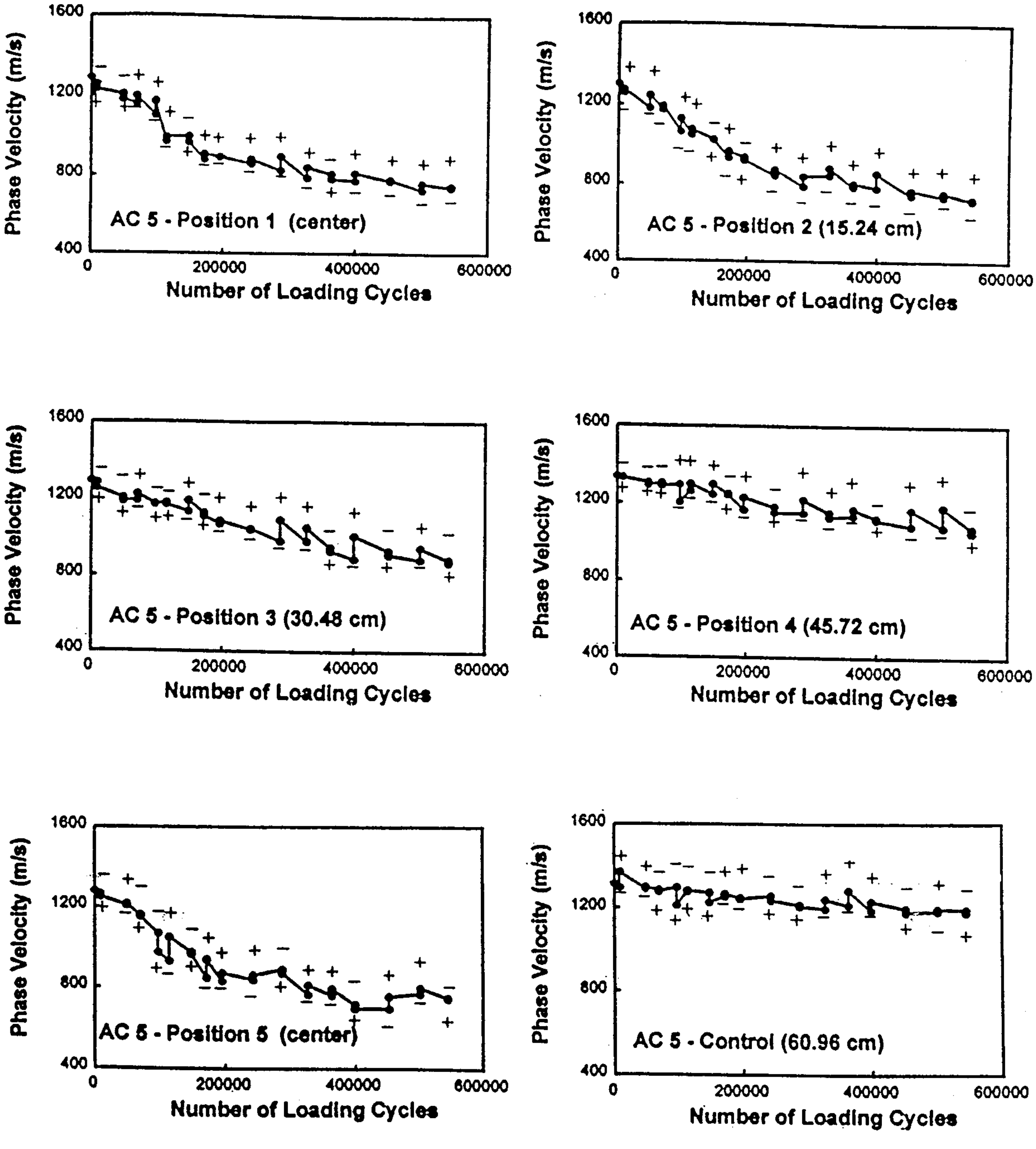

Figure A-1. Changes in Phase Velocity During Fatigue Loading and Rest Periods (204-mm AC 5-Section).

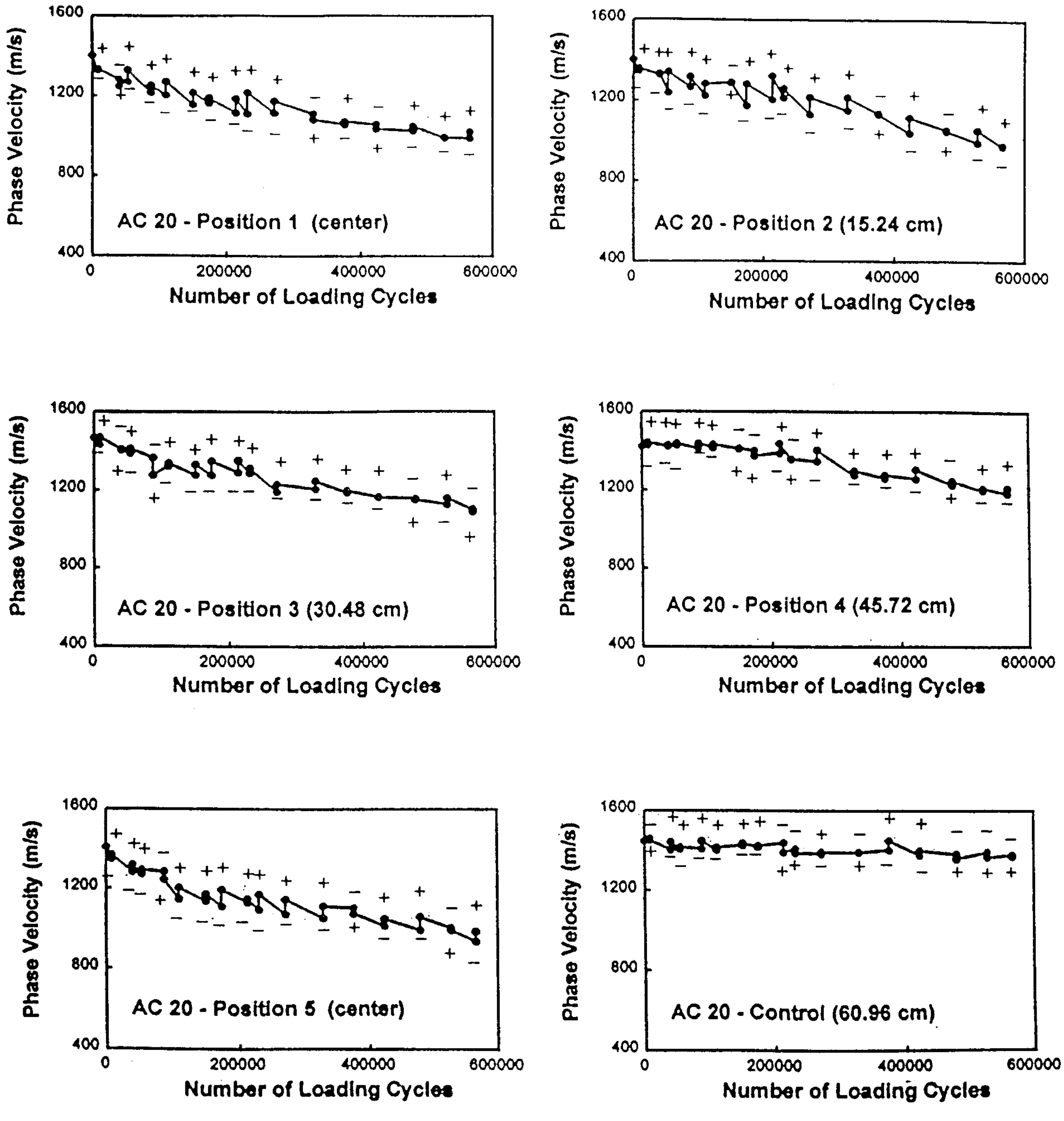

Figure A.2 Changes in Phase Velocity During Fatigue Loading and Rest Periods (204-mm AC 20 Section).

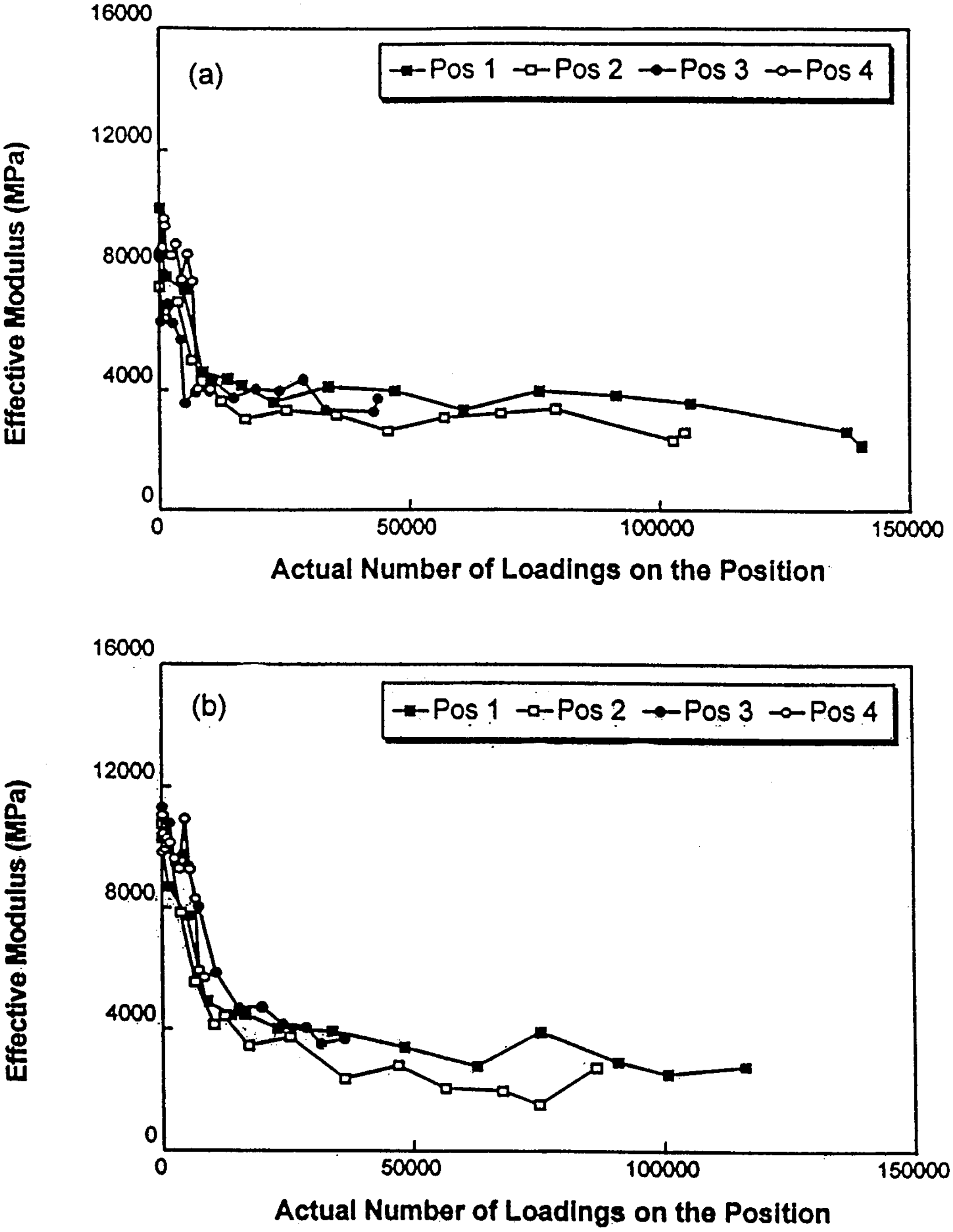

Figure A.3 Actual Number of Loadings on Each Position Considering the Normally Distributed Loading Patterns: (a) 102-mm AC 5 Section; (b) 102-mm AC 20 Section.

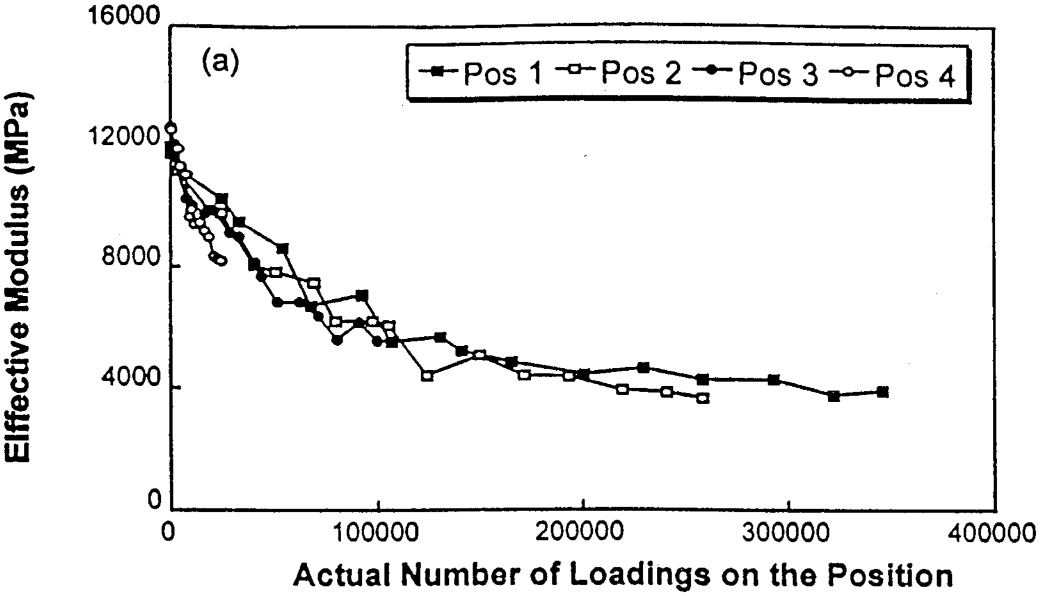

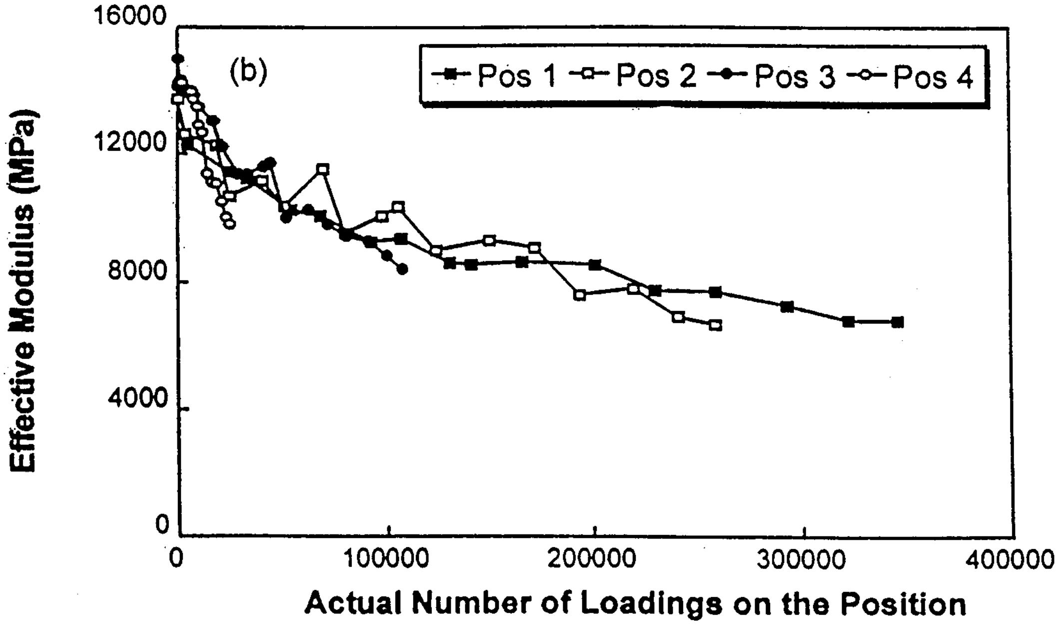

Figure A.4 Actual Number of Loadings on Each Position Considering the Normally Distributed Loading Patterns: (a) 204-mm AC 5 Section; (b) 204-mm AC 20 Section.

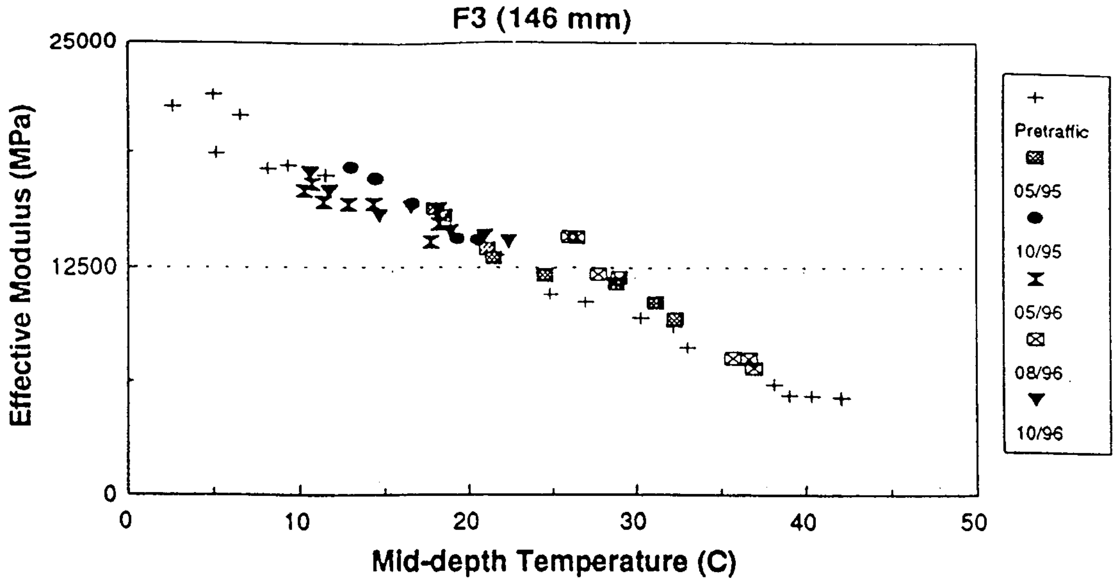

Figure A.5 Effective Moduli of Cell F3.

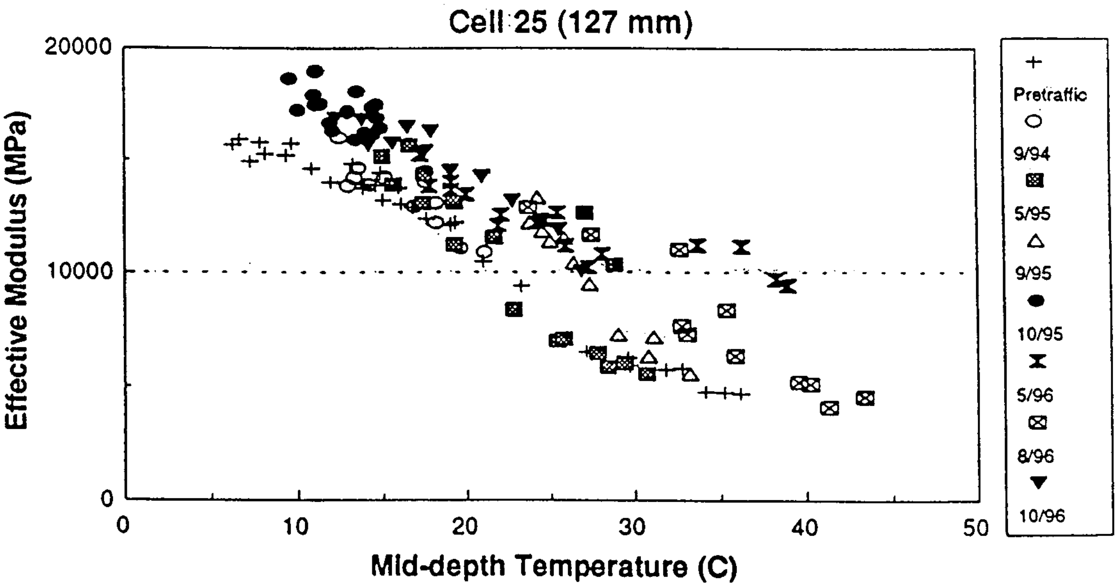

Figure A.6 Effective Moduli of Cell 25.

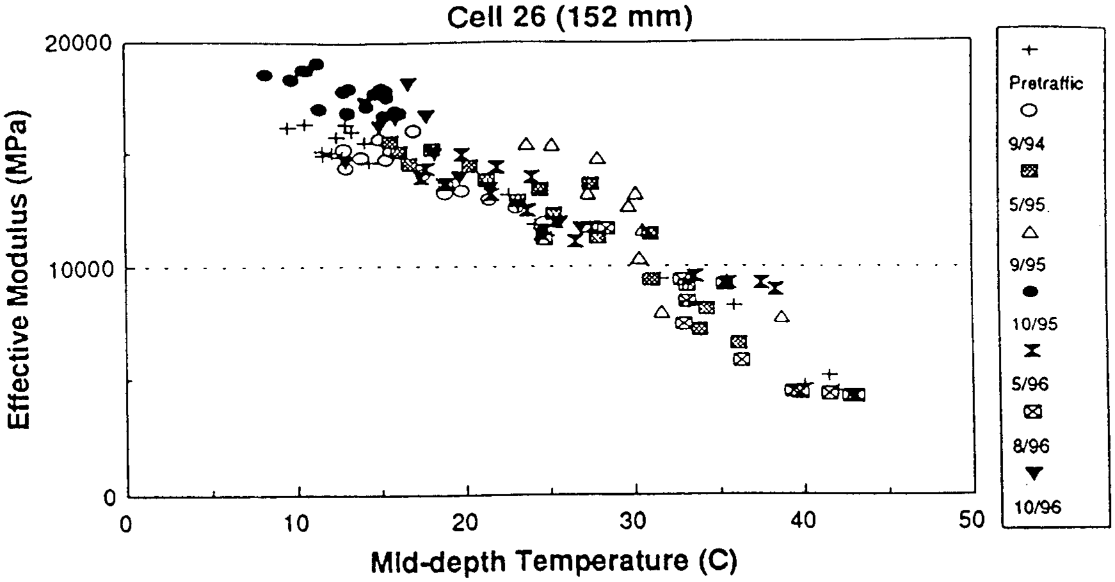

Figure A.7 Effective Moduli of Cell 26.

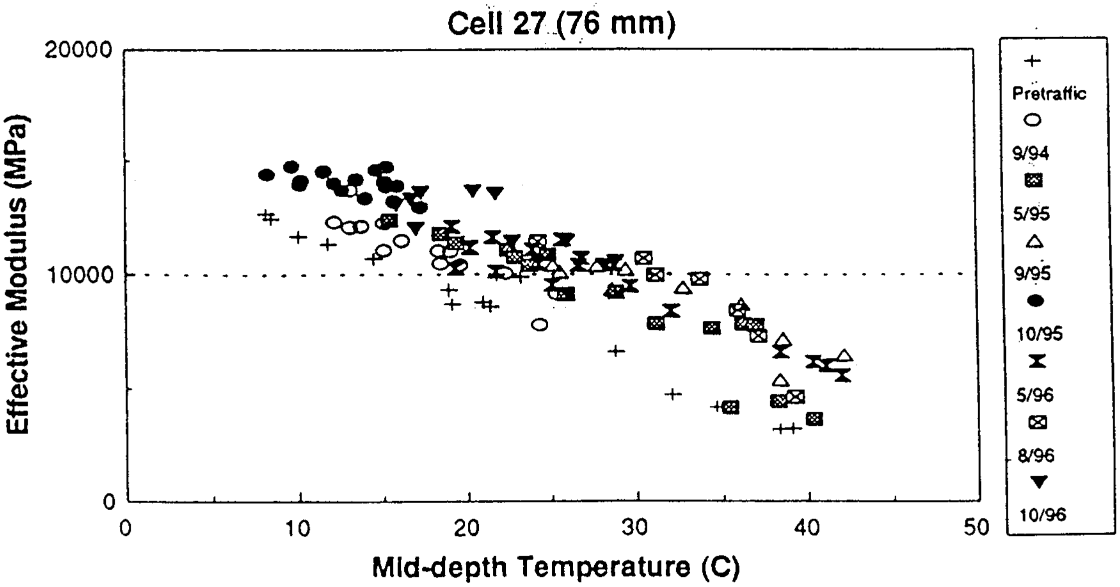

Figure A.8 Effective Moduli of Cell 27.

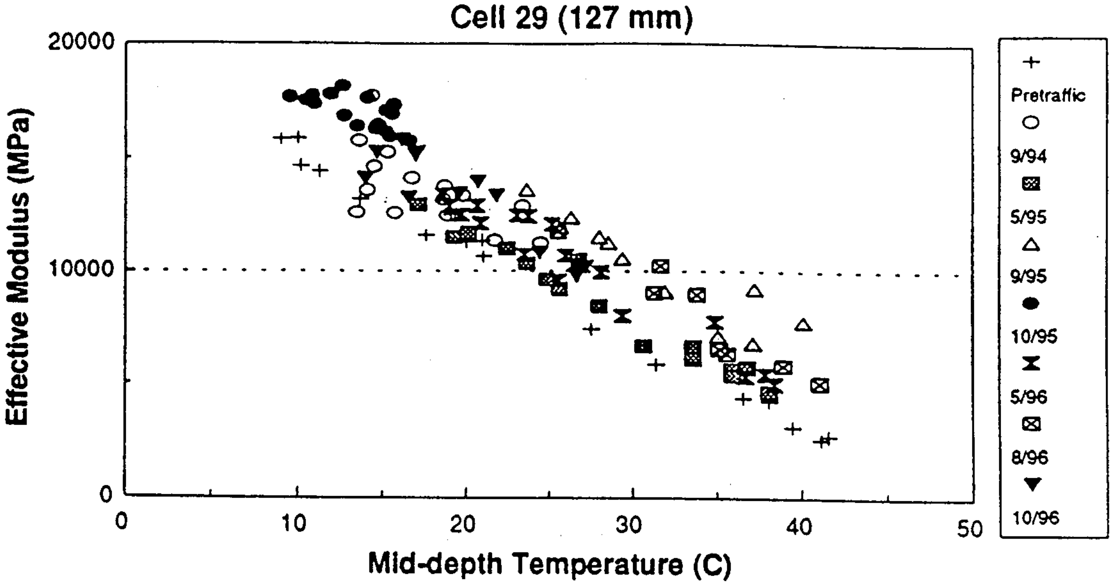

Figure A.9 Effective Moduli of Cell 29.

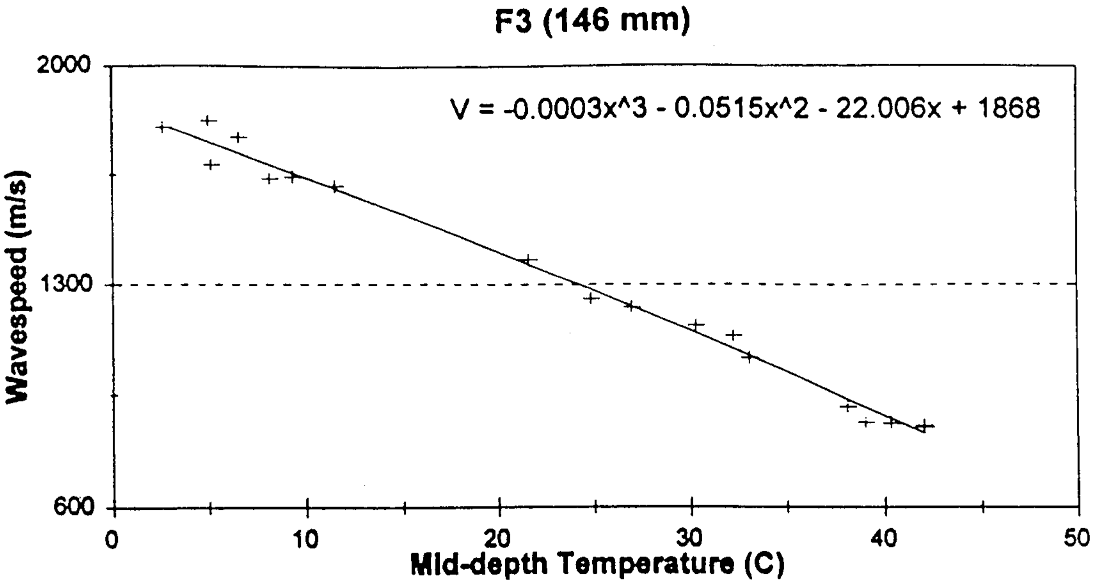

Figure A.10 Cell 25 Pretraffic Curve Fit.

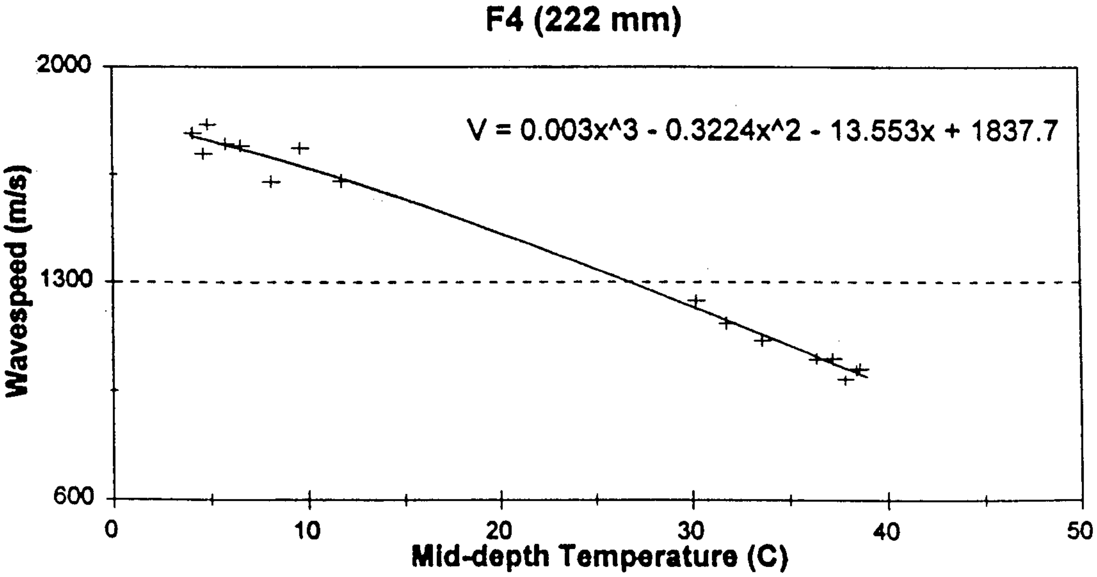

Figure A.11 Cell F4 Pretraffic Curve Fit.

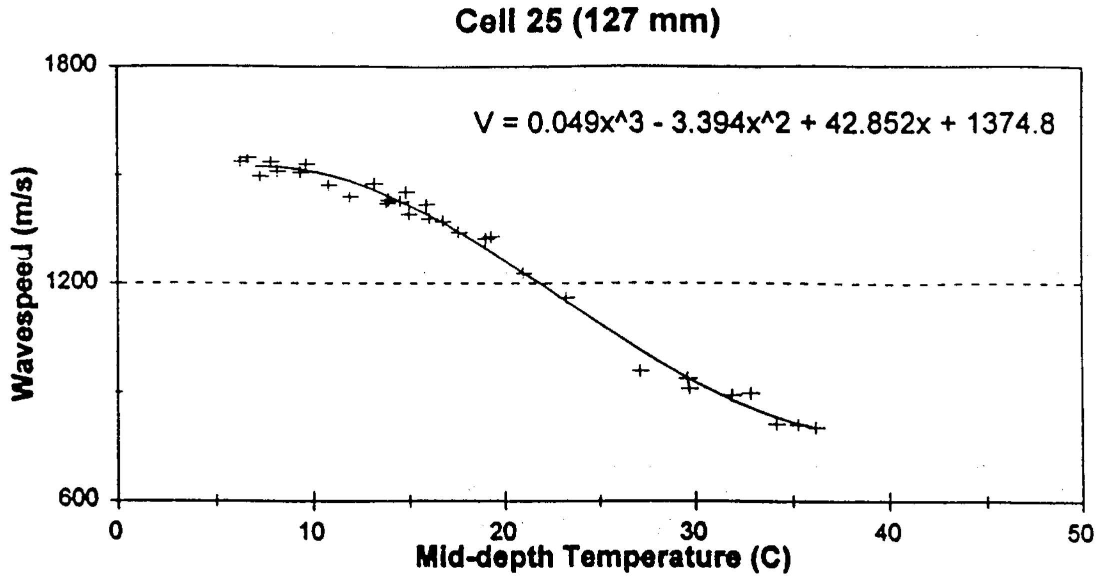

Figure A.12 Cell 25 Pretraffic Curve Fit.

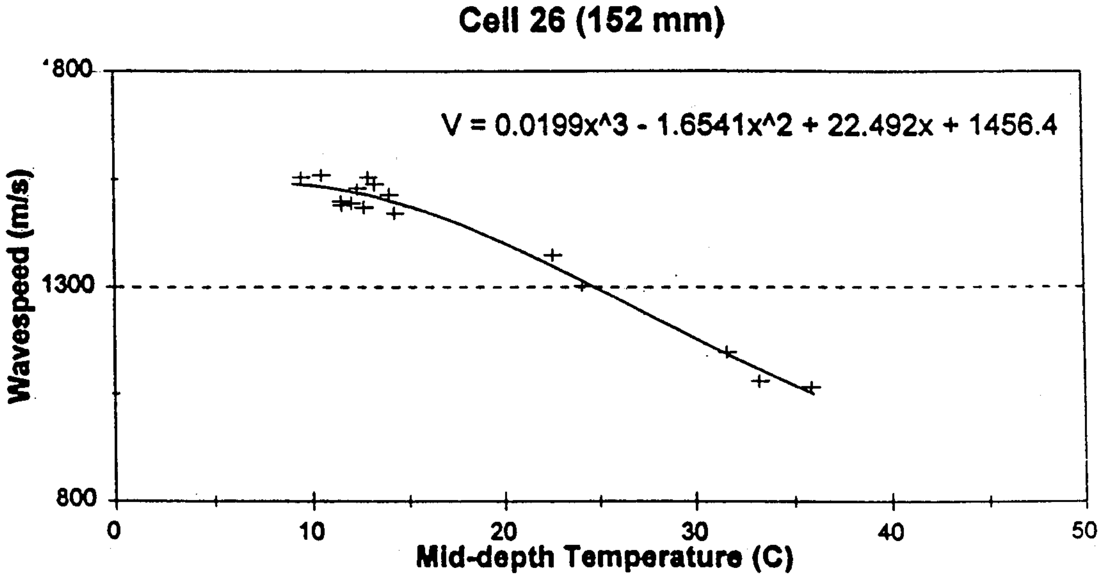

Figure A.13 Cell 26 Pretraffic Curve Fit.

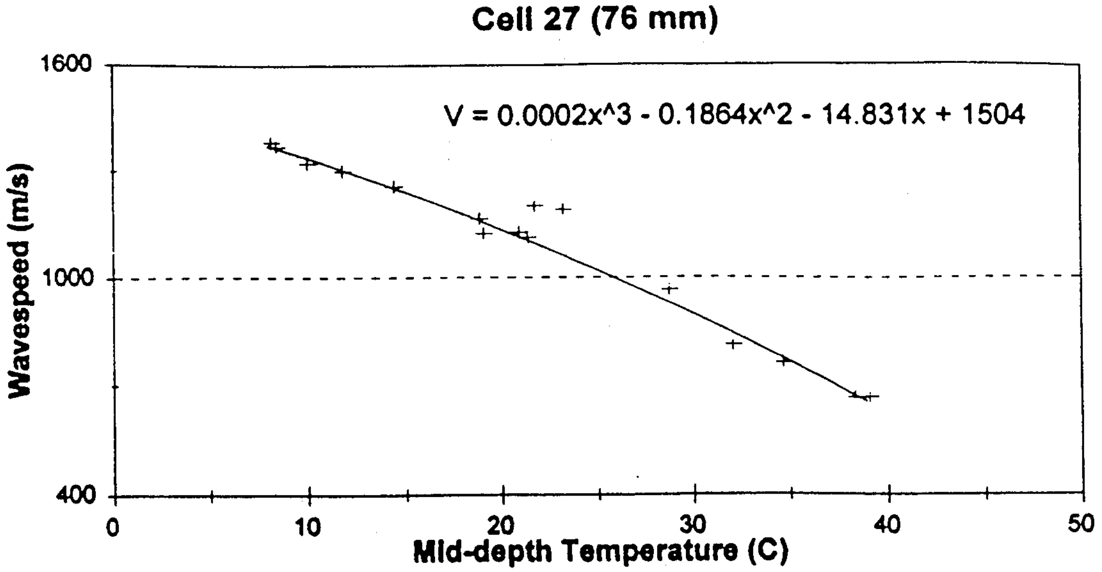

Figure A.14 Cell 27 Pretraffic Curve Fit.

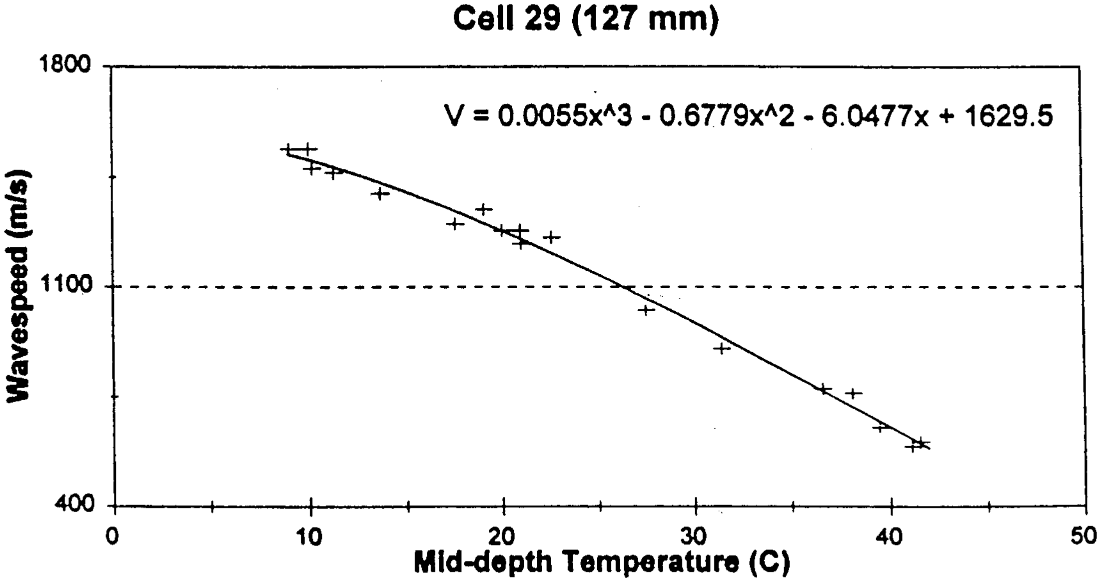

Figure A.15 Cell 29 Pretraffic Curve Fit.

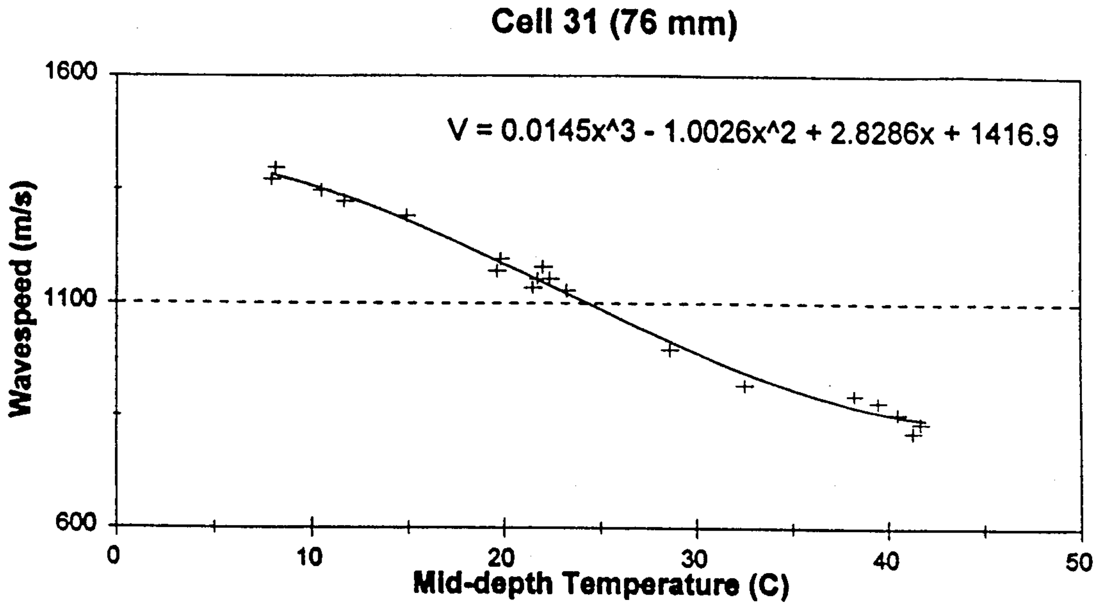

Figure A.16 Cell 31 Pretraffic Curve Fit.

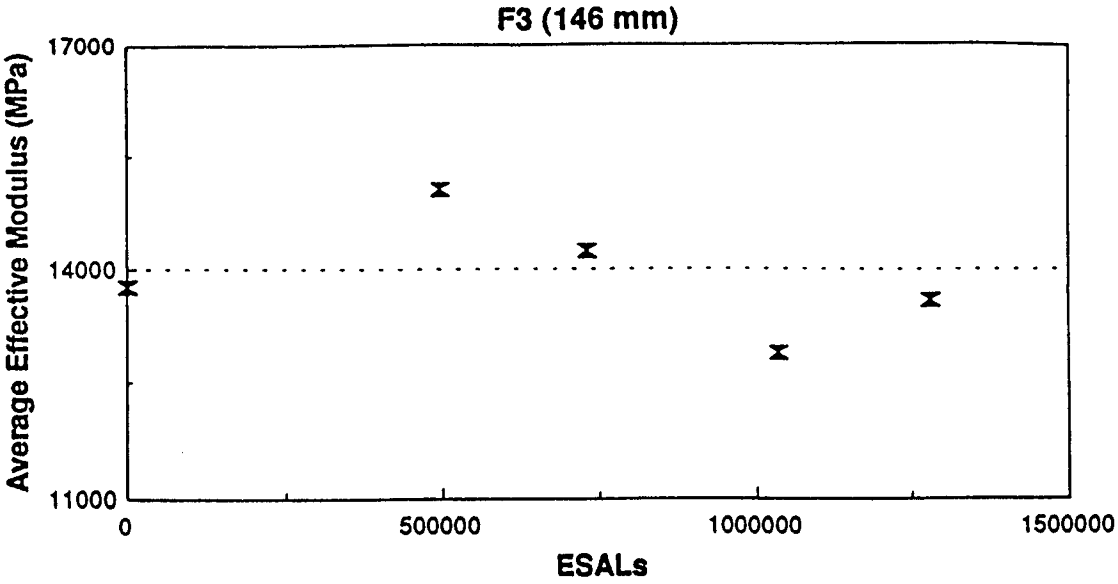

Figure A.17 Cell F3 Damage Growth Using Corrected Effective Moduli.

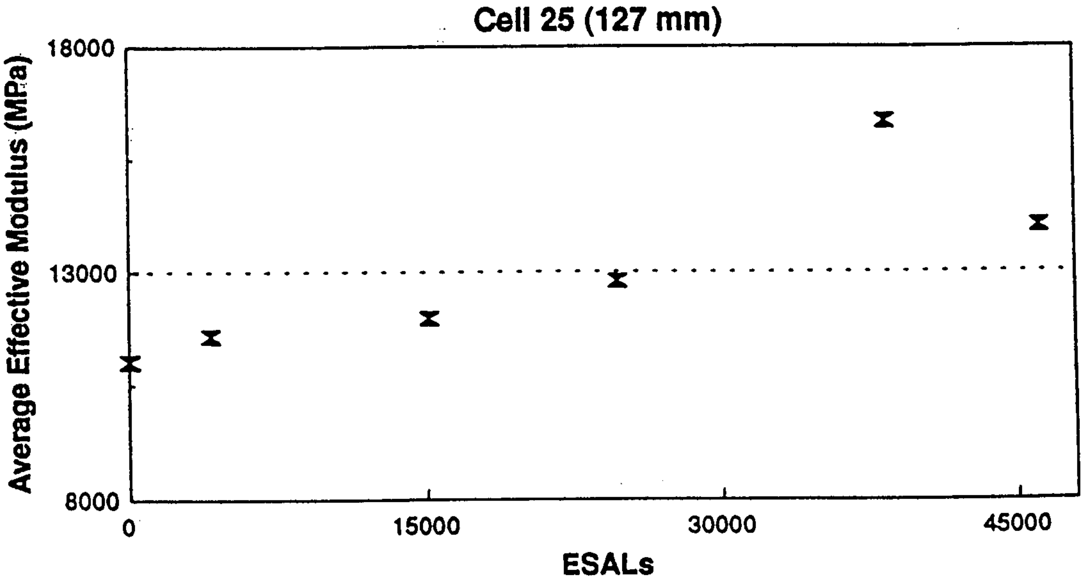

Figure A.18 Cell Damage Growth Using Corrected Effective Moduli.

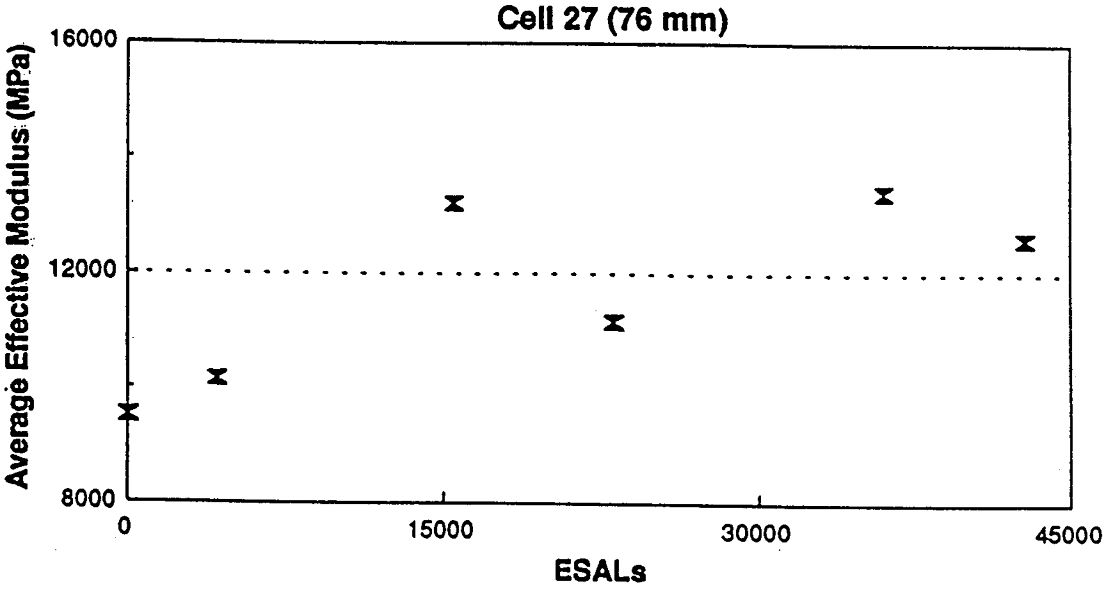

Figure A.19 Cell 26 Damage Growth Using Corrected Effective Moduli.

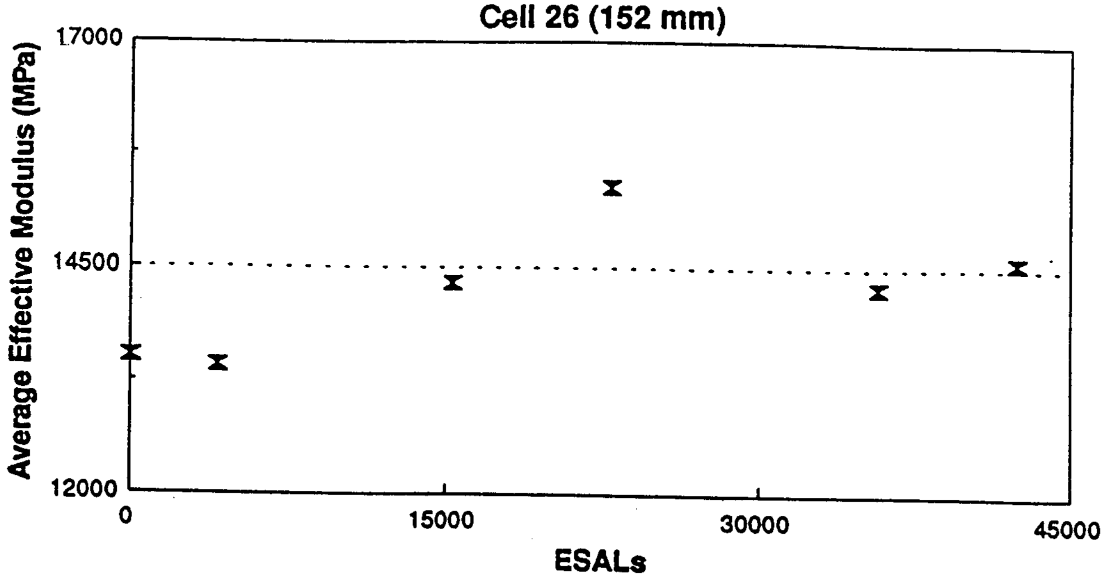

Figure A.20 Cell 27 Damage Growth Using Corrected Effective Moduli.

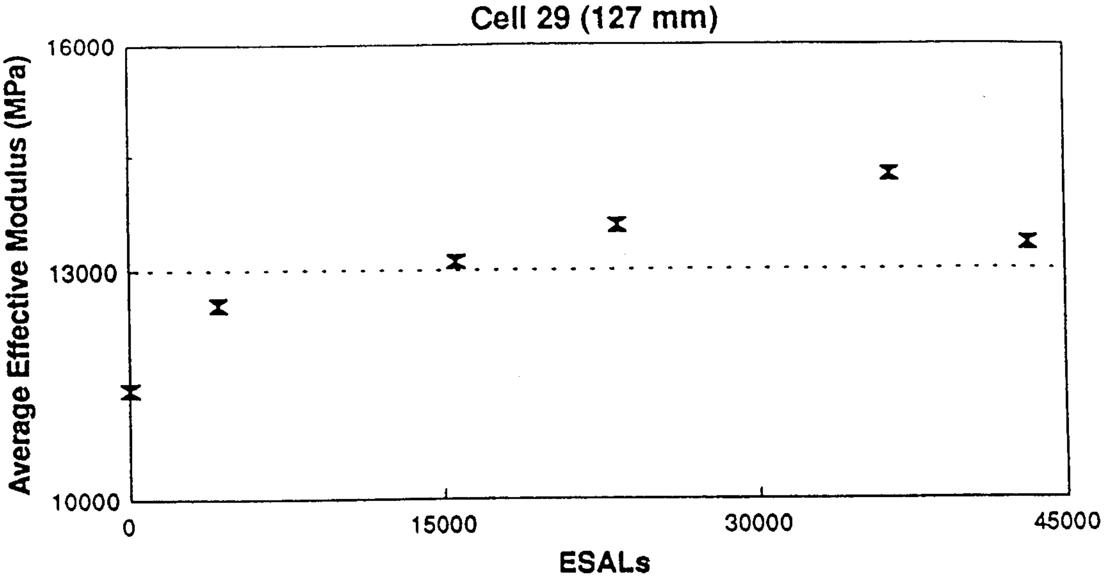

Figure A.21 Cell 29 Damage Growth Using Corrected Effective Moduli.

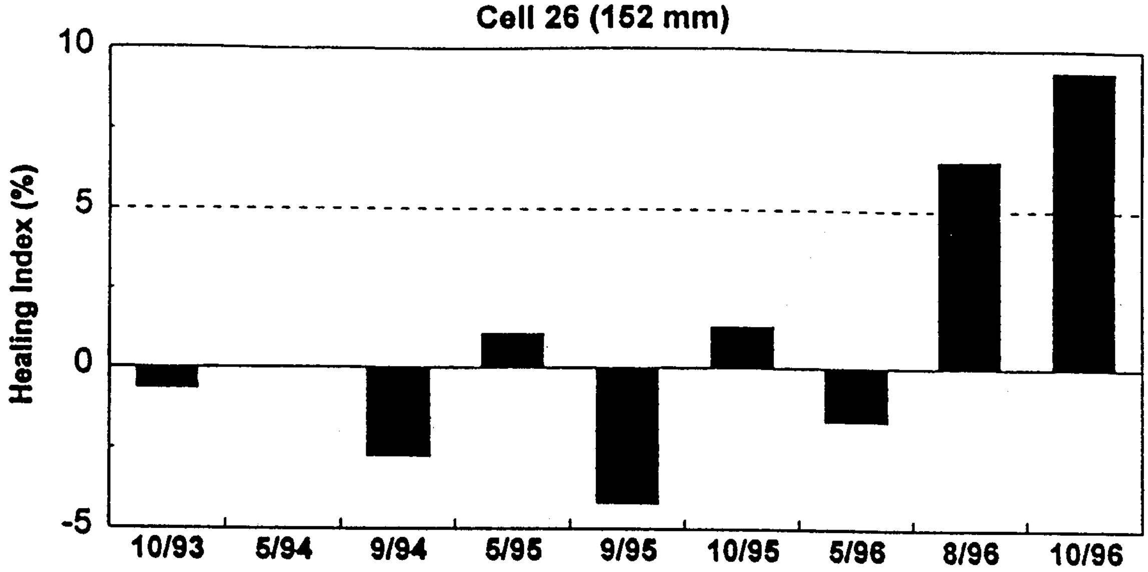

Figure A.22 Healing of Asphalt Concrete in Cell 26.

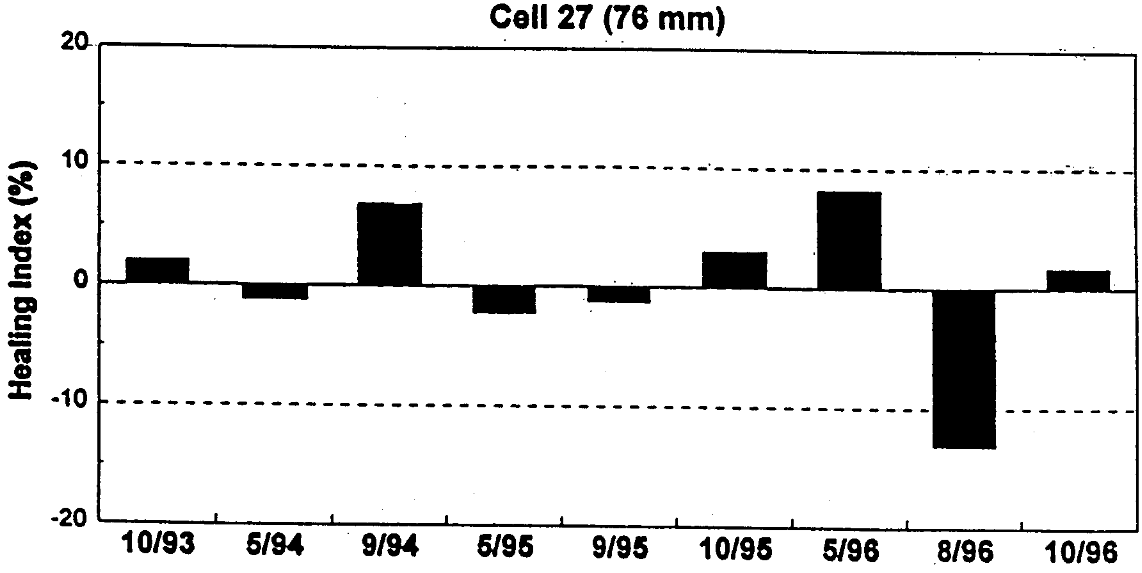

Figure A.23 Healing of Asphalt Concrete in Cell 27.

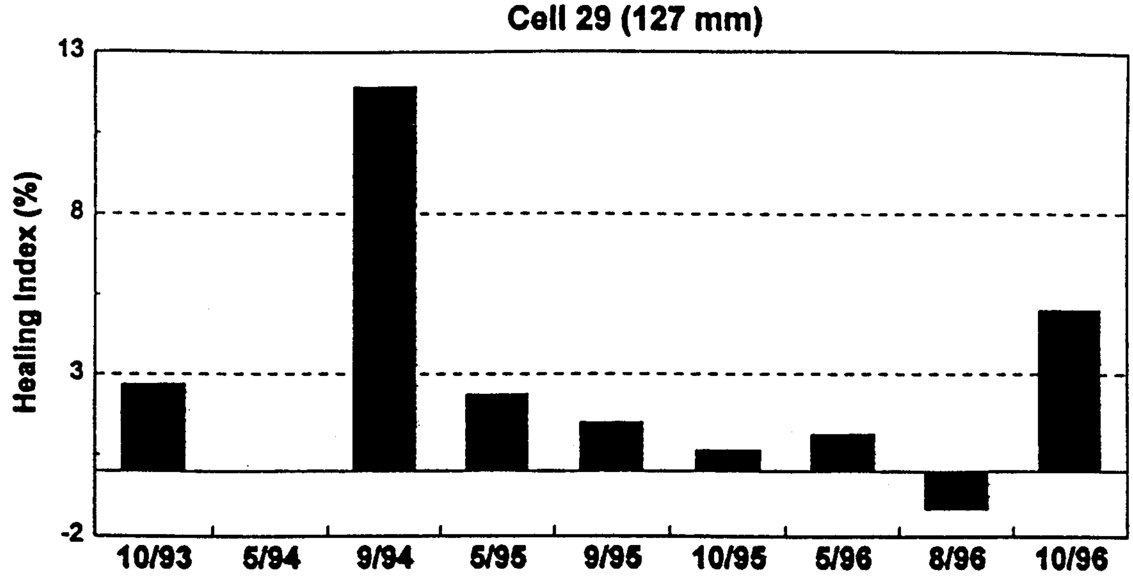

Figure A.24 Healing of Asphalt Concrete in Cell 29.

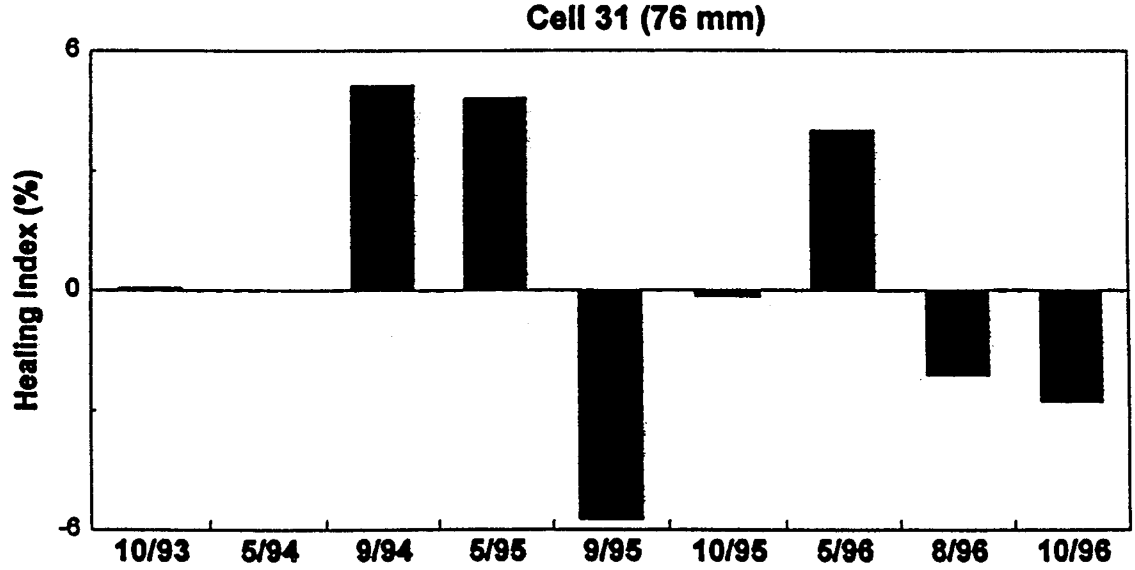

Figure A.25 Healing of Asphalt Concrete in Cell 31.

APPENDIX B

NUMERICAL SOLUTIONS FOR LAYERED MEDIA

APPENDIX B

NUMERICAL SOLUTIONS FOR LAYERED MEDIA

D.1 Equations of Motion in Cartesian Coordinate System

The dynamic equilibrium equations (the equations of balance of linear momentum) in a Cartesian coordinate system for an infinitesimal element are expressed as

$$\frac{\partial \sigma_x}{\partial x}+\frac{\partial \tau_{xy}}{\partial y}+\frac{\partial \tau_{xz}}{\partial z}=\rho\frac{\partial^2 u}{\partial t^2} \tag{B.1}$$

$$\frac{\partial \tau_{xy}}{\partial x}+\frac{\partial \sigma_y}{\partial y}+\frac{\partial \tau_{yz}}{\partial z}=\rho\frac{\partial^2 v}{\partial t^2}, \tag{B.2}$$

$$\frac{\partial \tau_{zx}}{\partial x}+\frac{\partial \tau_{yz}}{\partial y}+\frac{\partial \sigma_z}{\partial z}=\rho\frac{\partial^2 w}{\partial t^2}, \tag{B.3}$$

in which *u, v,* and *w* are the components of displacement in x, y, z directions, respectively; σ and τ are the normal and shear stresses on the surface corresponding to the indices; and ρ is the mass density of material.

For small deformations (linear geometry), the components of displacement *u, v,* and *w* are related to the components of the linear strain tensor by the strain-displacement equations expressed as

$$\varepsilon_x=\frac{\partial u}{\partial x}, \qquad \varepsilon_y=\frac{\partial v}{\partial y}, \qquad \varepsilon_z=\frac{\partial w}{\partial z}, \tag{B.4}$$

$$\gamma_{xy}=\frac{\partial u}{\partial y}+\frac{\partial v}{\partial x}, \qquad \gamma_{xz}=\frac{\partial u}{\partial z}+\frac{\partial w}{\partial x}, \qquad \gamma_{yz}=\frac{\partial v}{\partial z}+\frac{\partial w}{\partial y}, \tag{B.5}$$

in which ε is the longitudinal strain in the direction of x, y and z corresponding to the indices, respectively; and γ is the shear strain between the linear elements parallel to the respective indices.

The stress-strain relation (Hook's law, constitutive equation) for the isotropic, linear material can be expressed as

$$\sigma_x = \lambda e + 2G\varepsilon_x = \frac{1}{E}\left\{\sigma_x - \nu(\sigma_y + \sigma_z)\right\}, \tag{B.6}$$

$$\sigma_y = \lambda e + 2G\varepsilon_y = \frac{1}{E}\left\{\sigma_y - \nu(\sigma_z + \sigma_x)\right\}, \tag{B.7}$$

$$\sigma_z = \lambda e + 2G\varepsilon_z = \frac{1}{E}\left\{\sigma_z - \nu(\sigma_x + \sigma_y)\right\}, \tag{B.8}$$

$$\tau_{yz} = G\gamma_{xy}, \tag{B.9}$$

$$\tau_{xz} = G\gamma_{xz}, \tag{B.10}$$

$$\tau_{yz} = G\gamma_{yz}, \tag{B.11}$$

where e is the volumetric strain defined as

$$e = \frac{\partial u}{\partial x} + \frac{\partial v}{\partial y} + \frac{\partial w}{\partial z}, \tag{B.12}$$

and λ is Lame's constant and G is the shear modulus given by

$$\lambda = \frac{\nu E}{(1+\nu)(1-2\nu)} \tag{B.13}$$

$$G = \frac{E}{2(1+\nu)} \tag{B.14}$$

where v is Poisson's ratio and E is Young's modulus.

Substituting Eqs. (B.4) through (B.11) into Eqs. (B.1) to (B.3), and rearranging Eqs. (B.1) to (B.3) for displacement as the dependent variable (stiffness formulation), the equation of motions are obtained as

$$(\lambda + G)\frac{\partial e}{\partial x} + G\nabla^2 u = \rho\frac{\partial^2 u}{\partial t^2}, \tag{B.15}$$

$$(\lambda + G)\frac{\partial e}{\partial y} + G\nabla^2 v = \rho\frac{\partial^2 v}{\partial t^2}, \tag{B.16}$$

$$(\lambda + G)\frac{\partial e}{\partial z} + G\nabla^2 w = \rho\frac{\partial^2 w}{\partial t^2} \quad \text{.} \tag{B.17}$$

Using vector notation, Eqs. (B.15) through (B.17) can be rewritten as

$$(\lambda + G)\nabla(\nabla \bullet \mathbf{u}) + G\nabla^2 \mathbf{u} = \rho\frac{\partial^2 \mathbf{u}}{\partial t^2} \quad \text{.} \tag{B.18}$$

Using the relationship given by

$$\nabla^2 \mathbf{u} = \nabla(\nabla \bullet \mathbf{u}) - \nabla \times (\nabla \times \mathbf{u}), \tag{B.19}$$

the equation of motion in Eq. (B.18) can be rewritten as

$$(\lambda + 2G)\nabla(\nabla \bullet \mathbf{u}) - G\nabla \times (\nabla \times \mathbf{u}) = \rho\frac{\partial^2 \mathbf{u}}{\partial t^2} \quad \text{.} \tag{B.20}$$

B.2 Stiffness Matrix

B.2.1 Solution of Wave Equation

The dynamic response of a layered media to an external load or seismic excitation can be determined by solving a wave propagation problem. A matrix solution method for wave propagation in a layered elastic media was established by Thomson (1950) and Haskel (1953), and is known as the transfer matrix approach. In this approach, the transfer matrix is formulated considering the continuity of displacements and the force equilibrium at the top and bottom surfaces of each elastic layer and the adjacent layers. The dynamic response of a layered system can then be related to the exciting motion or load by matrix multiplication of the transfer matrices for each layer.

An alternative matrix solution for wave propagation in layered media, known as the stiffness matrix approach, was established by Kausel and Roesset (1981). In this approach, the forces at the interfaces between layers are related directly to displacements at the same locations by a dynamic stiffness matrix. A global stiffness matrix can then be assembled for the complete layered system considering the layer stiffness at the interface of each layer. The global load vectors correspond to external forces at the interfaces of this layered system.

B.2.2 Stiffness Matrix of an Individual Layer

The stiffness matrix approach is employed in this research to solve the wave propagation problem for a layered system. In the stiffness matrix approach, the displacements developed at the upper and lower interfaces of an isolated layer are related to the external loads applied at the same interfaces through the stiffness matrix. The displacements U and the loads P at the interfaces are shown in Figure B.1. The interrelationship between the loads P and the stresses S at the upper and lower interfaces for an isolated layer is also presented in the same figure. The stiffness matrix in a Cartesian coordinate system can be derived by considering the boundary conditions at the upper and lower interfaces for each of the isolated layers. Detailed derivation of the stiffness matrices can be found in Kausel and Roesset (1981).

The resulting stiffness matrix for the j-th soil layer is summarized as

$$\mathrm{K}^{j} = 2kG\begin{Bmatrix} \mathrm{K}_{11}{}^{j} & \mathrm{K}_{12}{}^{j} \\ \mathrm{K}_{21}{}^{j} & \mathrm{K}_{22}{}^{j} \end{Bmatrix} \tag{B.21}$$

in which the elements are expressed as

$$\mathrm{K}_{11}{}^{j} = \frac{1-s^2}{2D}\begin{bmatrix} \frac{1}{s}(C^r S^s - rsC^s S^r) & -(1-C^r C^s + rsS^r S^s) \\ -(1-C^r C^s + rsS^r S^s) & \frac{1}{r}(C^s S^r - rsC^r S^s) \end{bmatrix} - \frac{1+s^2}{2}\begin{bmatrix} 0 & 1 \\ 1 & 0 \end{bmatrix} \tag{B.22}$$

$$\mathrm{K}_{12}{}^{j} = \frac{1-s^2}{2D}\begin{bmatrix} \frac{1}{s}(rsS^r - S^s) & -(C^r - C^s) \\ (C^r - C^s) & \frac{1}{r}(rsS^s - S^r) \end{bmatrix} \tag{B.23}$$

$$\mathrm{K}_{21}{}^{j} = \frac{1-s^2}{2D}\begin{bmatrix} \frac{1}{s}(rsS^r - S^s) & (C^r - C^s) \\ -(C^r - C^s) & \frac{1}{r}(rsS^s - S^r) \end{bmatrix} \tag{B.24}$$

$$\mathrm{K}_{22}{}^{j} = \frac{1-s^2}{2D}\begin{bmatrix} \frac{1}{s}(C^r S^s - rsC^s S^r) & (1-C^r C^s + rsS^r S^s) \\ (1-C^r C^s + rsS^r S^s) & \frac{1}{r}(C^s S^r - rsC^r S^s) \end{bmatrix} + \frac{1+s^2}{2}\begin{bmatrix} 0 & 1 \\ 1 & 0 \end{bmatrix} \tag{B.25}$$

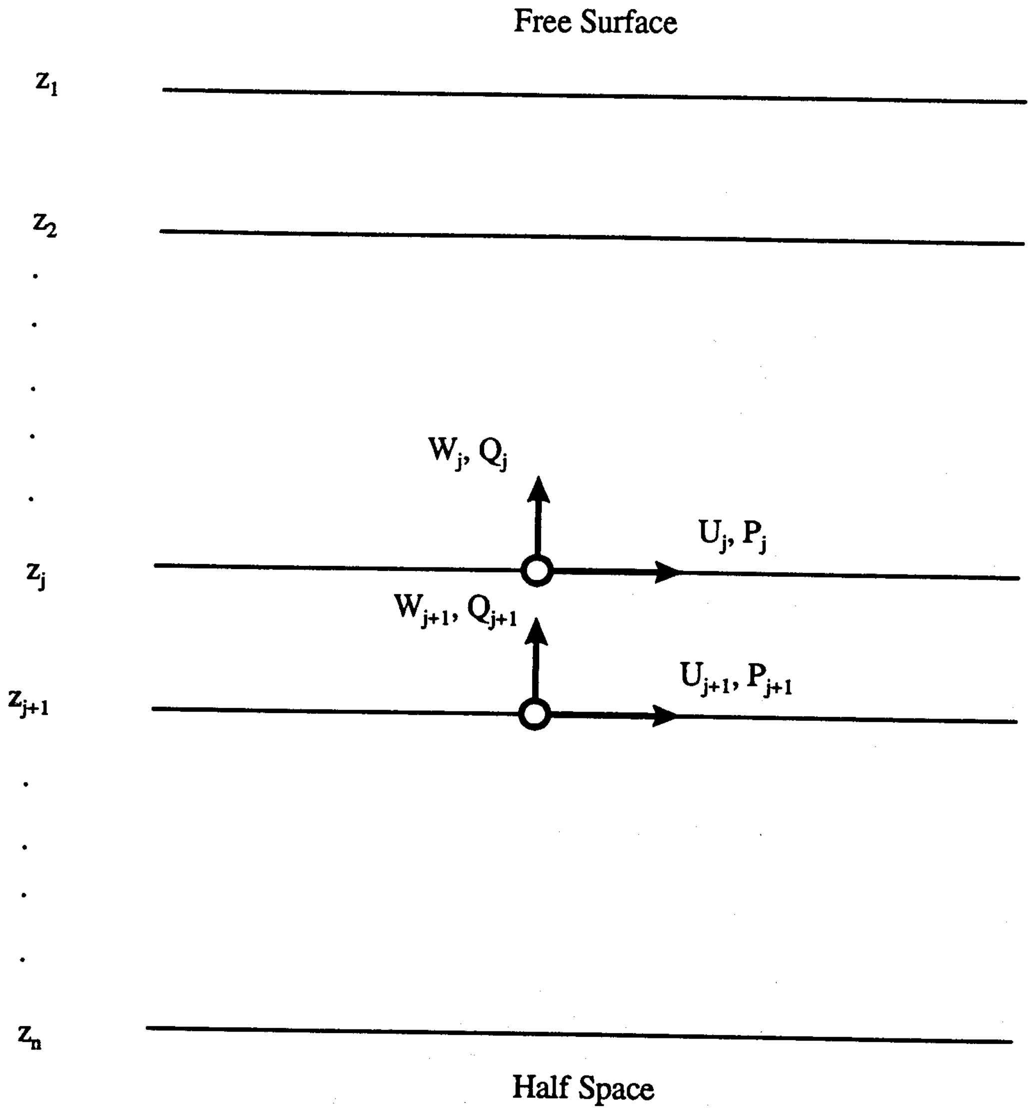

Figure B.1 Load and Displacement Relationship in j-th Layer.

where $$C^r = \cosh(krh) \qquad S^r = \sinh(krh) \tag{B.26}$$

$$C^s = \cosh(ksh) \qquad S^s = \sinh(ksh) \tag{B.27}$$

$$D = 2(1 - C^r C^s) + \left(\frac{1}{rs} + rs\right) S^r S^s \tag{B.28}$$

$$r = \sqrt{1 - \left(\frac{V}{V_p}\right)^2} \tag{B.29}$$

$$s = \sqrt{1 - \left(\frac{V}{V_s}\right)^2} \tag{B.30}$$

where h = layer thickness,
k = wave number,
V = phase velocity,
V_p = compression wave speed, and
V_s = shear wave speed.

In an elastic half-space, waves are transmitted only in the downward direction. Thus, a different stiffness matrix is obtained. The stiffness for a half-space is

$$\mathrm{K}^H = 2kG\left\{\frac{(1-s^{2)}}{2(1-rs)}\begin{bmatrix} r & 1 \\ 1 & s \end{bmatrix} - \begin{bmatrix} 0 & 1 \\ 1 & 0 \end{bmatrix}\right\} \tag{B.31}$$

where the superscript H denotes the stiffness is for a half-space.

B.2.3 Global Stiffness Matrix for a System

The global stiffness matrix of the system K is constructed by combining the individual layer stiffness matrix K^j for each layer. $\mathbf{K}_{22}$ of the upper layer and $\mathbf{K}_{11}$ of the lower elements are overlapped considering the compatibility of displacements and the force equilibrium at layer interfaces. This process is very similar to the construction of the global stiffness matrix in Finite Element Method.. Assembling a global stiffness matrix is illustrated in Figure B.2.

$$[\mathbf{K}] = \begin{bmatrix} \mathbf{K}^{1}_{11} & \mathbf{K}^{1}_{12} & & & \\ \mathbf{K}^{1}_{21} & \mathbf{K}^{1}_{22}+\mathbf{K}^{2}_{11} & \mathbf{K}^{2}_{12} & & \\ & \mathbf{K}^{2}_{21} & \mathbf{K}^{2}_{22} & & \\ & & & \ddots & \\ & & & \mathbf{K}^{n-1}_{11} & \mathbf{K}^{n-1}_{12} \\ & & & \mathbf{K}^{n-1}_{21} & \mathbf{K}^{n-1}_{22}+\mathbf{K}^{n} \end{bmatrix}$$

Figure B.2 Assembling Layer Stiffness Matrices Into a Global Stiffness Matrix.

B.3 Equations of Motion in Cylindrical Coordinate System

The equilibrium equations in cylindrical coordinates are expressed as

$$\frac{\partial \sigma_r}{\partial r} + \frac{1}{r} \cdot \frac{\partial \tau_{r\theta}}{\partial \theta} + \frac{\partial \tau_{rz}}{\partial z} + \frac{\sigma_r - \sigma_\theta}{r} = \rho \frac{\partial^2 u_r}{\partial t^2} \tag*{(B.32)}$$

$$\frac{\partial \tau_{r\theta}}{\partial r} + \frac{1}{r} \cdot \frac{\partial \sigma_\theta}{\partial \theta} + \frac{\partial \tau_{\theta z}}{\partial z} + \frac{2}{r} \tau_{r\theta} = \rho \frac{\partial^2 u_\theta}{\partial t^2} \tag*{(B.33)}$$

$$\frac{\partial \tau_{rz}}{\partial r} + \frac{1}{r} \cdot \frac{\partial \tau_{\theta z}}{\partial \theta} + \frac{\partial \sigma_z}{\partial z} + \frac{1}{r} \tau_{rz} = \rho \frac{\partial^2 u_z}{\partial t^2} \tag*{(B.34)}$$

where u, σ, and τ are the displacements, normal stresses, and tangential stresses, respectively, in the directions identified by the subindices r (radial), θ (circumferential), and z (vertical). These relationships are shown in Figure B.3.

The strains can be expressed in terms of displacement by the equations

$$\varepsilon_r = \frac{\partial u_r}{\partial r} \tag*{(B.35)}$$

$$\varepsilon_\theta = \frac{u_r}{r} + \frac{1}{r} \cdot \frac{\partial u_\theta}{\partial \theta} \tag*{(B.36)}$$

$$\varepsilon_z = \frac{\partial u_z}{\partial z} \tag*{(B.37)}$$

$$\gamma_{r\theta} = \frac{1}{r} \cdot \frac{\partial u_r}{\partial \theta} + \frac{\partial u_\theta}{\partial r} - \frac{u_\theta}{r} \tag*{(B.38)}$$

$$\gamma_{rz} = \frac{\partial u_r}{\partial z} + \frac{\partial u_z}{\partial r} \tag*{B.39)}$$

$$\gamma_{\theta z} = \frac{\partial u_\theta}{\partial z} + \frac{1}{r} \cdot \frac{\partial u_z}{\partial \theta} \tag*{(B.40)}$$

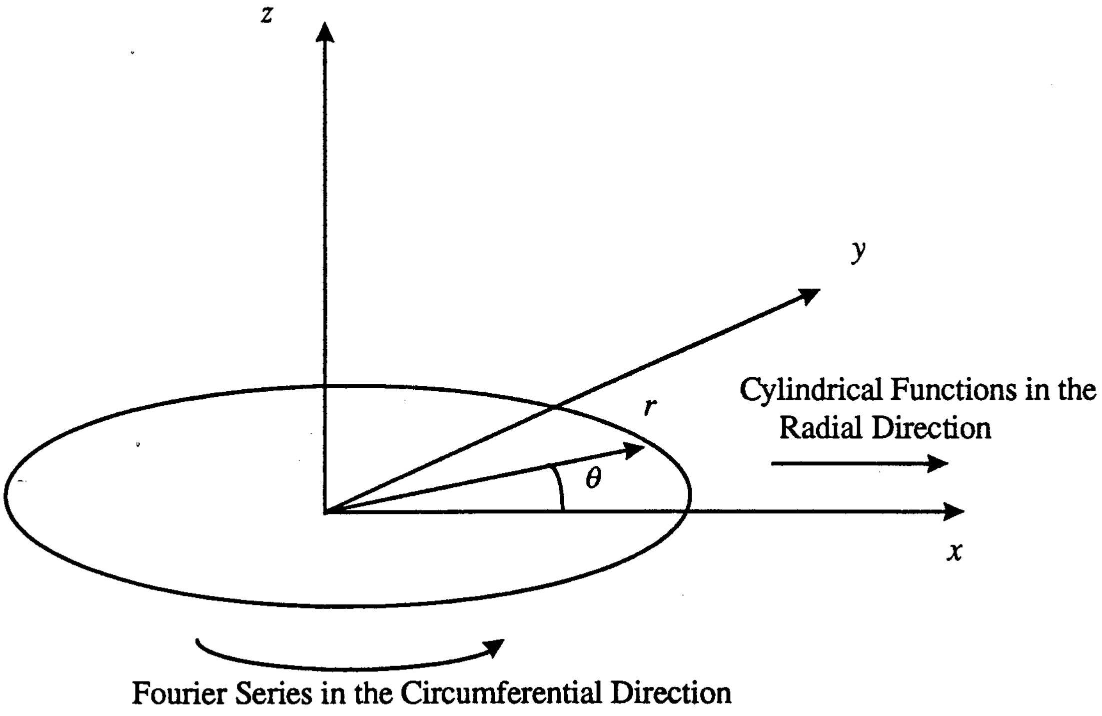

Figure B.3 Decomposition of the Displacements and Stresses in the Circumferential and Radial Directions in a Cylindrical Coordinate System.

where ε and γ are the normal and shear strains, respectively. The constitutive equations relating stresses to strains are expressed as

$$\sigma_r = \lambda e + 2G\varepsilon_r \tag{B.41}$$

$$\sigma_\theta = \lambda e + 2G\varepsilon_\theta \tag{B.42}$$

$$\sigma_z = \lambda e + 2G\varepsilon_z \tag{B.43}$$

in which *e* is the volumetric strain defined as

$$e = \varepsilon_r + \varepsilon_\theta + \varepsilon_z = \frac{\partial u}{\partial r} + \frac{u_r}{r} + \frac{1}{r}\cdot\frac{\partial u_\theta}{\partial \theta} + \frac{\partial u_z}{\partial z} \quad , \tag{B.44}$$

and λ and G are Lame's constant and the shear modulus, respectively.

A rotation vector (Ω) is introduced, which satisfies the relationship given by

$$\frac{\partial \Omega_r}{\partial r} + \frac{\Omega_r}{r} + \frac{1}{r}\cdot\frac{\partial \Omega_\theta}{\partial \theta} + \frac{\partial \Omega}{\partial z} = 0 \tag{B.45}$$

The components of the rotation vector, Ω , Ω_θ, and Ω_z, in the *r*, θ and *z* directions, respectively, are defined in terms of displacements as

$$\Omega_r = \frac{1}{2}\left[\frac{1}{r}\cdot\frac{\partial u_z}{\partial \theta} - \frac{\partial u_\theta}{\partial z}\right] \tag{B.46}$$

$$\Omega_\theta = \frac{1}{2}\left[\frac{\partial u_r}{\partial z} - \frac{\partial u_z}{\partial r}\right] \tag{B.47}$$

$$\Omega_z = \frac{1}{2}\left[\frac{\partial u_\theta}{\partial r} + \frac{u_\theta}{r} - \frac{1}{r}\cdot\frac{\partial u_r}{\partial \theta}\right] \tag{B.48}$$

The stresses can be expressed in terms of displacements by substituting the equations relating strain to displacement given by Eqs. (B.35) through (B.40) into Eqs.(B.41) through (B.43). Substituting the obtained expressions for stress into the dynamic equilibrium equations in Eqs. B.32 through B.34, and rewriting these equations using Eq. (B.44) through (B.48), the following equations are obtained:

$$(\lambda+2G)\frac{\partial e}{\partial r}+2G(\frac{\partial \Omega_\theta}{\partial z}-\frac{1}{r}\cdot\frac{\partial \Omega_z}{\partial \theta})=\rho\frac{\partial^2 u_r}{\partial t^2} \tag{B.49}$$

$$(\lambda+2G)\frac{1}{r}\cdot\frac{\partial e}{\partial \theta}+2G(\frac{\partial \Omega_z}{\partial r}-\frac{\partial \Omega_r}{\partial z})=\rho\frac{\partial^2 u_\theta}{\partial t^2} \tag{B.50}$$

$$(\lambda+2G)\frac{\partial e}{\partial z}+2G(\frac{1}{r}\cdot\frac{\partial \Omega_r}{\partial \theta}-\frac{\partial \Omega_\theta}{\partial r}-\frac{1}{r}\Omega_\theta)=\rho\frac{\partial^2 u_z}{\partial t^2} \tag{B.51}$$

These equations represent the equations of motion in a cylindrical coordinate system determined in terms of volumetric strain *e* and rotational vector Ω. The equations of motion describe the radiated field of waves in a cylindrical coordinate system and correspond to the equations of motion in a Cartesian coordinate system given by Eqs. (B.15) through (B.17).

B.4 General Solutions to the Wave Equation

The general solution to the wave equation formulated from the equations of motion given by Eqs. (B.49) through (B.51) can be expressed by "inverse Hankel transform" in cylindrical coordinates. This procedure is developed by Kausel and Peek (1982), using the decomposition of displacements in cylindrical functions (Cμ) in the radial direction, and in a Fourier series (**D**μ) in the circumferential direction as shown in Figure B.3. The general solution is then given by

$$\mathrm{U}(r,\theta,z,\omega)=\sum_{\mu=0}^{\infty}\mathrm{D}_\mu\int_{k=0}^{\infty}k\mathrm{C}_\mu\overline{\mathrm{U}}_\mu(k,\mu,z,\omega)dk \tag{B.52}$$

in which the terms *k* and μ are the wave number and the Fourier index, respectively. The Fourier index refers to the order of the Fourier component, given by 0, 1, 2, ... The term **U**(*r*, *θ*, *z*,*w*) is the displacement in spatial domain. The bar in the equation denotes the wave number domain, and the term $\overline{\mathrm{U}}_\mu(k,\mu,z,\omega)$ is the displacement in this domain corresponding to the μ th order Fourier component. The matrix Cμ in this equation includes cylindrical functions and is given by

$$\mathrm{C}\mu=\begin{bmatrix}\frac{d}{d(kr)}J\mu & \frac{\mu}{kr}J\mu & 0\\ \frac{\mu}{kr}J\mu & \frac{d}{d(kr)}J\mu & 0\\ 0 & 0 & -J\mu\end{bmatrix} \tag{B.53}$$

in which $J\mu=J\mu(kr)$ is the Bessel function of the first kind and μth order. The matrix **D**μ is the diagonal matrix corresponding to Fourier components and is given by

$$D\mu = diag(\cos\mu\theta,\ -\sin\mu\theta,\ \cos\mu\theta) \tag{B.54}$$

if the displacements are symmetric with respect to the radial direction, or

$$D\mu = diag(\sin\mu\theta,\ \cos\mu\theta,\ \sin\mu\theta) \tag{B.55}$$

if the displacements are anti-symmetric. Other cases can be formulated by combinations of these two situations.

For determining the displacement $U(r,\ \theta,\ z,\ \omega)$ corresponding to the external load in the spatial domain, the displacement $\overline{U}_\mu(k,\mu,z,\omega)$ in the wave number domain needs to be solved for a transformed load $\overline{P}_\mu(k,\mu,z,\omega)$ in the same domain. The transformed load in the wave number domain is determined by the Hankel transform of the load in the spatial domain. Hankel transform is given by

$$\overline{P}_\mu(k,\mu,z,\omega) = a\mu\int_{r=0}^{\infty} rC_\mu \int_{\theta=0}^{2\pi} D_\mu P(r,\theta,z,\omega)\, d\theta dr \tag{B.56}$$

where $a\mu$ is the orthogonalization factor and given by

$$a\mu = \frac{1}{2\pi} \quad \text{if } \mu=0,$$
$$= \frac{1}{\pi} \quad \text{if } m\neq 0. \tag{B.57}$$

The displacement in the wave number domain is given by the following:

$$[\mathbf{K}]\cdot\overline{\mathbf{U}}_\mu(k,\mu,z,\omega) = \overline{\mathbf{P}}_\mu(k,\mu,z,\omega) \tag{B.58}$$

where [K] is the stiffness matrix of a layered system in the wave number domain.

The stiffness matrices derived in Cartesian coordinates in Section B.2.2 can be used to formulate the global stiffness matrix in cylindrical coordinates. The reason for this compatibility is that the displacements in the wave number domain in cylindrical coordinates were expanded in a Fourier series in the circumferential direction, thus leading to an infinite number of two-dimensional problems.

B.5 Particular Solutions due to a Vertical Disk Load Acting on Surface

In the surface wave test, only one downward load is applied. Gucunski has simplified the general solution and acquired the particular solution for a case when only one load is applied downward (Gucunski and Woods, 1992) on the surface. Eq. (B.52) can be reduced to

$$\mathrm{U}(r,w)=\int_{k=0}^{\infty}-k\begin{bmatrix}J_1(kr) & 0\\ 0 & J_0(kr)\end{bmatrix}\overline{\mathrm{U}}(k,w)dk \tag{B.59}$$

Eventually, the particular solutions for the specified load are obtained as

$$u_r(r,w)=qR\int_0^{\infty}\bar{u}_r(k,w)J_1(kR)J_1(kr)dk \tag{B.60}$$

$$u_z(r,w)=qR\int_0^{\infty}\bar{u}_z(k,w)J_1(kR)J_0(kr)dk \tag{B.61}$$

where $u_r\,(r,w)$ and $u_z\,(r,w)$ represent the displacement in spatial domain corresponding to horizontal and vertical directions, respectively, and $\bar{u}_r(k,w)$ and $\bar{u}_z(k,w)$ are the displacements in wave number domain corresponding to horizontal and vertical directions, respectively. R represents the diameter of the disk load and r is the distance from the load.

Finally, using phase angle between the real and imaginary solution, the phase velocity can be acquired for a given frequency. This whole procedure has to be repeated for each desired frequency.

APPENDIX C

SURFACE WAVE TESTING AND ANALYSIS METHODS

APPENDIX C

SURFACE WAVE TESTING AND ANALYSIS METHODS

Theoretical Background

A vertical impact on the surface of an elastic half-space will create two types of wave propagation. These waves are body and surface waves. Body waves consist of compression and shear waves, which propagate in all directions away from the impact, but differ in the direction of particle motion. Shear waves (S-waves) have particle motion perpendicular to the direction of propagation, while compression waves (P-waves) have particle motion parallel to the direction of propagation (Kramer, 1996).

Surface waves were first investigated by Lord Rayleigh (1885). There are several types of surface waves, which all propagate near the surface of a medium. The type of surface wave used in this research is the Rayleigh wave. The particle motion of Rayleigh waves is both in the vertical and horizontal directions and varies with depth as shown in Figure C.1. The waves propagate along a cylindrical wavefront and the particle motion forms a retrograde ellipse near the surface, and a prograde ellipse at greater depths. At depths greater than about one wavelength the particle motion approaches zero. The Rayleigh wave contains 67% of the total energy from a vertical impact on a half-space. The remaining energy is present in the body waves (Kalinski, 1994).

The theoretical equations that describe wave motion in solids are usually developed using linear elastic theory. This is because wave propagation is typically considered in elastic materials, or materials that behave elastically during wave propagation. Testing in this research was performed on asphalt concrete, a viscoelastic material. Viscoelastic materials are rate-dependent, meaning their behavior is dictated by the rate of loading applied. Due to the time-temperature superposition principle of viscoelastic materials, a high rate of loading will correspond to behavior at lower temperatures where the material behaves more elastically. The high rate of impact loading in this research resulted in linear elastic behavior of the asphalt concrete and therefore linear elastic equations may be used to describe the wave motion.

Development of Wave Equations

In any linear elastic body, the stress-strain relationship is described by Hooke's law. For an isotropic material, only two constants are required to relate stress and strain. These constants are called Lame's constants and are denoted by λ and η (Kolsky, 1963). Lame's constants are related to the shear modulus (G) and Poisson's ratio (ν) as follows:

$$\lambda = \frac{2\nu G}{(1-2\nu)} \tag{C.1}$$

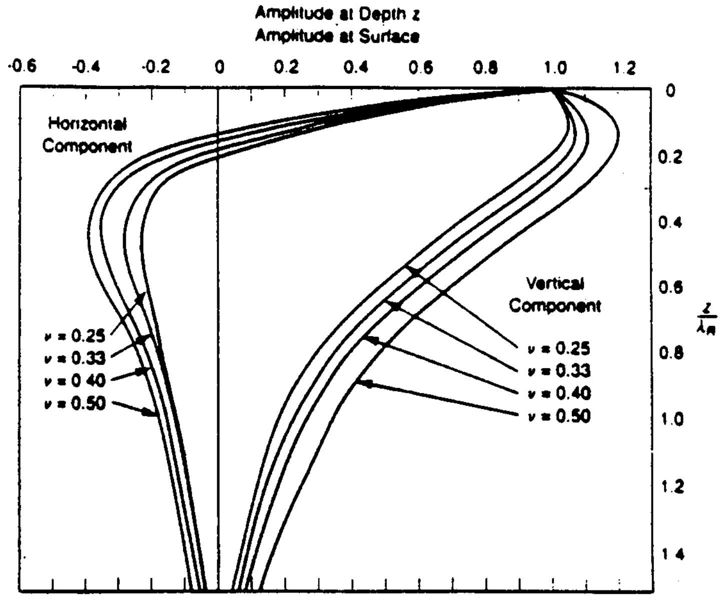

Figure C.1 Horizontal and Vertical Motion of Rayleigh Waves (Richart et al., 1970).

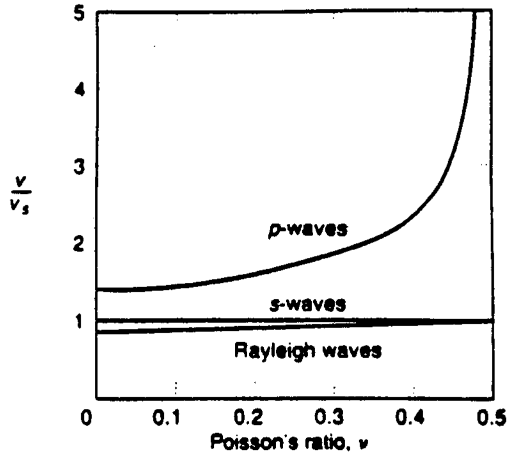

Figure C.2 Variation of Rayleigh and Body Wave Velocites with Poisson's Ratio (Richart, 1962).

$$\mu = G \tag{C.2}$$

The three-dimensional equations of motion for an elastic solid are obtained from equilibrium requirements on an infinitesimal cube in three orthogonal directions (x,y,z). These equations are presented below.

$$\rho \frac{\partial^2 u}{\partial t^2} = \frac{\partial \sigma_{xx}}{\partial x} + \frac{\partial \sigma_{xy}}{\partial y} + \frac{\partial \sigma_{xz}}{\partial z} \tag{C.3}$$

$$\rho \frac{\partial^2 v}{\partial t^2} = \frac{\partial \sigma_{yx}}{\partial x} + \frac{\partial \sigma_{yy}}{\partial y} + \frac{\partial \sigma_{yz}}{\partial z} \tag{C.4}$$

$$\rho \frac{\partial^2 w}{\partial t^2} = \frac{\partial \sigma_{zx}}{\partial x} + \frac{\partial \sigma_{zy}}{\partial y} + \frac{\partial \sigma_{zz}}{\partial z} \tag{C.5}$$

Differentiating the above three-dimensional equations of motion with respect to dilatation (Δ) and rotation (Ω) yields the wave equations for compression and shear waves respectively (Kolsky, 1963).

$$\frac{\partial^2 \Delta}{\partial t^2} = \frac{\lambda + 2\mu}{\rho} \nabla^2 \Delta \tag{C.6}$$

$$\frac{\partial^2 \Omega}{\partial t^2} = \frac{\mu}{\rho} \nabla^2 \Delta \tag{C.7}$$

where

λ, μ = Lame's constants,
ρ = density,
$\Delta = \varepsilon_{xx} + \varepsilon_{yy} + \varepsilon_{zz}$, and
$\nabla^2 = \frac{\partial^2}{\partial x^2} + \frac{\partial^2}{\partial y^2} + \frac{\partial^2}{\partial z^2}$ (Laplacian operator).

Equations C.6 and C.7 indicate the velocities of compression and shear waves are as follows:

$$V_p = \sqrt{\frac{\lambda + 2\mu}{\rho}} \tag{C.8}$$

$$V_s = \sqrt{\frac{\mu}{\rho}} \tag{C.9}$$

Substituting equations C.1 and C.2 for Lame's constants into the above equations results in the wave velocities for compression and shear waves in terms of elastic properties as shown below (Kramer, 1996).

$$V_p = \sqrt{\frac{G(2-2\nu)}{\rho(1-2\nu)}} \tag{C.10}$$

$$V_s = \sqrt{\frac{G}{\rho}} \tag{C.11}$$

By solving the two-dimensional equations of motion for a continuum, the relationship between surface and shear wave speed can be determined. The sixth order equation shown below can be solved for the ratio of the surface wave speed to the shear wave speed (Kolsky, 1963).

$$\alpha^6 - 8\alpha^4 + 8(3 - \frac{1-2\nu}{1-\nu})\alpha^2 - 16(1 - \frac{1-2\nu}{1-\nu}) = 0 \tag{C.12}$$

In the above equation, the ratio of the surface wave speed to the shear wave speed (α) is a function of Poisson's ratio. Richart (1962) developed the relationship between body waves and surface waves as a function of Poisson's ratio as shown in Figure C.2. For any given Poisson's ratio, the body wave velocities can be estimated from the surface wave velocity.

Using either equation C.10 or C.11, the shear modulus can be computed. The elastic modulus can also be determined from theory of elasticity using the following relation:

$$E = 2G(1+\nu) \tag{C.13}$$

From equations C.10 through C.13, it is clear that there is a direct relationship between wave speed and elastic modulus of a material. For a given material with constant Poisson's ratio and density, an increase in wave speed of any type corresponds to an increase in shear modulus, and therefore also an increase in elastic modulus.

Dispersion of Surface Waves

In a homogeneous, isotropic, linear elastic half-space, the Rayleigh wave velocities will not vary with frequency. However, in a layered half-space such as a pavement or soil profile, Rayleigh waves are said to be dispersive due to the fact that the various frequency components of the wave travel at different velocities. This occurs because the low frequencies of a Rayleigh wave will sample deeper depths while the higher frequencies sample shallower depths. Thus, the velocities corresponding to each frequency will reflect the properties of the sample depth of that frequency. It has been shown that the effective sampling depth of a Rayleigh wave is approximately one-third to one-half of the wavelength of the wave.

The wave velocity is related to the wavelength (λ) and frequency (f) of a stress wave as follows:

$$V = \lambda f \tag{C.14}$$

The velocities that correspond to each frequency in the above equation are called phase velocities. Often the Rayleigh wave velocities are just referred to as wave speed. The terms phase velocity and wave speed will be used interchangeably throughout this report.

In a layered pavement system, the stiffness of each layer typically decreases with increasing depth. Therefore, it is evident that the phase velocities will also decrease as the frequency decreases and the sampling depth increases. This relation will be reversed if a layered system has an increasing stiffness with depth such as a typical soil profile.

Surface Wave Testing Procedure

The surface wave test is performed by recording the particle displacements on the surface of a material at two or more locations due to loading. The test is quick and relatively simple, although care must be taken so that accurate and meaningful data are obtained. The required components for the test are an energy source, receivers, a data collection device, and a data storage device.

During the surface wave test, a linear array of sensors are placed on the material to be tested. An impact is made a certain distance from the first sensor in line with the linear sensor array. The resulting surface wave propagates in all directions, but is recorded along the linear array. The surface particle displacements at each sensor are converted to voltages and displayed on a digital oscilloscope. Finally these signals are stored in a computer for further study at a later time.

The sensor spacing for the surface wave test is determined based on the amount of energy from the source and the frequencies generated. More energy and lower frequencies will produce longer wave lengths and will require a larger sensor spacing. The spacing between each sensor is usually kept the same distance, and the distance from the source to the first sensor is typically the same distance as the sensor spacing. Although this distance will not affect the sensor-to-sensor phase velocity calculation, the distance should be at least one wavelength from the first sensor in order for the surface wave to fully develop. The maximum wave speeds found during this research were about 1524 m/s (5000 ft/s) at a dominant frequency of 10 KHz. Therefore, using equation C.14, the maximum wavelength will be about 15.25 cm (6.0 in). A sensor spacing of 15.25 cm (6.0 in) was used throughout this research.

Energy Source

Numerous types of energy sources have been used for stress wave testing. Some of the most common are hammers, metal balls, piezoelectric shakers, and spring-loaded devices. It is imperative that the energy source create a signal in the frequency range of interest. If surface layer properties are of importance, higher frequencies should be generated. Lower frequencies will reveal more information about deeper layers. A sufficient amount of energy is also required so that the signal is not influenced by background noise. The wave will naturally attenuate as it propagates and requires enough energy to be accurately recorded at the farthest sensor. Thus, a larger sensor spacing array will require more energy than a smaller one.

Throughout this research, an 8 oz. metal hammer was used as the energy source. Numerous studies were performed in order to determine the best energy source for a pavement stress wave application. It was found that an 8 oz. metal hammer worked best in combination with a small aluminum plate of dimensions 8.9 cm x 5.1 cm x 0.6 cm (3.5 in x 2.0 in x 0.25 in). Several objects were tested for use in combination with the metal hammer, but it was found that the aluminum plate provided the best and most consistent signals (Whitmoyer, 1993).

The aluminum plate was placed on its side perpendicular to the testing array. By striking the plate on its side, a relatively smooth, repeatable signal is obtained as shown in Figure C.3. A smooth signal with clearly defined peaks is desirable due to the nature of the signal processing techniques used. This type of signal contains energy primarily in one frequency range, and noise from unwanted frequencies is not present.

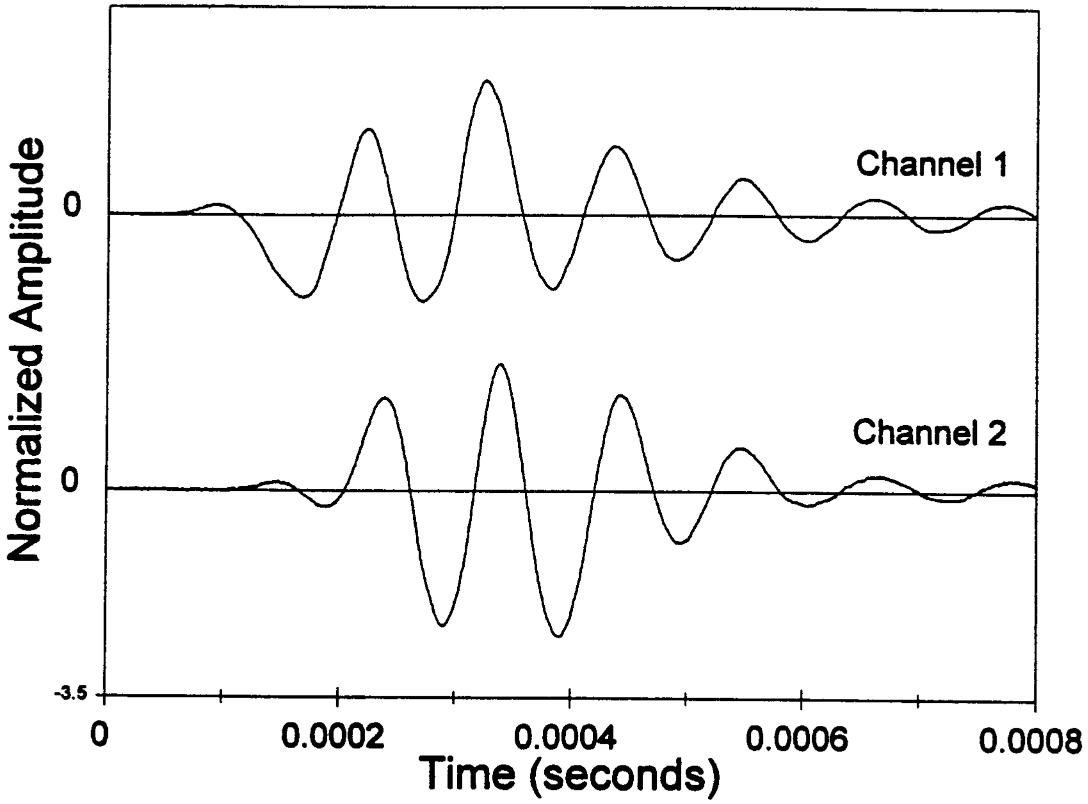

Figure C.3 Typical Surface Wave Test Signals.

An additional advantage of using the aluminum plate is that it prevents distortion of the material at the impact location. When numerous impacts are made at the same location on a material, the signal can be affected by cracking or crushing of the material. This is especially true on asphalt concrete due to its lower stiffness than other structural materials and its temperature dependency. Deterioration of the material at the impact location can significantly reduce the quality of the signal and can affect the results of an experiment. This research involved testing at the same locations a vast amount over the course of 2 days. The use of the aluminum plate greatly increased data quality while providing an effective way of transferring the energy from the source to the testing material.

Sensors

The sensors are required to detect and record the surface particle motion and convert the motion to a recordable measure of unit. Different sensors can measure displacement, velocity, or acceleration and record the motion as voltage. Velocity and acceleration are the first and second derivatives of displacement and are 90 and 180 degrees out of phase with displacement respectively (Kalinski, 1994). Since displacement, velocity, and acceleration are all closely related, any of them can be measured to record the stress wave signal.

In this research, PCB model 303A02 piezoelectric accelerometers were used to measure the particle accelerations at the pavement surface. Four accelerometers were used in order to obtain more information from the linear testing array, and to help facilitate the use of the signal processing methods.

Data Acquisition

The stress wave signal is obtained by use of a data acquisition device. This device will read the voltage changes from each sensor and plot them as a function of time. The device should be versatile so that various parameters concerning the data may be altered. The device should also have multiple input channels for simultaneous recording of two or more channels. A Tektronix 420A digital oscilloscope is used for all stress wave testing performed at North Carolina State University. The Tektronix oscilloscope can record up to four channels at once and numerous signal parameters can be adjusted, such as the number of data points, sample rate, horizontal and vertical scales, and trigger values. The oscilloscope has a display screen in which the user can view all four channels at once by vertically offsetting each channel.

The initial setup of the oscilloscope parameters is typically a trial and error process because the setup will vary depending on the impact type and intensity, and the material being tested. However, once the impact device and testing application are chosen, the oscilloscope parameters can be adjusted to optimum values and then saved in memory for all future testing of that application. During testing in this research, typically 2500 data points were recorded at a sample rate of 2.5 x 10^6 samples per second. Occasionally these values were altered due to temperature effects, but changing these parameters will not affect the signal obtained from the testing. The horizontal and vertical scales were adjusted for optimum viewing of the signals on the oscilloscope display.

The trigger level is the threshold value that will start recording of the signal by the oscilloscope when reached at a chosen sensor. This level is set as a positive or negative value and is selected at the nearest receiver in the surface wave testing array. Since there is always some amount of data prior to reaching the trigger value, a specified amount of pre-trigger data is recorded. These data are constantly present in an internal buffer in the oscilloscope, but are not recorded unless the trigger value is reached. The amount of pre-trigger data recorded was typically set at around 20% of the total record. An additional benefit of the pre-trigger data is that they precede the signal data with some zero amplitude data, which are necessary for some of the signal processing tools used for analysis.

Recording Device

A recording device is needed to save the stress wave data for future analysis. A floppy disk drive may be present in the data acquisition device to save data directly to disk. During this research, all data were saved directly to the hard drive of a Zenith 486 portable computer. This allowed a large number of data files to be saved in a format specified by the user. The data were backed up on floppy disks after completing the testing for each day.

Analysis Techniques

There are several digital signal processing methods that can be used to analyze surface wave data. The stress wave signal is often first converted from the time domain to the frequency domain by use of the Fourier transform. This transformation allows one to view the individual frequency components present in the signal. Once the frequencies present in the signal have been identified, it is useful to calculate the wave speeds at various frequencies, known as phase velocities. Phase velocities can be computed using two different methods, the Fourier Phase method and the Short Kernel Method.

A dispersion curve can be constructed by plotting the phase velocities versus frequency or wavelength. Since the sample depth of the Rayleigh wave is directly related to its wavelength, it is convenient to plot the dispersion curve as phase velocity versus wavelength. Thus, the wavelength can be viewed as depth to obtain a better indication of the layer properties. However, it should be noted that a deeper sample depth includes information from all the layers above that depth and represents an average of all the above layer properties. In order to differentiate between individual layer properties from a dispersion curve, a process of inversion must be used to convert the curve to the actual shear wave velocity profile. The velocities of the inverted curve will represent the properties of only the individual layers.

The Fourier Transform

A typical stress wave signal from an impact energy source is nonperiodic and composed of numerous frequency components. This signal can be broken down into its various sinusoidal components by use of the Fourier transform. This process is referred to as conversion from the time domain to the frequency domain. Mathematically, the continuous Fourier transform of x(t) is defined as (Chen, 1995):

$$Y(f) = \int_0^n x(t)e^{-j(2\pi)ft}dt \tag{C.15}$$

Y(f) is a complex number with a real component (Y_{Re}(f)) and an imaginary component (Y_{Im}(f)). It can be represented as a vector in a complex coordinate system as shown in Figure C.4. Each vector on the graph corresponds to a discrete frequency with amplitude and phase angle defined as (Chen, 1995):

$$A(f) = \sqrt{[Y_{\mathrm{Re}}(f)]^2 + [Y_{\mathrm{Im}}(f)]^2} \tag{C.16}$$

$$\phi = \tan^{-1}(\frac{Y_{\mathrm{Im}}(f)}{Y_{\mathrm{Re}}(f)}) \tag{C.17}$$

The Fourier transformed signal is commonly viewed as a plot of amplitude versus frequency as shown in Figure C.5. Due to the lengthy calculations performed during the Fourier transform, a Fast Fourier Transform (FFT) algorithm is commonly used. The FFT function approximates the Fourier transform integration and uses mathematical symmetries to speed up the calculations. A requirement of the FFT is that the number of input data points must be a power of 2 (Kalinski, 1994). In this research, 2^{13} was consistently used.

The Fourier Phase Method

The Fourier Phase method is often used when performing the Spectral Analysis of Surface Waves test to compute surface wave phase velocities and construct the dispersion curve. The process involves performing a Fourier transform of two surface wave signals

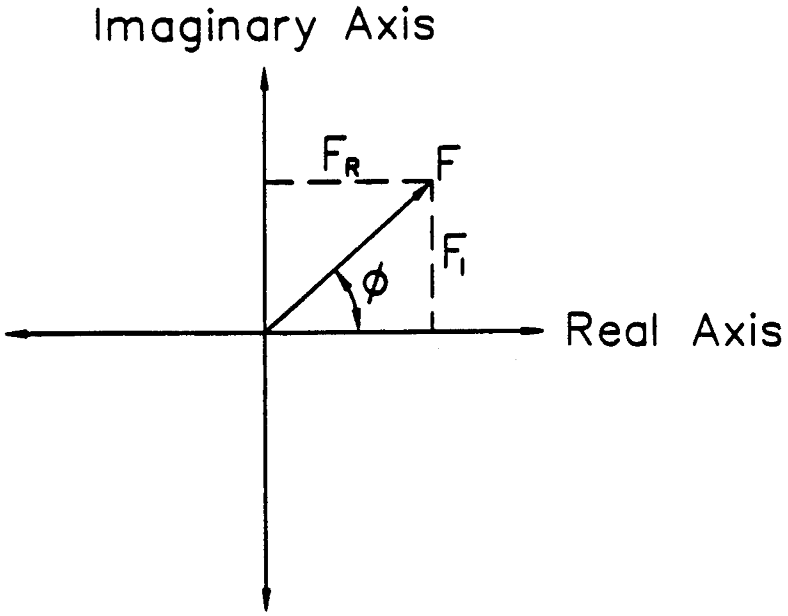

Figure C.4 Fourier Transform as a Complex Vector.

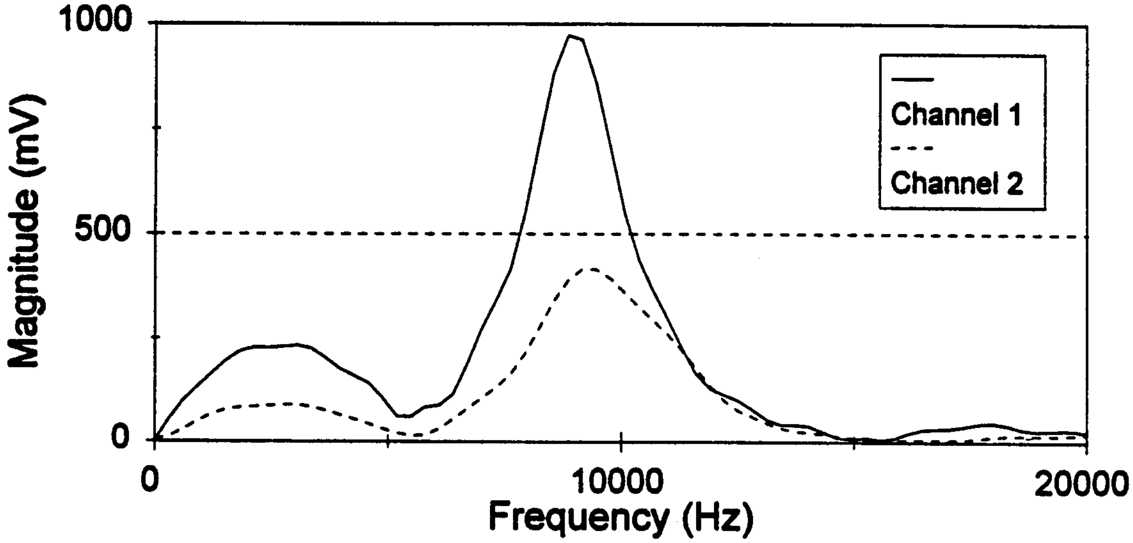

Figure C.5 Fourier Transform Amplitude Plot.

determining their frequency components and phase angles. The entire dispersion curve is then directly constructed from this information.

The Fourier Phase method is a straight forward and simple way to construct the entire dispersion curve at once. However, there are several major drawbacks to this method. In a layered system where the velocities will vary with depth, there will be multiple limbs of the dispersion curve due to the fact that there can be more than one solution for each frequency (Douglas et al., 1989). The Fourier Phase method is not capable of determining the multiple limbs of a dispersion curve because it is based on the Fourier transform, which can only identify one wave speed for each frequency. The actual dispersion curve constructed is an average of the multiple curves. In addition, the Fourier Phase method cannot determine new entry points for data and cannot identify multiple input signals contained in an output signal. This phenomenon is termed the "multiple voice" problem. One other problem with the method is that the exact value of the phase angle is unknown since it can be the angle computed or that angle plus some multiple of 360 degrees. Douglas et al. (1989) provide further explanation of these problems with the Fourier Phase method.

The Short Kernel Method

The Short Kernel Method (SKM) is a digital signal processing technique developed at North Carolina State University by Dr. R.A. Douglas. The method is used to calculate phase velocities and has been successfully applied to numerous stress wave applications. The process involves a piecewise examination of the signal by use of an SKM kernel. The kernel can be a sine, cosine, or any other function, but must have the same time step as the recorded data. Typically, a sine function of one cycle is used as the kernel and was used throughout this research.

The SKM value at a particular frequency can be stated as follows (Chen, 1995):

$$S_k(j\Delta t) = \sum_{i=0}^{n-1} x[(j+i)\Delta t] f_k[i\Delta t] \tag{C.18}$$

By substituting t = j(t), the equation is simplified to:

$$S_k(t) = \sum_{i=0}^{n-1} x(t + i\Delta t) f_k[i\Delta t] \tag{C.19}$$

where:

$S_k(t)$ = data point from SKM transform at assigned kth kernel frequency,
$f_k(i\Delta t)$ = data point from SKM kernel at assigned kth kernel frequency,
$x(t)$ = data point from real time record,
t = data point location at real time axis,
k = index of assigned SKM kernel frequency,
n = total number of data points in the assigned SKM kernel, and
Δt = time step at real time record and SKM kernel.

During the Short Kernel Method, the kernel of a certain frequency is lined up with the record data as shown in Figure C.6. The points on the kernel are multiplied by the corresponding points on the recorded signal. The sum of these products is plotted on a new graph at the time of the first point of the kernel. The kernel is then moved forward one data point and the whole process is repeated. This calculation is continued until the kernel reaches the end of the signal. The resulting function is the SKM transform function. The points where the kernel matches the signal the best will have the highest values of the SKM transform function, such as the one shown in Figure C.6. Similarly, the points where the kernel is most out of phase with the signal will have the lowest or most negative values of the SKM transform function. In this respect, the SKM procedure essentially filters out the frequencies that are not of interest and magnifies the chosen frequency of the kernel. The peaks of the SKM transform function therefore represent wave propagation of the frequency component of interest.

By plotting the SKM transform function for a signal recorded at two sensor locations, the phase velocities can be computed. When the SKM is applied to the two time records, similar peaks will be present in both SKM transform functions, but the peaks of the second record will be shifted due to the time of propagation between the first and second sensors. This shift in the SKM transform function is shown in Figure C.7 for four linear sensor locations equally spaced apart. The shift of each signal is shown by the number one above each first major peak. The SKM transform function is normalized so that the magnitudes of each signal are similar. The time between any two peaks is known since the signals were recorded on the same time scale. The distance between any two gauges is also known. Therefore the phase velocity can be computed by dividing the distance between sensor locations by the time between the two corresponding peaks in the SKM transformed functions as shown below.

$$V_{ph} = \frac{d}{t} \tag{C.20}$$

The dispersion field may be constructed by calculating the phase velocities at several frequencies and plotting them as a function of frequency or wavelength.

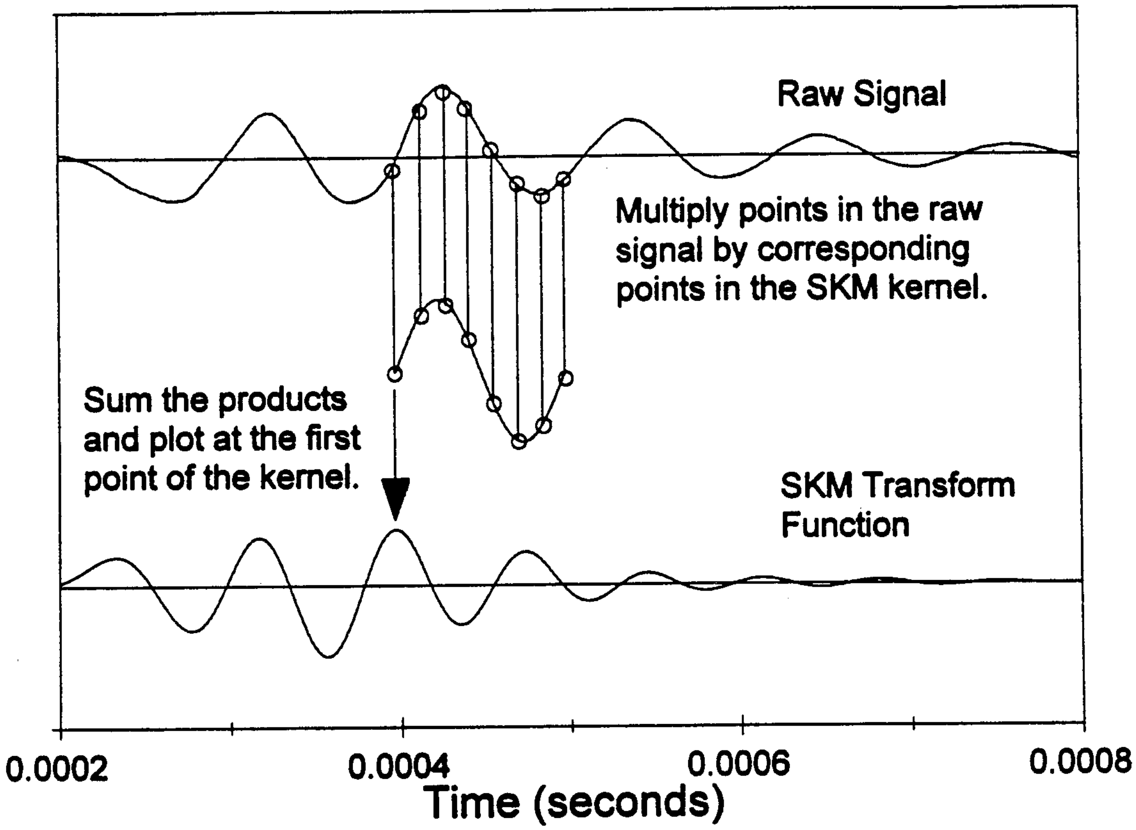

Figure C.6 Short Kernel Method Calculation.

Selection of Peaks Using the Short Kernel Method

When using the Short Kernel Method for phase velocity calculation, it is imperative that the proper peaks are selected. This will ensure that an accurate value of the phase velocity is obtained. If peaks that do not correspond to each other are selected, then an invalid phase velocity will result.

Selection of the proper peaks begins with locating a primary peak in the first channel of the SKM transform function and recognizing a diagonal shift in this peak as it shows up in the following channels. A distinct diagonal trend and well-defined peaks facilitate the proper selection of the peaks. Often the first primary peak in the first channel is chosen as the starting peak. Typically this will provide the most clearly defined trend in successive channels. This also avoids selecting an improper peak further in the time record due to the reflection of waves off of boundaries or the introduction of body waves.

The calculated phase velocity provides an additional way to be sure the proper peaks have been chosen. An approximate range for the phase velocity is known based on the material properties and the frequency of interest. Therefore, engineering judgment can be utilized in determining if the computed phase velocity is acceptable.

In certain testing configurations, small "pre-peaks" will show up in the SKM function prior to the first primary peak in the function. A study was conducted to determine the cause of these pre-peaks. It was found that the pre-peaks travel at about twice the wave speed of the surface waves and thus occur in greater amounts as the sensor spacing increases. These pre-peaks could be due to several factors; however, it is likely that they are compression waves that reflect off of the bottom of the surface layer and show up before the Rayleigh waves. In this research, the pre-peaks were always neglected and only the primary peaks were used for the phase velocity calculation.

Stress Wave Attenuation

In theory, stress waves will travel indefinitely in a homogeneous linear elastic material. However, in real materials stress waves will attenuate as they propagate. There are two types of damping that can cause this attenuation. Material and radiation damping will both occur as stress waves propagate in any material. However, this attenuation may be magnified if the material is significantly damaged.

Material Damping

Material damping is known as the conversion of elastic energy to heat as a stress wave propagates in a material (Kramer, 1996). This conversion of energy is due to friction between the individual particles from the particle motion caused by the wave. The

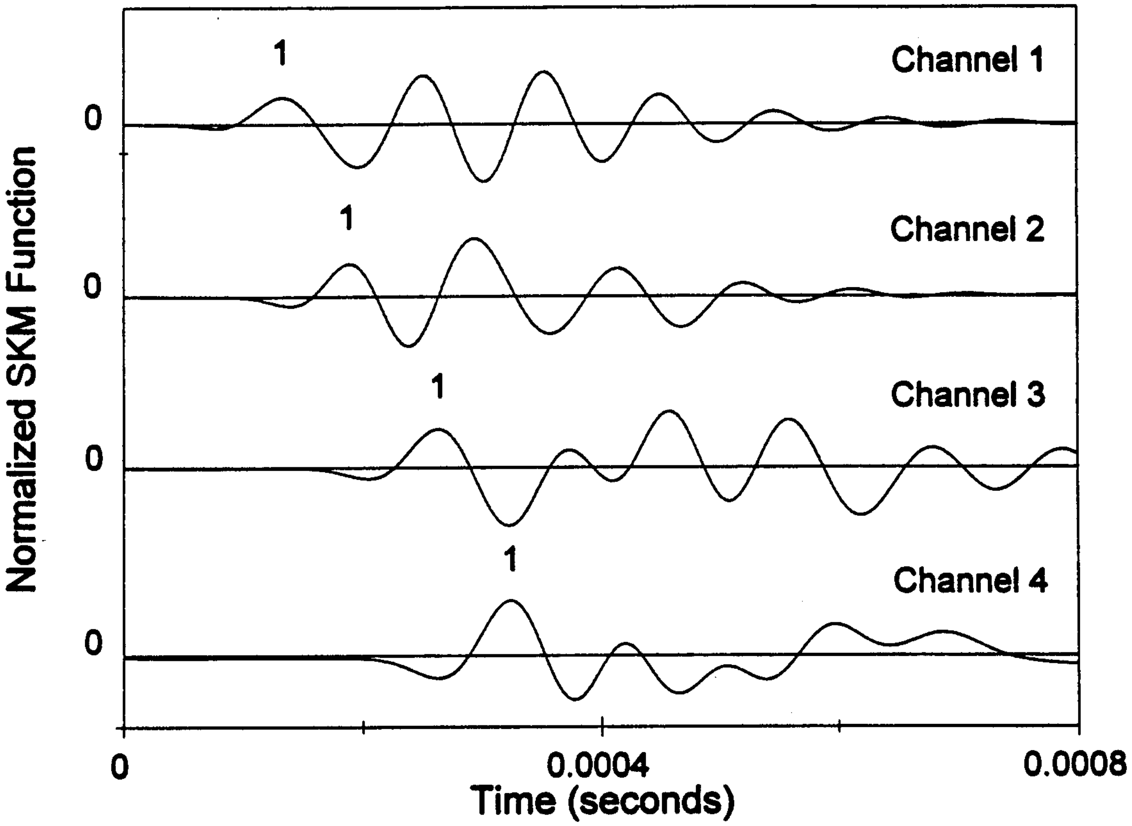

Figure C.7 Shift in the SKM Function for an Actual Time Record.

loss in energy results in a decrease in the amplitude of the wave. Viscous damping can be used to model the energy dissipation due to material damping as shown in figure C.8 (Kalinski, 1994). This system is a typical single degree of freedom system representing mass motion by use of a spring and dashpot for the elastic and viscous components respectively. The corresponding differential equation relating the displacement to the other forces present is as follows (Richart et al, 1970).

$$m\ddot{z} + c\dot{z} + kz = 0 \tag{C.21}$$

where:

z = displacement,
m = mass,
c = damping coefficient, and
k = spring constant.

Using this viscous model, the relationship between stress and strain can visually represent the energy loss due to material damping.

Below a strain level of 0.001%, an elliptical hysteresis loop results when stress is plotted versus strain as shown in Figure C.9. The total area within the loop A_{total} corresponds to the energy dissipated from material damping during one cycle. The peak energy during one cycle is shown as the shaded area and represents the maximum potential energy stored in one cycle of loading. The damping ratio can therefore be defined as follows (Kalinski, 1994).

$$\eta = \frac{A_{total}}{4\pi(A_{peak})} \tag{C.22}$$

Radiation Damping

Radiation damping or geometric damping is the attenuation of energy due to the wave spreading over a greater volume of material (Kramer, 1996). Therefore the amplitude of the wave is reduced proportionally with the distance the wave propagates.

Body waves traveling in a whole space will propagate as a spherical wavefront. The geometric damping of these waves causes the amplitude to decrease at a rate proportional to 1/r, where r is the radial distance from the impact location. For body waves traveling along a half-space, the rate of decrease of amplitude is proportional to $1/r^2$. Surface waves travel as a cylindrical wavefront and will attenuate much slower than body waves at a rate proportional to $1/r^{0.5}$ (Kramer, 1996). The slower attenuation of the surface wave from radiation damping provides an additional advantage for its use in stress wave testing.

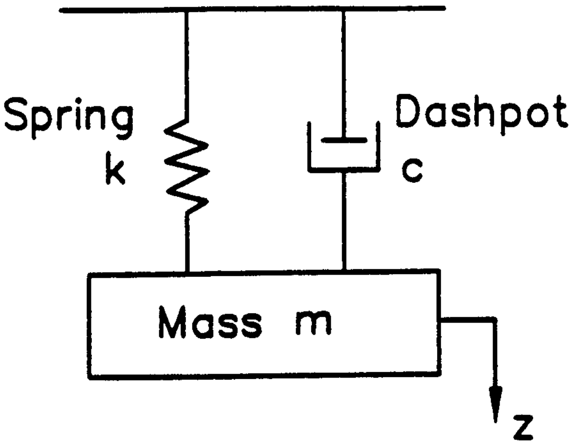

Figure C.8 Single Degree of Freedom Viscous Damping (Kalinski, 1994).

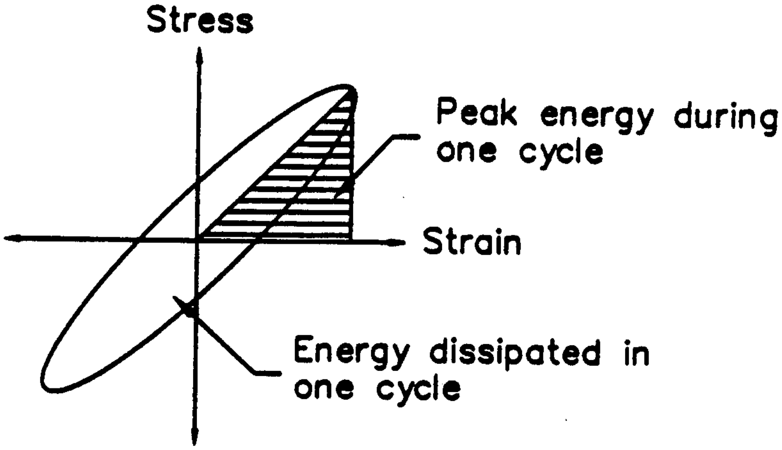

Figure C.9 Relationship Between Hysteresis Loop and Damping Ratio (Kramer, 1996).

Stress Wave Amplitudes

The amplitude of a body wave propagating in a whole space can be expressed as shown below (Kalinski, 1994):

$$A(r) = \frac{A_o}{r} e^{-\alpha r} \tag{C.23}$$

where:

A_o = the initial amplitude,
α = attenuation coefficient, and
r = radial distance from source.

Similarly, a body wave and a surface wave that propagate along a half-space will have the following amplitudes respectively (Kalinski, 1994):

$$A(r) = \frac{A_o}{r^2} e^{-\alpha r} \tag{C.24}$$

$$A(r) = \frac{A_o}{\sqrt{r}} e^{-\alpha r} \tag{C.25}$$

In the above equations, the attenuation coefficient accounts for the loss of energy due to material damping and the proportionality of the radial distance represents the radiation damping. The attenuation coefficient can also be described by the following equation (Kalinski, 1994):

$$\alpha = \frac{\eta 2 \pi f}{V} \tag{C.26}$$

where:

f = frequency,
η = material damping ratio, and
V = wave velocity.

Body wave material damping does not vary with frequency since all frequencies propagate at the same velocity. Surface waves are dispersive and the material attenuation of the frequencies is dependent on the material properties of the layers. It is important that the dispersion of Rayleigh waves be considered during attenuation study. A filter that disregards the frequencies that do not correspond to the layers of interest can be used.

During this research, the impact energy used generated primarily high frequencies (8 - 12 KHz) as shown in Figure C.5. As mentioned earlier, in this research the maximum wavelength for the 10 KHz dominant frequency is 15.24 cm (6.0 in). This would produce an effective sampling depth of 5.1 to 7.6 cm (2.0 to 3.0 in). Therefore it is reasonable to conclude that the majority of the surface waves were contained in the surface layer. However, there is a certain amount of energy in the lower frequency range that is most likely due to the base layers. These frequencies will be filtered out so that only the frequencies of the surface layer are studied.

REFERENCES

Bajpai, A. C., I. M. Calus, J. A. Fairley, "Numerical Methods for Engineers and Scientists," pp. 37-39, *John Wiley and Sons Ltd.*, 1977.

Bendat, J. S., and A. G. Piersol, "Engineering Applications of Correlation and Spectral Analysis," *John Wiley and Sons, Inc.*, New York, 1980.

Bonaquist, R., and W. Mogawer, "Analysis of Pavement Rutting Data From the FHWA Pavement Testing Facility Superpave Validation Study," To be Published in *Transportation Research Record*, TRB, National Research Council, Washington, D.C., 1997.

Carino, N., "Methods for Monitoring Concrete Properties at Early Ages: An Overview," Presented at Annual Convention of the American Concrete Institute, Washington, D.C., March, 1992.

Chen, S., and Y. R. Kim, "Condition Assessment of Installed Timber Piles by Dispersive Wave Propagation," *Transportation Research Record*, TRB, National Research Council, Washington, D.C., 1996.

Chen, C. W., "Mechanistic Approach to the Evaluation of Microdamage in Asphalt Mixes," Ph.D. Dissertation, Civil Engineering, Texas A&M University, 1997.

Cominsky, R. J., J. S. Moulthrop, W. E. Elmore, and T. W. Kennedy. "SHRP Materials Library Asphalt Selection Process,▯ Center for Transportation Research, University of Texas at Austin, Report No. *SHRP-IR-A-89-002*, August, 1989.

Daniel, J. S. and Y.R. Kim, "Laboratory Evaluation of Fatigue Damage Growth and Healing of Asphalt Concrete Mixtures Using the Impact Resonance Method," Submitted for publishing in the *Journal for Materials in Civil Engineering*, 1997.

Di Benedetto, Nouvelle approche du comportement des enrobes bitumineux: resultats experimentaux et formulatin rheologique, RILEM: Mechanical Tests for Bituminous Mixes, October, 1990.

Douglas, R. A., J. L. Eddy, and H. E. Wahls, "On Transforms and the Dispersion Computations Used for Evaluating Layer Properties," *ASTM STP 1026.* ASTM, Philadelphia, 1989.

Elphingstone, G.M., "Adhesion and Cohesion in Asphalt-Aggregate Systems," PhD. Dissertation, Texas A&M University, 1997.

Good, R.J. and C. J. van Oss, "The Modern Theory of Contact Angles and the Hydrogen Bond Components of Surface Energies," *Modern Approaches to Wettability*, pp. 1-27, M.E. Schrader and G. Loeb, editors. Plenum Press, New York, 1992.

Gucunski, N., and R. D. Woods, "Numerical Simulation of the SASW Test," *Journal of Soil Dynamics and Earthquake Engineering*, Vol. 11, No. 4, pp. 213-227, 1992.

Halabe, U. B., Hota V.S. GangaRao, S. H. Petro, and Veerabhadra R. Hota, "Assessment of Defects and Mechanical Properties of Wood Members Using Ultrasonic Frequency Analysis," Materials Evaluation, Vol. 54, No. 2, pp. 314-322, February 1996.

Holt, J. D., S. Chen, and R. A. Douglas, "Determining Lengths of Installed Timber Piles by Dispersive Wave Propagation," *Transportation Research Record 1447*, TRB, National Research Council, Washington, D.C., 1994, pp. 110-115.

Kalinski, M. E., "Measurement of Intact and Cracked Concrete Structural Elements by the SASW Method," MS Thesis, University of Texas at Austin, 1994.

Katzke, E. D., "Nondestructive Evaluation of Asphalt Pavement Surface Layers Using Stress Wave Testing," M.S. Thesis, North Carolina State University, Raleigh, NC, 1997.

Kausel, E., and J. M. Roesset, "Stiffness Matrices for Layered Soils," *Bulletin of the Seismological Society of America,*" Vol. 71, No. 6, Dec. 1981.

Kausel, E., and R. Peek, "Dynamic Loads in the Interior of a Layered Stratum: An Explicit Solution," Bulletin of the Seismological Society of America, Vol. 72, No. 5, October 1982.

Kim, Y., and Y. R. Kim, "In-Situ Evaluation of Fatigue Damage Growth and Healing of Asphalt Concrete Pavements Using Stress Wave Method," To be published in *Transportation Research Record,* Transportation Research Board, Washington, D.C., 1997.

Kim, Y. R., S. L. Whitmoyer, and D. N. Little, "Healing in Asphalt Concrete Pavements: Is it Real ?" *Transportation Research Record 1454*, TRB, National Research Council, Washington, D.C., pp. 89-96, 1994 a.

Kim, Y.R., H. J. Lee, J. Sias, and Y. Kim, "Second Interim Report Submitted to Texas A&M Research Foundation", September, 1994 b.

Kim, Y.R., H. J. Lee, J. Sias, and Y. Kim, "Third Interim Report Submitted to Texas A&M Research Foundation", April, 1995 b.

Kim, Y.R., S. L. Whimoyer, and D. N. Little, "Healing in Asphalt Concrete Pavements: Is It Real?" *Transportation Research Record No. 1454*, Transportation Research Board, National Research Council, Washington, D.C., pp.89-96, 1995 c.

Kim, Y. R., H. J. Lee, and D. N. Little, "Fatigue Characterization of Asphalt Concrete Using Viscoelasticity and Continuum Damage Theory," Presented at the *Annual Meeting of the Association of Asphalt Paving Technologists*, March, 1997.

Kolsky, H., "Stress Waves In Solids," Dover Publications, New York, 1963.

Kramer, S. L., "Geotechnical Earthquake Engineering," Prentice-Hall Inc., Upper Saddle River, NJ, 1996.

Labib, M.E. *Asphalt-Aggregate Interactions and Mechanisms for Water Stripping*, 204th ACS National Meeting, American Chemical Society, Washington, D.C., 1992.

Lytton, R.L., Chen, C. W., and Little, D.N., "A Micromechanics Fracture and Healing Model for Asphalt Concrete," Final *Report Project 7229, Volume 3*, Task K - Microdamage Healing in Asphalt And Asphalt Concrete, Texas A&M University, College Station, TX, 1998.

Marwan F. A., K. H. Stokoe II, and R. C. Briggs, "Stiffness of Asphalt Concrete Surface Layer from Stress Wave Measurements," *Transportation Research Record 1384*, TRB, National Research Council, Washington, D.C., pp. 29-35, 1993.

McElvany, J. and P. S. Pell, "Fatigue Damage of Asphalt," *Highways and Road Construction*, Vol.41, No. 1766, October, 16-20, 1973.

McGonnagle, "Non Destructive Testing," *McGraw-Hill*, New York, 1961.

Nazarian, S., K. H. Stokoe II, and W. R. Hudson, "Use of Spectral Analysis of Surface Waves Method for Determination of Moduli and Thicknesses of Pavement Systems," *Transportation Research Record 930*, TRB, National Research Council, Washington, D.C., pp. 38-45, 1983.

Nazarian, S., and K. H. Stokoe II, "Use of Surface Waves in Pavement Evaluation," *Transportation Research Record 1070*, TRB, National Research Council, Washington, D.C., pp. 132-144, 1986.

Petersen, J. C., "Chemical Composition of Asphalts Related to Asphalt Durability: State of the Art," *Transportation Research Board No. 999*, pp. 13-30, 1984.

Raithby, K. D. and A. B. Sterling, "Effect of Rest Periods on Fatigue Performance of Hot-Rolled Asphalt Under Reversed Axial Loading," *Association of Asphalt Paving Technologists, Vol. 39*, pp. 134-147, 1970.

Rayleigh, L., "On Waves Propagated Along the Plane Surface of an Elastic Solid," *Proceedings* of the London Mathematical Society, Vol. 17, pp. 4-11, 1885.

Richart, F. E., "Foundation Vibrations," Transactions of the *ASCE, Vol. 127* Part 1, pp. 863-898, 1962.

Richart, F. E., J. R. Hall, R. D. Woods, "Vibrations of Soils and Foundations," *Prentice-Hall Inc.*, 1970

Road and Bridge Specification. "Virginia Department of Highways and Transportation," Commonwealth of Virginia, 1992.

Roesset, J. M., D. W. Chang, K. H. Stokoe II, and M. F. Aouad, "Modulus and Thickness of the Pavement Surface Layer from SASW Tests," *Transportation Research Record 1260*, TRB, National Research Council, Washington, D.C., pp. 53-63, 1990.

Schapery, R.A., "Correspondence Principles and Generalized J Intergral for Large Deformation and Fracture Analysis of Viscoelastic Media," *International Journal of Fracture*, Vol. 25, pp.195-223, 1983.

Schapery, R. A., "On the Mechanics of Crack Healing," *International Journal of Fracture*, 1988.

Sias, J. E., "Rate-Dependent Stiffnesses of Asphalt Concrete Used for Field to Laboratory Prediction and Fatigue and Healing Evaluation," M.S. Thesis, North Carolina State University, Raleigh, NC, 1996.

Whitmoyer, S., "Vibrational / Stress Wave Analysis in the Characterization of Asphalt Concrete," M.S. Thesis, North Carolina State University, 1993.

Whitmoyer, S. and Y. R. Kim, "Determining Asphalt Concrete Properties via the Impact Resonant Method," Journal of Testing and Evaluation, JTEVA, Vol. 22, No.2, March, pp. 139-148, 1994.

Yoder, E. J. and M. W. Witcjak, "Principles of Pavement Design," *John Wiley & Sons*, 1975.